



THE HONG KONG
POLYTECHNIC UNIVERSITY

香港理工大學

Pao Yue-kong Library

包玉剛圖書館

Copyright Undertaking

This thesis is protected by copyright, with all rights reserved.

By reading and using the thesis, the reader understands and agrees to the following terms:

1. The reader will abide by the rules and legal ordinances governing copyright regarding the use of the thesis.
2. The reader will use the thesis for the purpose of research or private study only and not for distribution or further reproduction or any other purpose.
3. The reader agrees to indemnify and hold the University harmless from and against any loss, damage, cost, liability or expenses arising from copyright infringement or unauthorized usage.

IMPORTANT

If you have reasons to believe that any materials in this thesis are deemed not suitable to be distributed in this form, or a copyright owner having difficulty with the material being included in our database, please contact lbsys@polyu.edu.hk providing details. The Library will look into your claim and consider taking remedial action upon receipt of the written requests.

**AERO-ACOUSTIC-STRUCTURAL
INTERACTIONS AND NOISE CONTROL
IN THE FAN-DUCTED SYSTEM**

YAN KEI CHIANG

Ph.D

The Hong Kong Polytechnic University

2018



THE HONG KONG POLYTECHNIC UNIVERSITY

DEPARTMENT OF MECHANICAL ENGINEERING

**AERO-ACOUSTIC-STRUCTURAL INTERACTIONS
AND NOISE CONTROL IN THE FAN-DUCTED
SYSTEM**

YAN KEI CHIANG

A thesis submitted in partial fulfilment of the requirements for the
degree of Doctor of Philosophy

July 2017

Certificate of Originality

I hereby declare that this thesis is my own work and that, to the best of my knowledge and belief, it reproduces no material previously published or written, nor material that has been accepted for award of any other degree or diploma, except where due acknowledgement has been made in the text.

_____ (Signed)

YAN KEI CHIANG (Name of Student)

Abstract

In a fan-ducted system such as the air-conditioning system and the turbofan engine of the aircraft, the noise attenuation of the fan noise at low blade-passage frequency is still a challenge. The flow effect is a major element which influences the silencing efficiency of the noise attenuation approaches. The effects of the flow field on the acoustic performance of the silencer with flexible structures can be classified into two categories: (1) change of acoustic characteristics of the silencing device due to the vortex formation; (2) change of acoustic response of the flexible structure due to the existence of unsteady flow.

Micro-perforated panel (MPP) is commonly utilized as the acoustic liner in the aircraft engine. The engine noise at high intensity sound changes the acoustic properties of the perforations due to the process of jet formation. The effect of orifice nonlinearity on the acoustic response and absorption performance of the promising MPP absorber array in parallel arrangement is investigated. The MPP absorber array is constructed by three parallel-arranged MPP absorbers with different depths of cavity. A finite element model is established to simulate the acoustic response of the MPP absorber array under normal incidence with high sound intensity by adopting the nonlinear impedance model. The results show that the absorption mechanism of the MPP absorber array is highly subjected to the incident sound pressure. The moderate acoustic pressure excitation enhances the effect of the neighboring MPP absorber compound. If the sound pressure level increases continuously, compared with the MPP absorber array in the linear regime, the spectral peaks on the

absorption curve are smoothed out and the absorption bandwidth with high absorption coefficient ($\alpha > 0.8$) is wider due to the added-mass effect given by the non-resonating sub-cavities. The effect of the panel vibration on the absorption performance of the MPP absorber array is also considered in the proposed model. The measured normal absorption coefficients of a prototype MPP absorber array compare well with the numerical prediction in both linear and nonlinear regimes. The silencing performance of the MPP silencer for controlling the grazing incidence sound wave at moderate intensity in duct is studied. A two-dimensional finite element model is established to access the effect of the nonlinear feature of the orifice on the sound suppression mechanism of the MPP silencer. The silencing performance of the MPP silencer is achieved as a combination of sound reflection induced by panel oscillation and acoustic absorption given by the perforations. The performance of the silencer is improved by the effect of orifice nonlinearity when sound absorption mechanism is dominant. The broader stopband is achieved in the nonlinear regime due to the additional absorption in between the second and third stopbands which is given by the nonlinear effect of perforations.

The fan noise in flow duct can be controlled by using the membrane housing device at the source position directly. This present study investigates the noise reduction mechanism of a tensioned membrane housing device that directly controls the sound radiation from the doublet which is enclosed in the infinitely long duct with presence of a point vortex. The time dependent sound radiation mechanism and the vibro-acoustics coupling mechanism of the systems are studied by adopting the potential theory and matched asymptotic expansion technique. The silencing performance of such passive approach depends on the amplitude and phase of the sound field created

by the doublet and the acoustic pressure induced by the membrane oscillation in order to achieve sound cancellation. Results show that the response of membrane vibration is strongly associated with the flow field induced by the grazing uniform flow and also the fluid loading generated by the inviscid vortex. The geometrical property of cavity and the mechanical properties of the flexible membranes play important role of controlling the performance of the proposed device.

In this study, the flow effects on the acoustic responses of the silencing device are both examined at low Mach numbers.

List of Publications

International Journals

1. **Chiang, Y. K.**, Choy, Y. S. and Tang, S. K. (2017). “Vortex sound radiation in a flow duct with a dipole source and a flexible wall of finite length,” *Journal of the Acoustical Society of America*, 141, 1999-2010.
2. **Chiang, Y. K.** and Choy, Y. S. “Acoustic behaviors of the microperforated panel absorber array in nonlinear regime under moderate acoustic pressure excitation,” *Journal of the Acoustical Society of America* (revised).

Conference Proceedings

1. **Chiang, Y. K.**, Choy, Y. S., Tang, S. K. and Cheng, L. (2014). “Study on aero-acoustic structural interactions in fan-ducted system”, *the 43rd International Congress on Noise Control Engineering*, Melbourne, Australia 16-19 November.
2. Liu, Y., Choy, Y. S. and **Chiang, Y. K.** (2014). “Performance of multiple micro-perforated panels in a duct”, *the 43rd International Congress on Noise Control Engineering*, Melbourne, Australia 16-19 November.
3. **Chiang, Y. K.**, Choy, Y. S. and Tang, S. K. (2015). “Noise control of doublet by membrane housing device in flow duct system”, *Proc. 22nd International Congress on Sound and Vibration*, Florence, Italy 12-16 July.

4. **Chiang, Y. K.** and Choy, Y. S. (2016). “Acoustic performance of microperforated panel absorber array subjected to high intensity sound”, *Proc. 23rd International Congress on Sound and Vibration*, Athens, Greece 10-14 July.

Acknowledgements

*I would like to express my sincere gratitude to my chief supervisor, Dr. **Yat-sze Choy**, for her inspiring ideas and professional guidance throughout the whole period of my study. Over the past four years, she has given me lots of support and encouragement to accomplish my study. I also wish to thank my two co-supervisors Prof. **Li Cheng** and Prof. **Shiu-keung Tang**, who give me inspirations and insightful advices.*

*I would also like to extent my gratitude to Prof. **Xiaodong Jing**, Beijing University of Aeronautics and Astronautics who give me inspiring enlightenment that invaluable for my future development.*

*Special thanks go to my colleagues, Dr. **Yang Liu**, Dr. **Qiang Xi**, **Tiangang Wang**, **Zhibo Wang**, **Long Cheng**, **Long Wei** and **Hon-chiu Ng** for their kind assistance and comments during my study. I also wish to thank the generous help from the technicians in the department.*

*I would like to thank my friends, **Long Wu**, **Yang Meng**, **Ka-yan Chan**, **Shuk-ching Chan**, **Tsz-ting Wong**, **Wing-yee Hau** and **Hei-lam Ma** for their supports.*

Last but most importantly, I would like to deeply thank my parents and family for their love, wave care and encouragement.

Table of Contents

Certificate of Originality	i
Abstract	ii
List of Publications	v
Acknowledgements	vii
Table of Contents	viii
List of Figures	xi
List of Tables	xvi
Nomenclature	xvii

Chapter One

Introduction	1
1.1. Review of Noise Attenuation Methods in Duct.....	1
1.1.1. Dissipative Approaches.....	1
1.1.2. Reactive Approaches.....	3
1.2. Fluid-acoustic-structural Interaction of Flexible Structure in Duct.....	5
1.2.1. Acoustic Properties of Micro-perforated Panel induced by Vortex Shedding	6
1.2.2. Acoustic Response of Membrane induced by Unsteady Flow	9
1.3. Motivations and Objectives	11
1.4. Outline of Thesis	13

Chapter Two

Theoretical and Numerical Studies on Micro-perforated Panel Absorber Array subject to Acoustic Nonlinearity Features of Orifice	15
--	-----------

2.1.	Acoustic Properties of MPP Absorber.....	16
2.2.	Theoretical Modeling of Parallel-arranged MPP Absorber.....	20
2.3.	Finite Element Modeling of Parallel-arranged MPP Absorber	22
2.4.	Numerical Results and Discussion	25
2.4.1.	Parametric Study of MPP Absorber Array	27
2.4.2.	Effects of Incidence Pressure Amplitude.....	34
2.4.3.	Effects of Panel Vibration	41
2.4.4.	Optimization of Structural Parameters of MPP	43
2.5.	Experimental Measurement and Validation	45
2.6.	Conclusions	50

Chapter Three

Performance of Micro-perforated Panel Silencer subject to Orifice Nonlinearity under Grazing Plane Wave Incidence..... 52

3.1.	Finite Element Modeling of MPP Silencer.....	53
3.2.	Numerical Results and Discussion	57
3.2.1.	Noise Attenuation Mechanism	57
3.2.2.	Parametric Study of MPP silencer	62
3.2.2.1.	Structural Properties of Panel.....	63
3.2.2.2.	Parameters of MPP.....	68
3.3.	Conclusions	71

Chapter Four

Theoretical Studies on the Sound Attenuation Mechanism of a Tensioned Membrane Housing Device in a Flow Duct..... 73

4.1.	Theoretical Modeling of Membrane Housing Device	74
4.1.1.	Vortex Dynamics and Membrane Vibrations	75
4.1.2.	Far-field Sound Radiation.....	81
4.2.	Numerical Results and Discussion	83
4.2.1.	Fluid-structural Interactions.....	84
4.2.2.	Far-field Acoustic Pressure Radiation	90

4.2.3. Noise Attenuation Mechanism	93
4.3. Conclusions	101

Chapter Five

Conclusions and Recommendations	103
5.1. Conclusions	103
5.2. Recommendations for Future Development.....	106
References.....	109

List of Figures

Figure 1.1	Near-field sound pressure level of the unducted fan engine GE-36. ..	6
Figure 1.2	Schematic diagram of the advanced ducted propeller with lining treatment.	7
Figure 1.3	Acoustic circulation around orifice.	9
Figure 2.1	Acoustic properties of MPP absorber at different incidence sound pressure level. (a) Acoustic absorption; (b) Acoustic resistance; (c) Acoustic reactance.	18
Figure 2.2	Variations of the acoustic properties of MPP absorber at different incidence sound pressure level in percentage. (a) Acoustic absorption; (b) Acoustic resistance; (c) Acoustic reactance.	19
Figure 2.3	Schematic diagram of the MPP absorbers. (a) Single MPP absorber; (b) Dual MPP absorber array; (c) Triple MPP absorber array.	20
Figure 2.4	Schematic diagram of the parallel-arranged MPP absorber array with three partitioned sub-cavities.	22
Figure 2.5	Comparison of the predicted normal incidence absorption coefficients of the single MPP absorber by the finite element model and the analytical solutions. (a) Linear; (b) Nonlinear at $SPL_{incident} = 100dB$; (c) Nonlinear at $SPL_{incident} = 120dB$. The properties of the MPP A are $d = t_{mpp} = 0.5mm$ and $\sigma = 1\%$. The cavity depth is $D_s = 100mm$	27
Figure 2.6	Effect of perforation ratio on the normal incidence absorption coefficients of MPP absorber array at the nonlinear regime, $SPL_{incident} = 110 dB$. (a) MPP B with $\sigma = 5.5\%$; (b) MPP C with $\sigma = 3.3\%$. (—) MPP absorber array; (-·-) Single MPP absorber with $D_s = 100mm$; (- -) Single MPP absorber with $D_s = 50mm$; (- - -) Single MPP absorber with $D_s = 25mm$	30

Figure 2.7	Frequency range for half-absorption. (a) Upper frequency limits; (b) Lower frequency limits; (c) Half-absorption bandwidth.	31
Figure 2.8	Effect of orifice diameter on the normal incidence absorption coefficients of MPP absorber array at the nonlinear regime, $SPL_{incident} = 110$ dB. (—)MPP B with $d = 1$ mm; (---) MPP D with $d = 0.6$ mm.	32
Figure 2.9	Frequency range for half-absorption. (a) Upper frequency limits; (b) Lower frequency limits; (c) Half-absorption bandwidth.	32
Figure 2.10	Effect of panel thickness on the normal incidence absorption coefficients of MPP absorber array at the nonlinear regime, $SPL_{incident} = 110$ dB. (—)MPP B with $t_{mpp} = 1$ mm; (---) MPP E with $t = 0.5$ mm.	33
Figure 2.11	Frequency range for half-absorption. (a) Upper frequency limits; (b) Lower frequency limits; (c) Half-absorption bandwidth.	33
Figure 2.12	Comparison of the normal incidence absorption coefficients of MPP F between the linear and nonlinear regimes. (a) Single MPP absorber; (b) Triple MPP absorber array.	35
Figure 2.13	Acoustic impedance of the single MPP absorber for MPP F. (a) Specific acoustic resistance; (b) Specific acoustic reactance. (—) Linear; (---) $SPL_{incident} = 100$ dB; (- - -) $SPL_{incident} = 110$ dB; (- · -) $SPL_{incident} = 120$ dB.	37
Figure 2.14	Acoustic impedance of the parallel-arranged MPP absorber array for MPP F. (a) Specific acoustic resistance; (b) Specific acoustic reactance. (—) Linear; (---) $SPL_{incident} = 100$ dB; (- - -) $SPL_{incident} = 110$ dB; (- · -) $SPL_{incident} = 120$ dB.	39
Figure 2.15	Acoustic properties of the MPP absorber array for MPP G. (a) Absorption coefficient; (b) Specific acoustic resistance; (c) Specific acoustic reactance. (—) Triple MPP absorber array in linear; (- - -)	

	Triple MPP absorber array at $SPL_{incident} = 120$ dB; (---) Single MPP absorber at $SPL_{incident} = 120$ dB.	41
Figure 2.16	Comparison of the acoustic responses of the MPP absorber array between flexible and rigid MPP in the nonlinear regime. The results are obtained from MPP F. (a) Normal incidence absorption coefficients; (b) and (c) Amplitude of the panel vibrating velocities; (d) and (e) The acoustic intensity vector in the duct.	43
Figure 2.17	Optimal spectrum for the single MPP absorber and MPP absorber array in the nonlinear regime. (a) The normal absorption coefficients at optimal surface density and bending stiffness. The subfigures below show the optimal half-absorption bandwidth contour as a function of surface density M_s and bending stiffness B . (b) Single MPP absorber; (c) Triple MPP absorber array.	45
Figure 2.18	Experimental setup for measuring the normal incidence absorption coefficient by using the two-microphone method.	46
Figure 2.19	Comparison between the numerical predictions obtained from the finite element model and the experimental results of the MPP absorber array. (a) Linear; (b) Nonlinear at $SPL=110$ dB. The MPP is made of stainless steel with parameters $t_{mpp} = 0.4$ mm, $d = 0.65$ mm and $\sigma = 1.76\%$. The depths of three sub-cavities are $D_1 = 50$ mm, $D_2 = 99$ mm and $D_3 = 25$ mm.	48
Figure 2.20	Comparison between the numerical predictions obtained from the finite element model and the experimental results of the MPP absorber array. The MPP is made of stainless steel with parameters $t_{mpp} = 0.4$ mm, $d = 1.08$ mm, $\sigma_{1,2,3} = 0.85\%$, 1.15% and 0.85% . The depths of three sub-cavities are $D_1 = 50$ mm, $D_2 = 99$ mm and $D_3 = 25$ mm.	49
Figure 3.1	Two-dimensional configuration of the MPP silence.	54
Figure 3.2	Comparison of TL of the MPP silencer at different incidence sound pressure level for MPP 1 of $M_s = 2$ and $B = 0.008$	58

Figure 3.3	Time-averaged acoustic intensity at $f^* = 475$ Hz.	59
Figure 3.4	Time-averaged acoustic intensity at $f^* = 635$ Hz.	60
Figure 3.5	Time-averaged acoustic intensity at $f^* = 965$ Hz.	60
Figure 3.6	Time-averaged acoustic intensity at $f^* = 1200$ Hz.	61
Figure 3.7	Acoustic response of the MPP silencer for MPP 1 of $M_s = 2$. (a) Reflection coefficient; (b) Absorption coefficient.	62
Figure 3.8	TL achieved by MPP silencer with different surface density for MPP 2. (a) $M_s = 3$; (b) $M_s = 5$; (c) $M_s = 7$	64
Figure 3.9	Acoustic response of MPP silencer with different surface density for MPP 2. Left column represents the reflection coefficient and the right one denotes the absorption coefficient. (1) $M_s = 3$; (2) $M_s = 5$; (3) $M_s = 7$	65
Figure 3.10	TL achieved by MPP silencer with different bending stiffness for MPP 2. (a) $B = 0.05$; (b) $B = 0.15$; (c) $B = 0.25$	67
Figure 3.11	Acoustic response of MPP silencer with different bending stiffness for MPP 2. Left column represents the reflection coefficient and the right one denotes the absorption coefficient. (1) $B = 0.05$; (2) $B = 0.15$; (3) $B = 0.25$	68
Figure 3.12	Acoustic response of MPP silencer with different length of panel for MPP 3. Left column represents the results of $L = 2.5$ and the right one denotes the results of $L = 5$. (1) TL; (2) Reflection coefficient; (3) Absorption coefficient.	69
Figure 3.13	Acoustic response of MPP silencer with different panel thickness for MPP 3. Left column represents the results of $t_{mpp} = 4$ mm and the right one denotes the results of $t_{mpp} = 0.5$ mm. (1) TL; (2) Reflection coefficient; (3) Absorption coefficient.	71
Figure 4.1	Two-dimensional schematic diagram of the membrane housing device in flow duct.	75

Figure 4.2	Effects of cavity height and mass density on the vortex trajectories. (a) $m = 50$; (b) $m = 100$; (c) $m = 150$	85
Figure 4.3	Vibration of lower membrane. The first row represents the variation of displacement while the second row represents the velocity at (a) $\tau=0.498$; (b) $\tau=1.239$; (c) $\tau=2.971$	87
Figure 4.4	Vibration displacement of lower membrane for $h_c=0.5$. The first row represents the modal magnitude while the second row represents the time variation of vibration displacement of lower membrane of (a) $m=50$; (b) $m=100$; (c) $m=150$	88
Figure 4.5	Effect of doublet strength and initial vortex height on the vortex dynamics for $h_c = 0.8$. (a) $\mu_0 = 3$; (b) $\mu_0 = 6$; (c) $\mu_0 = 9$	90
Figure 4.6	Effect of mean flow speed on the sound radiation. (a) Root mean square value of acoustic pressure radiation; (b) Maximum sound power radiation.	93
Figure 4.7	Effect of cavity height on the sound radiation of membrane. (a) $U = 0.05$; (b) $U = 0.1$; (c) $U = 0.2$. (---) p_{dou} ; (—) p_{mem} for $h_c = 0.4$; (---) p_{mem} for $h_c = 0.6$; (-·-) p_{mem} for $h_c = 0.8$	95
Figure 4.8	Effect of mass ratio on the sound radiation of membrane. (a) $U = 0.05$; (b) $U = 0.1$; (c) $U = 0.2$. (---) p_{dou} ; (—) p_{mem} for $m = 80$; (---) p_{mem} for $m = 100$; (-·-) p_{mem} for $m = 120$	97
Figure 4.9	Effect of tension on the sound radiation ($\mu_0 = 8, f = 0.34, h_c = 0.7, m = 90$). (a) $U = 0.05$; (b) $U = 0.1$; (c) $U = 0.2$. (---) p_{dou} ; (—) p_{mem} for $T = 20$; (---) p_{mem} for $T = 40$; (-·-) p_{mem} for $T = 60$	98
Figure 4.10	Silencing performance of proposed membrane housing device. (a) Spectrum of inserting loss (IL). (b) and (c) are the components of sound pressure radiation for $c_T = 0.577$ and $c_T = 0.471$ respectively. (—) Total sound pressure radiation; (- - -) Pressure radiated by vortex; (-·-) Pressure radiated by membrane oscillation; (---) Pressure radiated by doublet.	100

List of Tables

<i>Table 2.1</i>	Parameters of MPPs used in the numerical investigations.	26
<i>Table 3.1</i>	Parameters of MPPs used in MPP silencer.	57

Nomenclature

Symbol	Description
A_+	Complex magnitude of downstream going wave
A_-	Complex magnitude of upstream going wave
a^*	Dimensional duct height, with unit m
a	Dimensionless duct height
B^*	Dimensional bending stiffness of the plate, with unit $\text{m}^2\text{kg/s}^2$
B	Dimensionless bending stiffness of the plate, where $B = B^*/\rho_0^*(c_0^*)^2(h^*)^3$
b	Distance between orifices, with unit mm
c_T	Wave speed of the membrane $c_T=(T/m)^{0.5}$
c_0^*	Dimensional sound speed, with unit m/s
c_0	Dimensionless sound speed
D^*	Dimensional damping coefficient, with unit kg/ms
D	Dimensionless damping coefficient, where $D = D^*/a^*U_{max}^*\rho_0^*$
D_s	Cavity depth of single MPP absorber, with unit mm
$D_{1,2,3}$	Sub-cavity depths of triple MPP absorber array, with unit mm
d	Orifice diameter, with unit mm
f^*	Dimensional frequency, with unit Hz

f	Dimensionless frequency, where $f = f^* a^* / U_{max}^*$
h^*	Dimensional total height of MPP absorber, with unit m
h	Dimensionless total height of MPP absorber
h_c^*	Dimensional depth of side branch backing cavity, with unit m
h_c	Dimensionless depth of side branch backing cavity, where $h_c = h_c^* / a^*$
IL	Insertion loss, with unit dB
k_0	Wavenumber $k_0 = \omega / c_0$
L^*	Dimensional length of MPP, with unit m
L	Dimensionless length of MPP, where $L = L^* / a^*$
M	Mach number
M_s^*	Dimensional surface density of MPP, with unit kg/m ²
M_s	Dimensionless surface density of MPP, where $M_s = M_s^* / \rho_0^* h^*$
m^*	Dimensional mass density of the membrane, with unit kg/m ²
m	Dimensionless mass density of the membrane, where $m = m^* / \rho_0^* a^*$
n	Normal direction
p	Acoustic pressure
p_{cav}	Acoustic pressure on the backing cavity side

p_{dou}	Sound radiation of doublet
p_{duct}	Acoustic pressure on the duct side
p_i	Incident sound wave
p_{in}	Amplitude of incidence sound wave
p_{mem}	Sound radiation of membrane vibration
p_r	Reflected sound wave
T^*	Dimensional tension of membrane, with unit kg/s^2
T	Dimensionless tension of membrane, where $T = T^*/a^*(U_{max}^*)^2\rho_0^*$
TL	Transmission loss, with unit dB
t	Time in far-field
t_{mpp}	Thickness of MPP, with unit mm
U	Mean flow speed
u	Particle velocity
u_p	Dimensional normal vibration velocity of panel, with unit m/s
u_p'	Dimensionless normal vibration velocity of panel, where $u_p' = u_p/c_0^*$
v_0	Peak velocity in the orifice
v_{dou}	Fluid velocity of doublet

v_{mem}	Vibrating velocity of membrane
v_{vortex}	Vortex velocity
v_x, v_y	Longitudinal and transverse particle velocities
W	Acoustic power
W_{dou}	Complex potential of doublet
W_{mem}	Complex potential of membrane vibration
w	Displacement of panel in y-direction
\hat{x}, \hat{y}	Unit vector
(x_d, y_d)	Location of the doublet
(x_e, y_e)	Initial position of the inviscid vortex
(x_v, y_v)	Instantaneous position of vortex
$\Delta x, \Delta y$	Spatial size for x- and y-direction
Z	Specific acoustic impedance
Z_{resist}, Z_{react}	Linear specific acoustic resistance and reactance
$Z_{resist,NL}, Z_{react,NL}$	Nonlinear specific acoustic resistance and reactance
α	Absorption coefficient
β	Reflection coefficient
η	Normal displacement of panel
η_u, η_l	Displacement of the upper and lower membranes

τ	Time
$\Delta\tau$	Temporal step size
μ_0	Amplitude of source strength of doublet
ν	Coefficient of viscosity
ω	Angular frequency $\omega = 2\pi f$
Γ	Vortex circulation
σ	Perforation ratio
ρ_0^*	Dimensional air density, with unit kg/m^3
ρ_0	Dimensionless air density
ϕ	Velocity potential
ϕ_i	Velocity potential of the incident sound wave
γ	Time function
ξ_x, ξ_y	Normalized impedance in x - and y -direction

Chapter One

Introduction

1.1. Review of Noise Attenuation Method in Duct

In present day, products with the installation of fans and blowers like the air conditioning system and hair dryer are widely used to improve the quality of life of human beings. Generally, the fan is connected with the ductwork, which is defined as the fan-ducted system of the present study, in order to deliver the air. The aerodynamic noise arise from flow separation on the impeller blade and also the flow-field interactions between the rotor and stator (Sharland, 1964; Longhouse 1977) in the fan-ducted system is one of the major annoyance in our daily lives. The noise control of the fan noise at low blade-passage frequency (BPF) is still a challenge. Numerous noise reduction methods for duct noise control were proposed by researchers.

1.1.1. Dissipative Approaches

Duct lining (Allard, 1993; Ingard, 1995; Beranek and Ver, 2006) is the traditional method adopted in the air conditioning system. The noise is dissipated by the fibrous materials by converting the acoustic energy into heat due to the friction between the air particle and the porous material. A desirable absorption performance can be achieved by the dissipative approach at the mid to high frequencies. However, at low frequencies, such absorber is ineffective due to the highly impedance mismatch at the interface of the air and the absorption material. In order to reduce the large

characteristic impedance of the conventional absorber, Choy *et al.* (2003, 2009, 2012) suggested to fill the pores of the absorber with low density helium gas such that a better sound penetration through the air-absorber interface can be achieved. However, the use of fibrous material would bring about the environmental problem such as the accumulation of dirt in the pores (Fuchs, 2001a; b).

In order to achieve better absorption performance at low frequency range without bringing the environmental problem, the micro-perforated panel (MPP) absorber is proposed as a fiber-free dissipative approach for broadband noise control. MPP absorber is composed of a plate with numerous small orifices and a backing cavity. The acoustic energy can be absorbed by the MPP due to the friction between the panel and the oscillating air particle in the orifice. Bolt (1947) analyzed the acoustic response of the perforated panel. Later, Maa (1975, 1998) further studied the theory and the acoustic properties of the MPP absorber in the linear regime by an empirical impedance model without including the effect of panel vibration. Lee *et al.* (2005) then investigated the effect of the panel vibration on the acoustic performance of MPP absorber. An additional absorption peak was observed due to the resonance of panel (Toyoda *et al.*, 2010; Bravo *et al.*, 2012).

Although the MPP absorber performs well with high absorption at low frequencies, its effective frequency band is relatively narrower than that achieved by porous materials. In order to further extend the absorption bandwidth, double-layer (Maa, 1987; Zhang and Gu, 1998) or even multiple-layer MPP absorbers (Lee and Chen, 2001; Lee and Kwon, 2004; Mu *et al.*, 2011) are suggested. Sakagami *et al.* (2006) investigated the absorption behaviors of the double-layer MPP absorber (or double-

leaf MPP absorber) theoretically under the normal incidence excitation. The absorption mechanism of the double-layer MPP absorber was found to be a combination of resonator type absorption at mid-to-high frequencies and acoustic flow resistance at low frequencies. Therefore, a considerable supplementary absorption can be obtained by the double-layer MPP absorber. Besides the multiple-layer MPP absorber, the MPP absorbers with different frequency characteristics can also be arranged in parallel to form a MPP absorber array. Zha *et al.* (1994) investigated the normal incidence absorption performance of the MPP absorber array with two sub-cavities of different cavity depth based on the Maa's impedance model. Wang and Huang (2011) then established a finite element model to further investigate the acoustic properties of the MPP absorber array. They found that a broad absorption bandwidth can be achieved by the device based on the parallel absorption mechanism.

1.1.2. Reactive Approaches

Apart from the dissipative approach, the duct noise can also be controlled by reactive silencers. The expansion chamber with an expanded or contracted cross-sectional area is one of the classical devices used to control duct noise. The noise reduction can be achieved by sound reflection. The performance of the expansion chamber greatly depends on the expansion ratio of the cross section area and the length of chamber. However, the performance of the expansion chamber is degraded due to the existence of passband on transmission loss (TL). In order to improve the noise suppression performance, multiple chambers was proposed (Yi and Lee, 1986; Ji, 2005). However, unavoidable pressure loss would be induced due to the change of area and thus increases the power consumption of the fans.

Helmholtz resonator is another commonly utilized silencer. The resonance frequency of the resonator is determined by the stiffness effect of the resonator cavity and the air inertia in the neck. At the resonance frequency, the transmission coefficient is zero. However, an effective noise attenuation can only be obtained for a very narrow frequency range. Multiple resonators arranged in parallel were developed in order to broaden the effective bandwidth (Seo and Kim, 2005; Li *et al.*, 2007). However, the device would be too bulky for the low frequency noise control.

Besides the traditional reactive device, Huang (1999; 2002) introduced an advanced silencer with flexible structures, which is named as drum-like silencer, for duct noise control. The drum-like silencer consists of two stretched membranes in light mass and two side branch backing cavities. The harmonic responses of the membrane were predicted analytically. The strong vibro-acoustic coupling was found in the system. The incident sound wave in the duct would excite the membrane into vibration when it passes over the membrane section. Part of the acoustic wave is reflected back to the upstream due to the sound radiation induced by the membrane oscillation. As a result, the transmitted wave to the downstream is reduced according to the principle of energy conservation. The prototype device has been examined successfully without flow (Choy and Huang, 2002) by experiments. Choy and Huang (2003) improved the drum-like silencer by filling the cavity with helium gas. The lighter gas helps to release the massive loading acting on the membrane. Thus, an enhancement of noise reduction at low frequencies is achieved.

Later, Huang (2006) utilized a low mass plate with high bending stiffness as the replacement of the tensioned membrane to ease the implementation process of silencer.

By comparing with the performance of the drum-like silencer, a wider stop-band can be achieved by the plate silencer due to the change of intermodal acoustic interference between the odd and even *in vacuo* vibration modes. The optimization study of the plate silencer with clamped support was conducted by Wang *et al.* (2007). They showed that the stop-band can reach to 6 for the optimal case. The demand on the tension applied of the drum-like silencer and the strength to mass ratio of the plate silencer is relatively high. In order to ease the requirements of the plate silencer, perforations are introduced on the panel to provide supplementary sound absorption (Wang *et al.*, 2012). The additional absorption given by the perforations helps to maintain the silencing performance at the frequency with insufficient sound reflection.

1.2. Fluid-acoustic-structural Interactions of Flexible Structures in Duct

From the literature mentioned above, the acoustic response and the silencing performance of the noise attenuation approaches were investigated in the system without considering the flow effect. However, in the fan-ducted system, the flow effect is an important element that should be taken into account. The acoustic behaviors of the silencing device especially for the device with flexible structures would be changed due to the interactions between the flow field, acoustic field and the structural vibration. The fluid-acoustic-structural interactions of the flexible structures influence the acoustic behaviors of the silencing device from two aspects: one is changing the acoustic properties of the device due to vortex formation, another one is changing the acoustic responses of the silencer due to the existence of vortex. The effects of the fluid-acoustic-interactions on the acoustic response of the device

with flexible structures induced by the process of vortex formation and the presence of turbulent flow were observed from the MPP absorber and the silencer with flexible membrane respectively.

1.2.1. Acoustic Properties of Micro-perforated Panel induced by Vortex shedding

The aircraft engine is one of the fan-ducted system. The engine noise which composed of the jet noise due to the strong turbulence and the fan noise induced by the boundary layer development on the fan blades is the major sound source of aircraft. Huff (2013) conducted a near-field acoustic measurement on the unducted fan engine GE-36 at different angles. The sound pressure level at BPF exceeds 110 dB as shown in Figure 1.1.

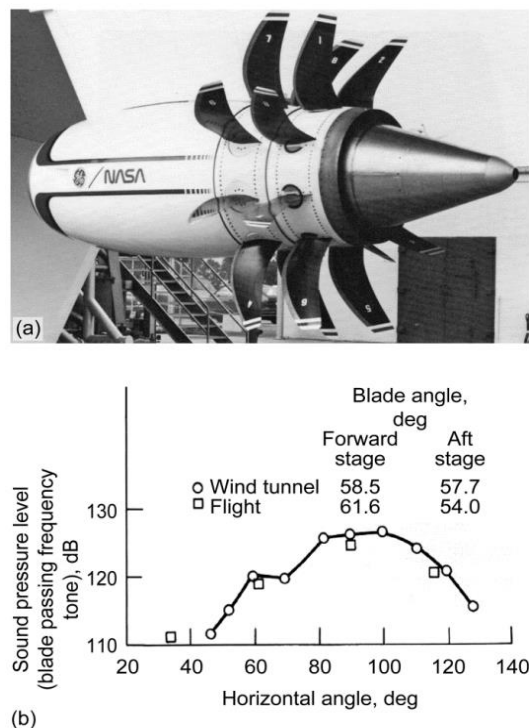


Figure 1.1 Near-field sound pressure level of the unducted fan engine GE-36. (Huff, 2013)

The acoustic liner is usually adopted on the nacelle enclosing the fan in order to reduce the fan noise. It is mainly installed in the inlet, fan case and fan duct sections as shown in Figure 1.2.

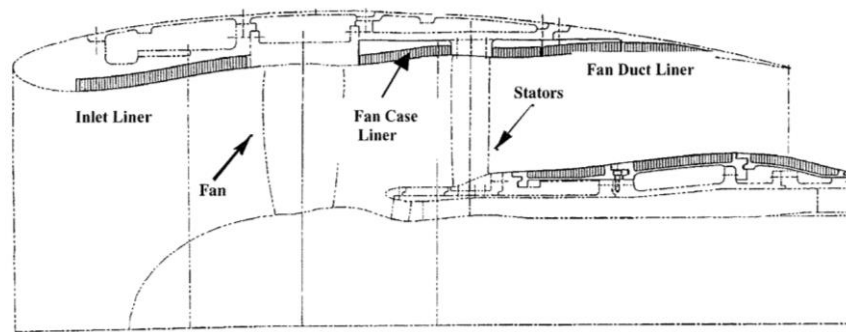


Figure 1.2 Schematic diagram of the advanced ducted propeller with lining treatment. (Bielak *et al.*, 2002)

In such situation, the MPP absorber would be exposed to the environment at high sound pressure level, and hence, it could affect the acoustic properties of the MPP absorber. A number of researchers have studied the acoustic behaviors of the orifice when it is subjected to high sound intensity (Sivian, 1935; Thurston *et al.*, 1957). From the flow visualizations, Salikuddin and Ahuja (1983) observed the flow separation and the jet formation at the exit of orifice. The acoustic energy converted to the vortical energy due to the vortex ring formation. Hence, such acoustic nonlinearity of the orifice changes the acoustic performance of the MPP due to the process of vortex shedding.

Several studies were conducted to investigate the nonlinear effects on the acoustic impedance of the orifice induced by the jet formation at the orifice (Ingard and Labate, 1950). Ingard and Ising (1967) studied the nonlinear behavior of acoustic impedance of an orifice in the absence of mean fluid flow by measuring the air particle velocity

in the orifice and the acoustic pressure fluctuations producing the flow simultaneously. They showed that the acoustic resistance increases proportionally with the flow velocity in the orifice, and the acoustic reactance decreases at high sound pressure. Cummings and Eversman (1983) established a simple quasi-steady model by introducing the empirical vena contracta coefficient to explain the acoustic energy dissipation mechanism. Afterward, Cummings (1986) adopted the numerical time-domain (NTD) model to examine the acoustic power losses induced by the production of vorticity at the orifice lip in the presence of high-amplitude sound wave. The equation of motion for the air is numerically integrated in time domain, and hence, the details of the pressure-time history of the wave transmitted through the orifice can be predicted. Hersh *et al.* (2003) further developed the quasi-steady model with the use of discharge coefficient as the nonlinear parameter to predict the nonlinear acoustic impedance for both single and multiple orifices over a wide range of sound pressure levels and frequencies. Instead of using the quasi-steady model with the empirical parameter, Maa (1996) also suggested a nonlinear acoustic impedance which is a combination of the linear impedance and the end correction which is directly related to the air particle velocity in the orifice. Later on, Tayong *et al.* (2010) proposed another nonlinear impedance model in terms of the Mach number in the perforation based on the dimensional analysis and Forchheimer's law in order to study the acoustic behavior of the MPP absorber at high sound excitation. Park (2013) introduced an empirical nonlinear impedance model which considers all geometric parameters of the MPP and the incident pressure based on the Buckingham Pi theorem. He calculated the flow velocity in the orifice from the incident pressure by using the Bernoulli's law and the acoustic circuit analogy. The results showed that a better

sound absorption can be achieved by the single MPP absorber at high sound pressure level. Both the quasi-steady model and empirical impedance model focus on the nonlinear characteristic of the acoustic impedance without describing the flow details around the orifice. Therefore, Jing and Sun (2000) established a discrete vortex model to study the vortex shedding process at the orifice at high intensity sound. Dai *et al.* (2012) further extended the discrete vortex model to examine the acoustic properties of the rectangular orifice of Helmholtz resonator at high sound pressure in the presence of grazing flow.

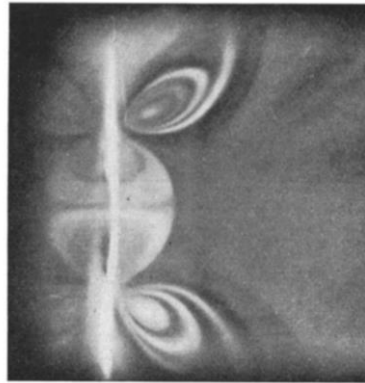


Figure 1.3 Acoustic circulation around orifice. (Ingard and Labate, 1950)

1.2.2. Acoustic Response of Membrane induced by Unsteady Flow

In the fan-ducted system such as the ventilation system, the time-varying pressure fluctuation induced by the unsteady flow is another flow effect that changes the acoustic response of the silencing device with flexible boundaries. In the work conducted by Choy and Huang (2005), the interactions between the membrane of drum-like silencer and the grazing uniform flow was investigated. The idea of drum-like silencer can also be employed to attenuate the sound radiation from the axial fan directly at the source position. The device is so called a membrane housing device

(Liu *et al.*, 2014). There is a number of aerodynamic noise sources created during the fan operation. Generally speaking, there are three types of noise sources in any machine with moving blades, monopole from the blade motion, dipole from the fluctuating forces on blades, and quadrupole emanating from the core of turbulence jets (Lighthill, 1952; Curle, 1955; Ffowcs Williams and Hawkings, 1969). Focusing on the operation of axial fan at subsonic speeds, it is found that the dominant noise source is often the unsteady pressure fluctuation arising from the interaction between the rotating blades and stationary blades, which can be characterized as a dipole source. The performance of using the membrane housing silencing device in controlling subsonic axial fan radiated tonal noise of dipole nature was investigated by Liu *et al.*, (2012) analytically by simply modelling the flow as uniform. However, when the fan is operating, the turbulent flow is induced, and hence it will interact with the flexible structures of the silencer in a more intricate vibro-acoustic mechanism. Ostoich *et al.* (2013) utilized a direct numerical simulation approach to study the coupled fluid-structural interactions between the turbulent boundary layer and the thin steel panel. Such approach examined the coupled fluid-structural interaction by matching nodes at the interface between the fluid and structural domains, which are computed by the compressible Navier-Stokes equations and finite-strain finite element solver respectively. Zhang and Bodony (2016) further developed the simulation technology to estimate the discharge coefficient and predict the acoustic impedance of the honeycomb liner in the presence of grazing laminar and turbulent boundary layers as well as the incident sound waves. The effect of turbulence can also be studied by the semi-analytical approach which simply models the turbulent eddies as discrete point vortices (Howe, 2003). Tang *et al.* (2005) adopted the simplification of the turbulent

eddies by using an inviscid vortex with grazing flow in order to study the fluid-acoustic-structural interactions including the vortex dynamics and the aero-acoustic radiation between the unsteady flow and the flexible membrane without backing cavity. Later, Tang (2011) further investigated the effect of existence of vortex on the vibro-acoustic coupling mechanism of the drum-like silencer in the flow duct at low Mach number based on the discrete vortex model.

1.3. Motivations and Objectives

The present study is focused on the investigation of the complicated mechanism of fluid-acoustic-structural interaction between the flow and flexible structures and also the acoustic performance of the silencing devices in the fan-ducted system. The acoustic behavior of the device can be influenced in two different ways: 1) one way is to directly change the acoustic properties of the device due to the jet formation. For this part, the study would mainly focus on the effect of the induced nonlinearity on the acoustic performance of the device; 2) another way is to change the structural vibration of the device due to the additional loading given by the presence of vortex. For this, the fluid-structural-acoustic interaction and sound radiation mechanism of the device will be investigated.

The first phenomenon can be observed by using the micro-perforated panel in an environment at moderate or high acoustic pressure like the aircraft engine. From the literatures, different models were established to study the effect of the nonlinear acoustic property of the orifice on the normal incidence absorption performance of the single MPP absorber. However, little attention have been paid to the effect of

orifice nonlinearity on the acoustic response of the promising MPP absorber array in parallel arrangement. As such, this study is presented for the purpose of investigating the acoustic behaviors of the MPP absorber array in the nonlinear regime. Also, the effect of the acoustic excitation and the effect of structural vibration on the absorption mechanism of the MPP absorber array is examined by establishing a finite element model.

Besides, the micro-perforated panel can be adopted in the plate silencer to control the grazing incidence sound wave in duct in order to improve the silencing performance by providing supplementary sound absorption. Most of the studies presented in previous sections were conducted in the linear regime. The acoustic performance of the MPP silencer on the grazing incidence sound wave at high amplitude has not been studied. Therefore, another purpose of the current study is to assess the sound suppression mechanism of the MPP silencer with the nonlinear acoustic features of orifice for controlling the grazing incidence sound wave at moderate intensity in duct.

The second phenomenon can be found by adopting the membrane housing device in the fan-ducted system with turbulent flow like the ventilation system. The investigation on the performance of a membrane housing device that is used to control the fan noise directly at the source position was only conducted in the frequency domain. The time-dependent excitation from the fan and response of membranes were neglected. Also, the influence of flow turbulence and the corresponding unsteady flow sound generation mechanism were not examined. A simplified theoretical aeroacoustic model of the membrane housing device is established in current study to investigate the complicated fluid-acoustic-structural interactions and the noise

attenuation mechanism of the membrane housing device in the presence of a point vortex. The proposed theoretical model has the following distinct features. (a) It is different from previous studies (Tang, 2011) which were mainly focused on the vortex-membrane interactions, in that a dipole sound source is considered, which leads to a more complicated fluid-structural interactions. Moreover, the noise attenuation mechanism of the membrane housing device in controlling the dipole source is studied with different design parameters. (b) Inside the backed-cavity, a non-uniform fluid pressure is considered instead of assuming an even pressure distribution in order to simulate a more realistic transient response of the fully coupled membrane-cavity system. In order to examine the time varying fluid field corresponding to the dipole nature of fan noise, it is described as a doublet which is composed of two sources with anti-phase volume flow rate. The unsteady turbulent eddy is represented by an inviscid point vortex for simplification. In addition, finite difference time domain (FDTD) approach (Kowalczyk and Van Walstijn, 2008) was adopted to explore the non-uniform fluid pressure distribution inside both the upper and lower cavities.

1.4. Outline of Thesis

In chapter two, two-dimensional theoretical and finite element models of the parallel-arranged MPP absorber array are presented in order to study the effects of acoustic nonlinearity features of orifice on the acoustic properties of the parallel MPP absorber array. The acoustic property of the MPP absorber at different incidence sound pressure level is investigated experimentally at low acoustic Mach numbers. Such device is highly subjected to the acoustic excitation. The effects of the incident pressure

amplitude on the absorption mechanism of the MPP absorber array are discussed. Also, the effect of panel vibration on the absorption performance of the absorber is presented. The parametric study and optimization are conducted for the purpose of the design of MPP absorber array.

In chapter three, the finite element model of the MPP silencer is established. The MPP silencer is subject to grazing plane wave at high sound intensity. The sound suppression mechanism of the MPP silencer with the nonlinear acoustic features of orifice in low acoustic Mach number is discussed and presented with the numerical results. The effect of the sound pressure amplitude on the acoustic behavior of the MPP silencer is explained in terms of the parameters of the MPP silencer including the orifice diameter, length of panel and the cavity depth.

In chapter four, the theoretical formulations of the membrane housing device in flow duct in low Mach number are presented. The effect of the cavity depth and the effect of the initial vortex height on the fluid-structural interactions are shown. The sound radiation mechanism of the system is examined with different flow speeds. Moreover, the noise attenuation mechanism of the membrane housing device that is used to reduce the dipole noise directly at the source location is described. The effects of the depth of backing cavity and the membrane properties including the tension applied and mass ratio of the membrane on the sound pressure radiation are studied numerically. Based on the noise suppression mechanism, the performance of such silencer is presented.

In chapter five, the conclusions and recommendations for future development are given.

Chapter Two

Theoretical and Numerical Studies on Micro-perforated Panel Absorber Array subject to Acoustic Nonlinearity Features of Orifice

In recent years, micro-perforated panel has been widely utilized for noise control especially at low frequency since the perforations of the panel provide sufficient acoustic resistance and low reactance for sound absorption. In many situations, the MPP absorber is exposed to high sound intensity. Salikuddin and Ahuja (1983) observed from flow visualizations that a jet forms at the exit of orifice when sound wave at high amplitude transmits through the perforated plate. Hence, the acoustic nonlinearity of orifice induced by the vortex shedding would affect the acoustic properties of the MPP absorber. This chapter describes the acoustic properties of MPP absorbers under different acoustic excitation levels, i.e., from 50 dB to 120 dB. When the acoustic excitation is below 130 dB, the acoustic Mach number M is low, i.e., $M \ll 1$. For low Mach number, the acoustic field can be regarded as linear acoustics (Crocker, 1998).

In order to extend the absorption bandwidth of the single MPP absorber, Zha *et al.* (1994), Wang and Huang (2011) proposed the MPP absorber array in parallel arrangement. They studied the absorption mechanism of the device in linear regime. The results showed that a wider absorption bandwidth can be achieved by the MPP absorber array based on the parallel absorption mechanism. The present study mainly

focuses on the device of MPP absorber array instead of a single MPP absorber in order to investigate the effect of the acoustic nonlinearity of orifice on the parallel absorption mechanism.

In this chapter, the theoretical and finite element models of the parallel-arranged MPP absorber array are presented in order to study the effects of acoustic nonlinearity features of orifice on the acoustic properties of the parallel MPP absorber array with normal incidence pressure at low Mach number. With the numerical model developed, the absorption performance and behaviors of the MPP absorber array are predicted.

2.1. Acoustic Properties of MPP Absorber

Maa (1975, 1998) studied the theory of MPP absorber and also proposed an empirical impedance model to describe the acoustic properties of MPP absorber. The linear specific acoustic impedance can be written as

$$Z_L = Z_{resist} + Z_{react} , \quad (2.1)$$

where Z_{resist} and Z_{react} are the linear specific acoustic resistance and reactance respectively, which are expressed as

$$\begin{aligned} Z_{resist} &= \frac{32vt_{mpp}}{\sigma\rho_0c_0d^2} \left[\left(1 + \frac{K^2}{32} \right)^{1/2} + \frac{\sqrt{2}}{8} K \frac{d}{t_{mpp}} \right] \\ Z_{react} &= \frac{i\omega t_{mpp}}{\sigma c_0} \left[1 + \left(9 + \frac{K^2}{2} \right)^{-1/2} + 0.85 \frac{d}{t_{mpp}} \right] , \end{aligned} \quad (2.2)$$

where $K = d\sqrt{\omega\rho_0/4\nu}$, ν is the coefficient of viscosity, c_0 is the sound speed, ρ_0 is the density of air, $\omega = 2\pi f$ denotes the angular frequency, f represents the frequency, d is

the orifice diameter, b is the distance between orifices, t_{mpp} denotes the thickness of MPP and $\sigma = 0.25\pi(d/b)^2$ is the perforation ratio in percentage. The effect of incidence acoustic pressure on the properties of MPP absorber is not considered in Eq. (2.2). However, Ingard and Ising (1967) found that the acoustic impedance of an orifice would change with the incidence pressure at high sound pressure. Figure 2.1 shows variations of acoustic absorption and impedance of a single MPP absorber with cavity depth $D_s = 100$ mm measured experimentally under different acoustic incidence pressure. The experimental setup is described in Sec. 2.5. The parameters of the MPP is $t_{mpp} = 0.4$ mm, $d = 1$ mm and $b = 6.3555$ mm. The experimental results at five frequencies $f = 500$ Hz (\circ), 700 Hz (\times), 800 Hz (\square), 900 Hz (Δ) and 1100 Hz ($+$) are shown. Figures 2.1(a) and 2.1(b) illustrate that both acoustic absorption and acoustic resistance increase with the incidence sound pressure level $SPL_{incident}$, which agrees with the observation given by Ingard and Ising (1967). Moreover, Figure 2.1(c) shows that the acoustic reactance of the MPP decreases when the incidence sound pressure increases. The obvious change of absorption coefficient, acoustic resistance and reactance is observed at SPL around 95 dB. By comparing with the results measured at the lowest $SPL_{incident}$, the variations of the acoustic absorption, resistance and reactance in percentage are shown in Figure 2.2. More than 10 % of increments of both absorption, acoustic resistance and reactance are observed at $SPL_{incident} \geq 100$ dB. The experimental results imply that the linear acoustic impedance expressed as Eq. (2.2) is no longer valid at $SPL_{incident}$ larger than 100 dB due to the significant nonlinearity effect of the orifice.

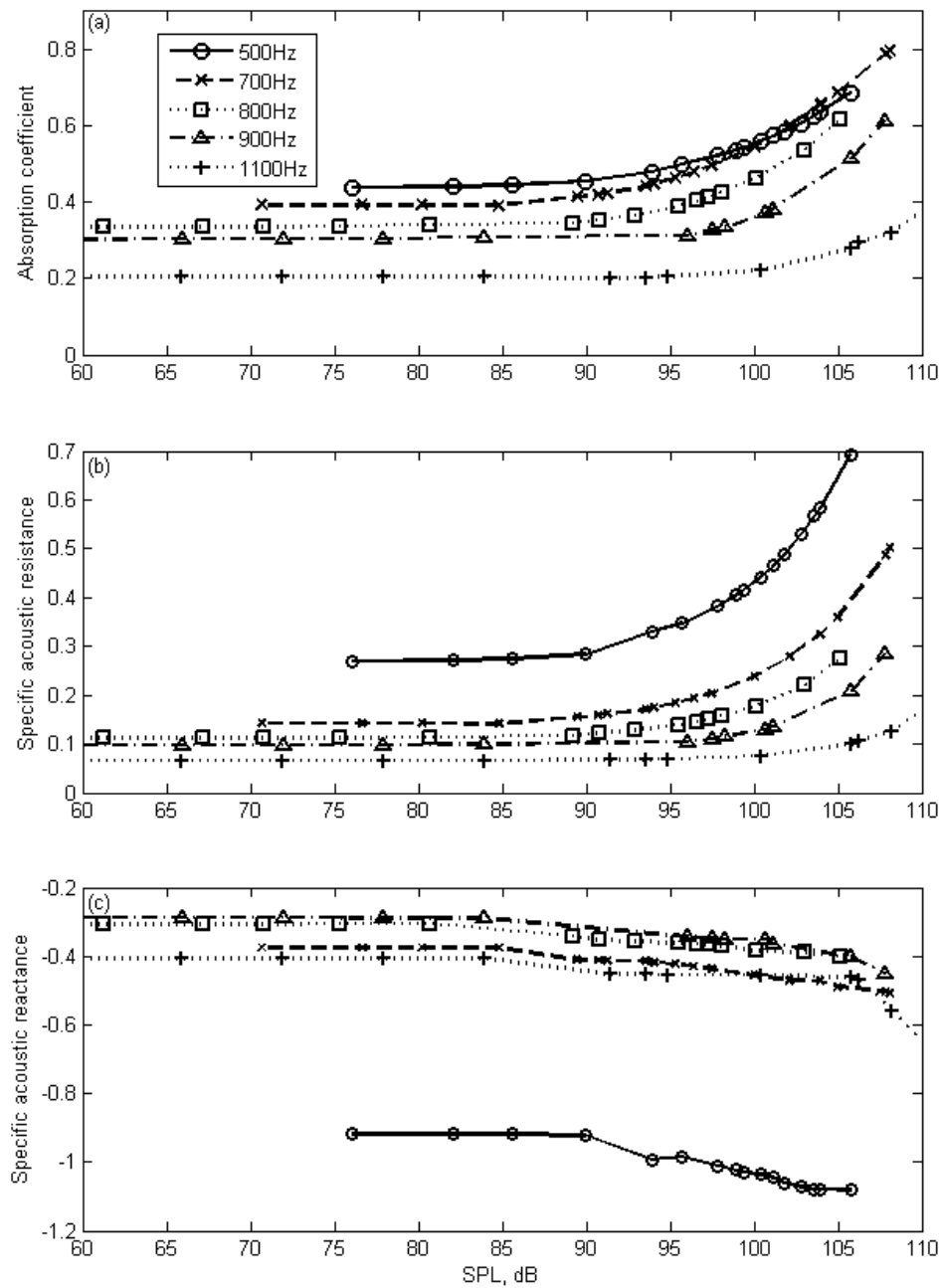


Figure 2.1 Acoustic properties of MPP absorber at different incidence sound pressure level. (a) Acoustic absorption; (b) Acoustic resistance; (c) Acoustic reactance.

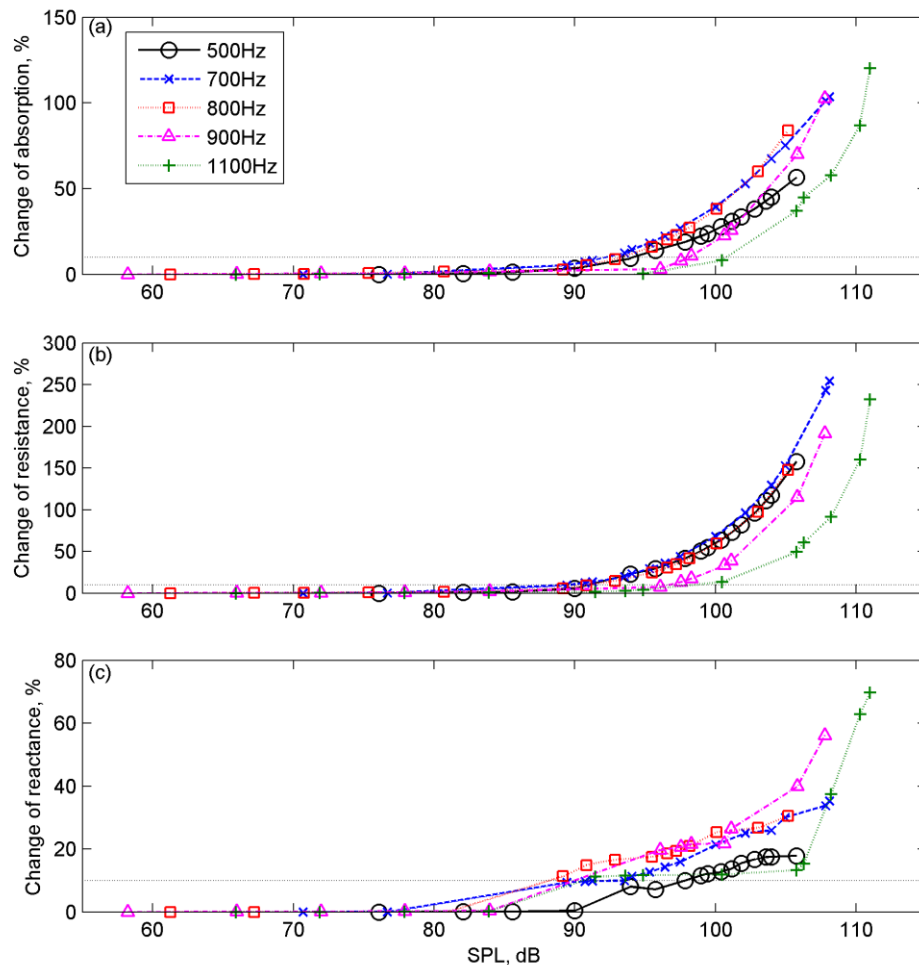


Figure 2.2 Variations of the acoustic properties of MPP absorber at different incidence sound pressure level in percentage. (a) Acoustic absorption; (b) Acoustic resistance; (c) Acoustic reactance.

Numerous studies were conducted to investigate the acoustic behaviors of the orifice in the situation of high amplitude excitation. When sound wave at high amplitude transmits through the orifice, there is flow separation and vortex shedding at the sharp edge of the orifice. The process of the vortex formation takes the acoustic energy, and hence improve the absorption performance of MPP. Park (2013) introduced an empirical impedance model which included all geometric parameters of MPP and also the incidence pressure. The specific nonlinear impedance is expressed as

$$Z_{NL} = Z_{resist,NL} + Z_{react,NL} , \quad (2.3)$$

where $Z_{resist,NL}$ and $Z_{react,NL}$ are the nonlinear specific acoustic resistance and reactance respectively, which are written as

$$Z_{resist,NL} = \frac{32\nu t_{mpp}}{\sigma \rho_0 c_0 d^2} \left[\left(1 + \frac{K^2}{32} \right)^{1/2} + \frac{\sqrt{2}}{8} K \frac{d}{t_{mpp}} \right] + 1.59 \left(\frac{d}{t_{mpp}} \right)^{0.06} \sigma^{-0.845} \left[\sigma \left(\sqrt{0.25 + \frac{2p_{in}}{\rho_0 c_0^2 \sigma^2}} - 0.5 \right) \right], \quad (2.4)$$

$$Z_{react,NL} = \frac{i\omega t_{mpp}}{\sigma c_0} \left[1 + \left(9 + \frac{K^2}{2} \right)^{-1/2} + 0.85 \frac{d}{t_{mpp}} \left(1 + \frac{1}{1-\sigma^2} \times \left(\sqrt{0.25 + \frac{2p_{in}}{\rho_0 c_0^2} \times \frac{1-\sigma^2}{\sigma^2}} - 0.5 \right) \right)^{-1} \right]$$

where p_{in} is the amplitude of incidence sound wave.

2.2. Theoretical Modeling of Parallel-arranged MPP Absorber

Figure 2.3 shows the two-dimensional configuration of three basic modules of MPP absorbers. The schematic diagram of a single MPP absorber with one backing cavity with depth D_s is shown as Figure 2.3(a). The MPP absorbers with the backing cavity partitioned into two and three sub-cavities with different cavity depths are named as dual MPP absorber array and triple MPP absorber array and shown in Figures 2.3(b) and 2.3(c) respectively. Homogeneous MPP is considered in the present study.

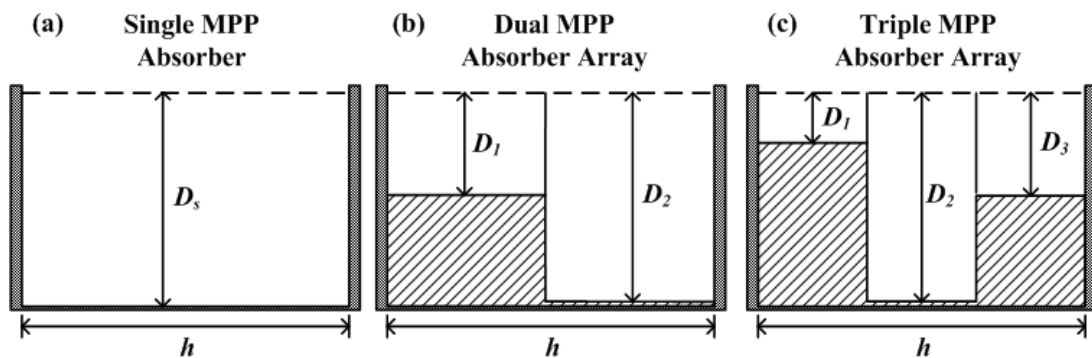


Figure 2.3 Schematic diagram of the MPP absorbers. (a) Single MPP absorber; (b) Dual MPP absorber array; (c) Triple MPP absorber array.

For the single MPP absorber, the normal absorption coefficient can be predicted by (Maa, 1998)

$$\alpha = \frac{4 \operatorname{Re}(Z)}{[1 + \operatorname{Re}(Z)]^2 + [\operatorname{Im}(Z) - \cot(k_0 D_s)]^2}, \quad (2.5)$$

where $k_0 = \omega/c_0$ is the wavenumber and Z is the specific acoustic impedance which can be expressed as Eqs. (2.1) or (2.3) for the linear and nonlinear regime respectively.

For the micro-perforated panel absorber array, the acoustic impedance between each MPP absorber component is different. In this case, the acoustic impedance and the sound absorption coefficient of the MPP absorber array can be predicted by using the electro-acoustic circuit model (Yairi and Sakagami, 2011). For the multiple MPP absorber array consisting of N MPP absorber components, the total acoustic impedance can be formulated as

$$Z_{total} = \left[\sum_{j=1}^N \frac{1}{N} \times \frac{1}{Z_j} \right]^{-1}, \quad (2.6)$$

where Z_j is the specific acoustic impedance of the j -th MPP absorber component. Z_j equals to $Z_L - i \cot(k_0 D_j)$ or $Z_{NL} - i \cot(k_0 D_j)$ in the linear regime and nonlinear regime respectively, where i is $\sqrt{-1}$, $j = 1, \dots, N$. The corresponding sound absorption coefficient of multiple absorber array can be expressed as

$$\alpha_{array} = 1 - \left| \frac{Z_{total} - 1}{Z_{total} + 1} \right|^2. \quad (2.7)$$

2.3. Finite Element Modeling of Parallel-arranged MPP Absorber

A finite element model of the parallel-arranged MPP absorber array is developed based on the configuration shown in Figure 2.4 in order to simulate the acoustic behaviors of the MPP absorber array at high sound intensity. The normal incident sound wave p_i is assumed as a plane wave. When the acoustic wave is incident on the MPP, part of the sound energy is dissipated by the MPP, while the rest is reflected. The reflected sound wave is represent by p_r . The duct walls, cavity walls and the partitions are regarded as acoustically rigid.

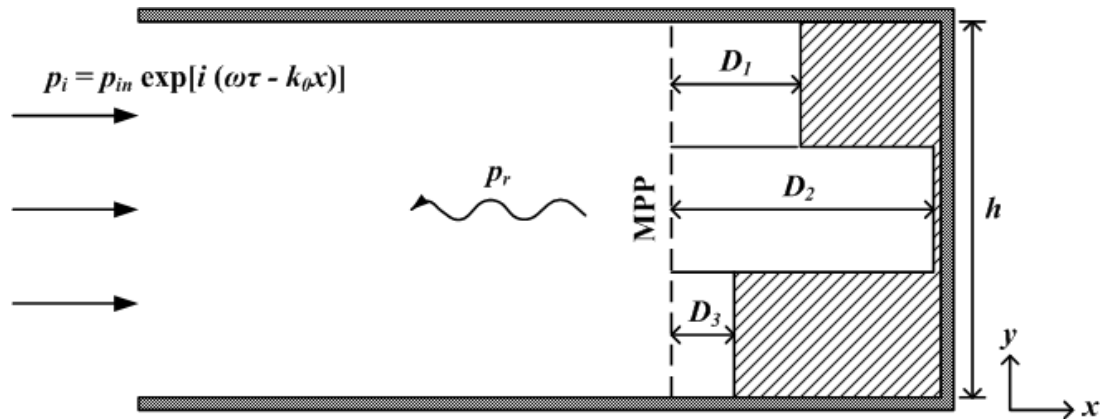


Figure 2.4 Schematic diagram of the parallel-arranged MPP absorber array with three partitioned sub-cavities.

The acoustic field inside the duct and backing sub-cavities are modeled as two acoustic domains. At the acoustic excitation below 130 dB, the acoustic Mach number M is low, i.e., $M \ll 1$, the acoustic field can be regarded as linear acoustics. Therefore, the Helmholtz equation is used as the governing equation for the acoustic domains of duct and backing sub-cavities, which is expressed as

$$(\nabla^2 + k_0^2)\phi = 0, \quad (2.8)$$

where ϕ is the velocity potential. The acoustic pressure p and the particle velocity u can be expressed by the velocity potential,

$$p = -i\omega\rho_0\phi, \quad u = \nabla\phi, \quad (2.9)$$

At the inlet of the duct, the Dirichlet-to-Neumann (DtN) boundary condition is applied to describe the no-reflection condition. The plane sound wave is incident on the MPP from the left hand side of the duct,

$$p_i = p_{in} \exp[i(\omega\tau - k_0x)], \quad (2.10)$$

where p_{in} is the amplitude of incident sound wave and τ is time. For the acoustically rigid duct walls and partitions, the particle velocity vanishes in the normal direction of the wall \mathbf{n} , and hence the boundary condition can be expressed as

$$\mathbf{n} \cdot \nabla\phi = 0. \quad (2.11)$$

The MPP is modeled in a structural domain. By neglecting the vibration of the panel, the boundary condition at the interface of the rigid MPP is formulated as the normal velocity over the orifice

$$\left. \frac{\partial\phi}{\partial x} \right|_{rigid} = \frac{P_{cav} - P_{duct}}{\rho_0 c_0 Z} \quad (2.12)$$

where p_{duct} and p_{cav} represent the acoustic pressure on the duct side and the backing cavity side respectively, and Z is the specific acoustic impedance. In the linear regime, the specific acoustic impedance Z is formulated as Eq. (2.1). For the case at moderate acoustic excitation, the acoustic nonlinearity of the orifice is considered, and hence the acoustic impedance is expressed as Eq. (2.3).

When the acoustic excitation is high and a light panel is used, the effects of the structural vibration of the perforated panel on the acoustic performance can be significant at the resonance frequency of the MPP. In this case, the vibration of the MPP should be taken into consideration and the MPP is treated as a flexible panel. The motion of the MPP is driven by the pressure difference at the panel interface,

$$B\nabla^4\eta(y,\tau)-\omega^2M_s\eta(y,\tau)=p_{duct}-p_{cav}, \quad 0 < y < h, \quad (2.13)$$

where η denotes the normal displacement of panel, h is the total height of MPP absorber, B is the bending stiffness of the plate and M_s is the MPP surface density. The ends of the MPP can be either fixed or pinned. The boundary conditions for fixed and pinned ends are

$$\begin{cases} \eta = 0, \quad \frac{\partial\eta}{\partial y} = 0, & \text{fixed ending,} \\ \eta = 0, \quad \frac{\partial^2\eta}{\partial y^2} = 0, & \text{pinned ending.} \end{cases} \quad (2.14)$$

When the perforated panel vibrates, the averaged velocity field over the orifice combines the normal vibration velocity of the panel $u_p' = i\omega\eta$ and the air particle velocity inside the orifice. Thus, the boundary condition at the interface of MPP expressed in Eq. (2.12) becomes

$$\left. \frac{\partial\phi}{\partial x} \right|_{flexible} = \left(1 - \frac{\sigma \times \text{Im}(Z)}{Z} \right) \times u_p' + \frac{p_{cav} - p_{duct}}{\rho_0 c_0 Z}, \quad (2.15)$$

where Im is the imaginary part of complex acoustic impedance.

The governing equations for the acoustic domains and structural domain, Eqs. (2.8) and (2.13), with the relevant boundary conditions are solved by using COMSOL

Multiphysics. The normal incidence absorption coefficient of the MPP absorber array is formulated as

$$\alpha = \frac{\rho_0 c_0 \int_0^h \text{Re}[p^*(y) \times u(y)] dy}{|p_{in}|^2 h}, \quad (2.16)$$

where the asterisk represents the complex conjugate and Re is the real part of complex number.

2.4. Numerical Results and Discussion

Following the acoustic impedance model stated in Sec. 2.2, the normal absorption coefficients of the MPP absorber with simple configuration can be calculated. The parameters of the MPPs used in the numerical investigations are listed as *Table 2.1* in details. The structural vibration of the MPP is excluded in Sec. 2.4.1 and 2.4.2. The effect of the panel vibration is taken into account in Sec. 2.4.3 and 2.4.4. In the present study, the numerical model is discretized as the triangular quadratic-Lagrange elements. For the model without vibration, the maximum element size is 0.005m and the mesh consists of 3065 elements totally. The element size to wavelength ratio for the cut-on frequency $f^* = 1700$ Hz is 0.025. For the model with structural vibration, the maximum element size is 0.003m, and the mesh consists of 6044 elements and 33 elements for the acoustic and structural domains respectively.

	Thickness (t_{mpp})	Orifice diameter (d)	Perforation ratio (σ)
MPP A	0.5 mm	0.5 mm	1%
MPP B	1 mm	1 mm	5.5%

MPP C	1 mm	1 mm	3.3%
MPP D	1 mm	0.6 mm	5.5%
MPP E	0.5 mm	1 mm	5.5%
MPP F	0.7 mm	1.2 mm	2.8%
MPP G	1 mm	1 mm	1.5%

Table 2.1 Parameters of MPPs used in the numerical investigations.

The comparisons of the predicted normal absorption coefficient of a single MPP absorber with the configuration shown as Figure 2.3(a) by the finite element model and the analytical solutions for linear and nonlinear regimes at incidence sound pressure level $SPL_{\text{incident}} = 100$ dB and 120 dB are shown in Figures 2.5(a), 2.5(b) and 2.5(c) respectively. MPP A is used and it is regarded as a rigid panel. The depth of the single backing cavity is $D_s = 100$ mm. For both linear and nonlinear regimes, the numerical results predicted by the finite element model and the analytical solutions are in good agreement. In order to verify the results calculated by the finite element model with a more complicated configuration backed by multiple sub-cavities, experimental studies are conducted and compared with the finite element simulations in Sec. 2.5.

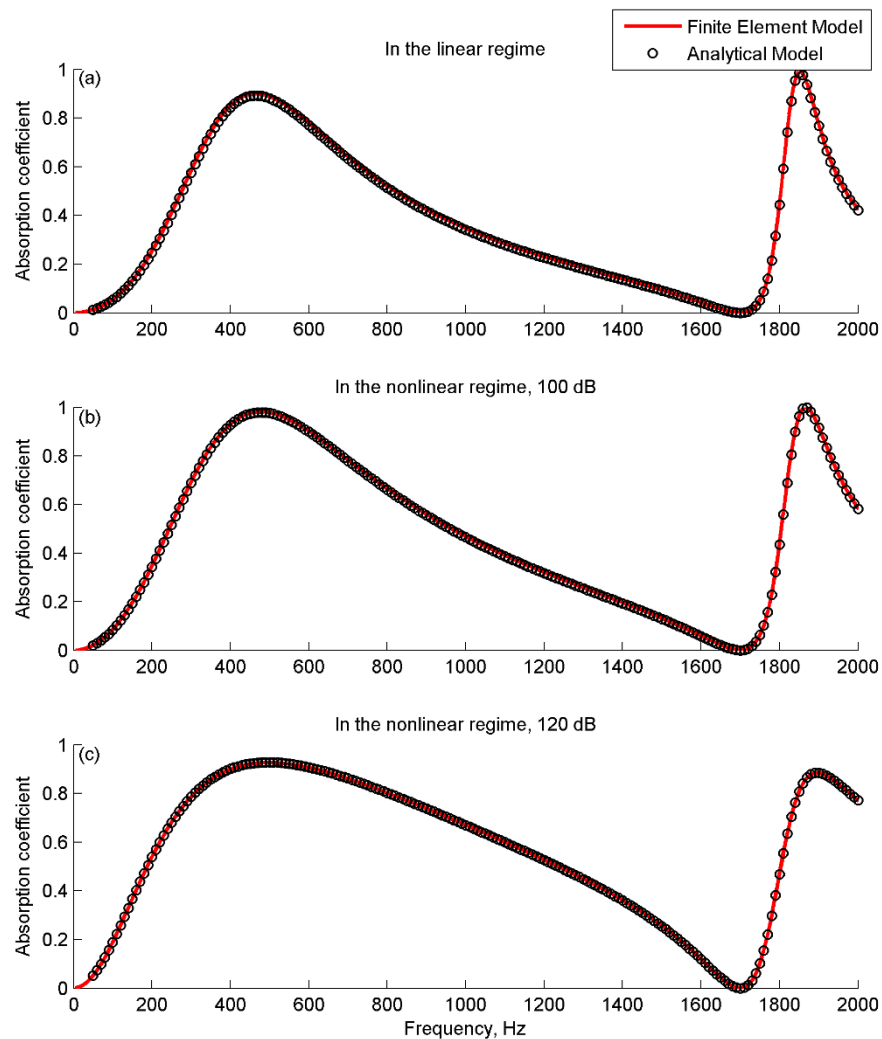


Figure 2.5 Comparison of the predicted normal incidence absorption coefficients of the single MPP absorber by the finite element model and the analytical solutions. (a) Linear; (b) Nonlinear at $\text{SPL}_{\text{incident}} = 100\text{dB}$; (c) Nonlinear at $\text{SPL}_{\text{incident}} = 120\text{dB}$. The properties of the MPP A are $d = t_{\text{mpp}} = 0.5\text{mm}$ and $\sigma = 1\%$. The cavity depth is $D_s = 100\text{mm}$.

2.4.1. Parametric Study of MPP Absorber Array

Figure 2.6 shows the absorption performance of triple MPP absorber array with different perforation ratios. It also compares the absorption coefficients of the triple MPP absorber array (solid line) with the single MPP absorber with cavity depths $D_s = 100\text{mm}$, 50mm and 25mm which are denoted by the dash-dot, dashed and dotted

lines respectively. The incident sound pressure level is 110dB. The default depths of sub-cavities for the triple MPP absorber array are $D_1 = 50$ mm, $D_2 = 100$ mm and $D_3 = 25$ mm. Figure 2.6(a) shows the sound absorption curves for MPP B. The poor absorption performances are observed for the single MPP absorbers, where the absorption coefficients are less than 0.5, due to the insufficient acoustic resistance provided by the large orifices with diameter $d = 1$ mm. In contrast, for the MPP absorber array, the overall sound absorption coefficients are relatively higher than those of single MPP absorbers. Based on the parallel absorption mechanism, three spectral peaks with $\alpha_{1,2,3} = 0.92, 0.91$ and 0.67 induced by the local resonance effects of sub-cavities are identified. Also, the half-absorption bandwidth, i.e., half-absorption bandwidth $= f_U/f_L$ where f_U is the upper frequency limit and f_L is the lower frequency limit where the absorption coefficient is 0.5, is improved to 2.96. In this regard, the MPP absorber array can provide better absorption performance with lower requirement of acoustic resistance. The absorption coefficients of the MPP absorber array at three spectral peaks can be further improved by reducing the number of orifices as shown in Figure 2.6(b), which illustrates the performance of MPP C with $\sigma = 3.3\%$. Referring to Eq. (2.4), such increment of absorption is attributed to the increase of acoustic resistance. Moreover, with the decrease of perforation ratio, the frequency range for half-absorption is shifted to lower frequencies due to the increase of acoustic reactance. Although the upper limit frequency f_U reduces from 1565 Hz to 1465 Hz as shown in Figure 2.7(a), the lower limit frequency f_L decreases from 530 Hz to 430 Hz. Hence, the enhanced absorption performance of the MPP absorber array for a lower frequency range can be achieved by the MPP absorber array with smaller perforation ratio. The effect of the orifice diameter on the absorption performance of

MPP absorber array is shown in Figure 2.8. The numerical result of MPP B is compared with MPP D, which has a smaller diameter $d = 0.6$ mm, at 110 dB. Figure 2.8 shows that a high absorption coefficient can be achieved with a smaller diameter of orifice d since the smaller orifice can provide a higher surface acoustic resistance. Therefore, the absorption performance is improved for the whole frequency range, and hence, the half-absorption bandwidth increases from 2.96 to 3.5 as shown in Figure 2.9(c). Figure 2.10 illustrates the effect of panel thickness on the absorption coefficient of the MPP absorber array. The performance of a thinner MPP, i.e., MPP E of $t_{mpp} = 0.5$ mm, is predicted and compared with that of MPP B. With the decrease of the panel thickness, the lower and upper frequency limits for half-absorption shift to higher frequency. Figure 2.11 shows that the lower and upper frequency limits of the MPP absorber array for MPP E are 580 Hz and 1640 Hz respectively. Moreover, the half-absorption bandwidth reduces with the panel thickness. The parametric study on the absorption performance of the parallel-arranged MPP absorber array gives the basic information in designing the MPP absorber.

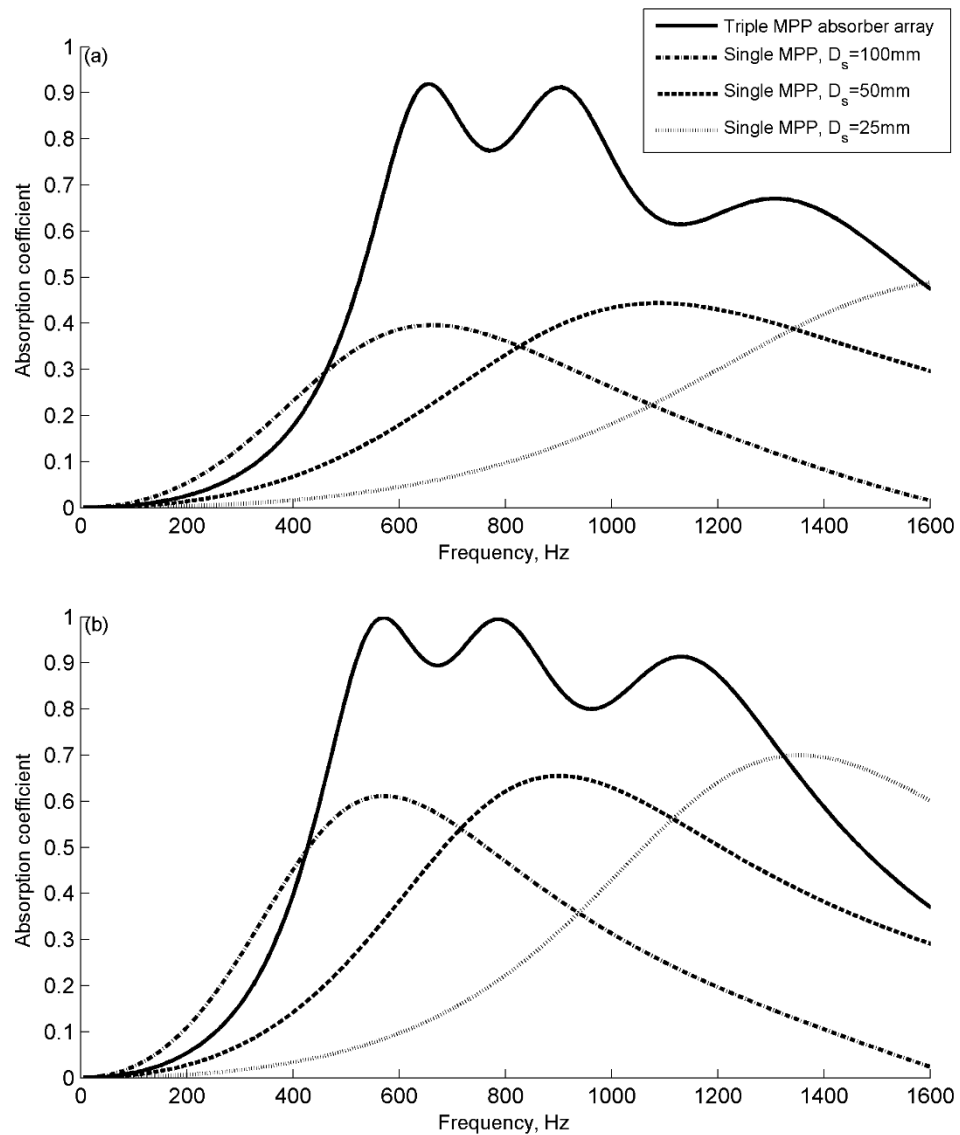


Figure 2.6 Effect of perforation ratio on the normal incidence absorption coefficients of MPP absorber array at the nonlinear regime, $SPL_{\text{incident}} = 110$ dB. (a) MPP B with $\sigma = 5.5\%$; (b) MPP C with $\sigma = 3.3\%$. (—) MPP absorber array; (···) Single MPP absorber with $D_s = 100\text{mm}$; (---) Single MPP absorber with $D_s = 50\text{mm}$; (-.-) Single MPP absorber with $D_s = 25\text{mm}$.

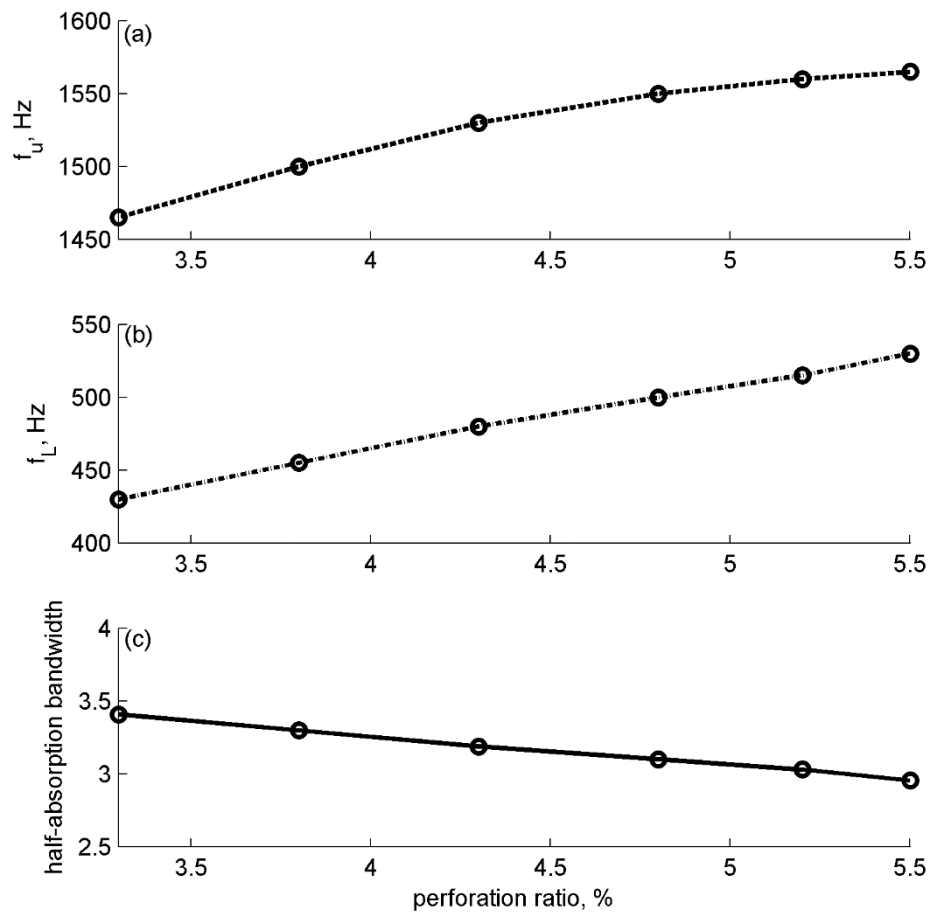


Figure 2.7 Frequency range for half-absorption. (a) Upper frequency limits; (b) Lower frequency limits; (c) Half-absorption bandwidth.

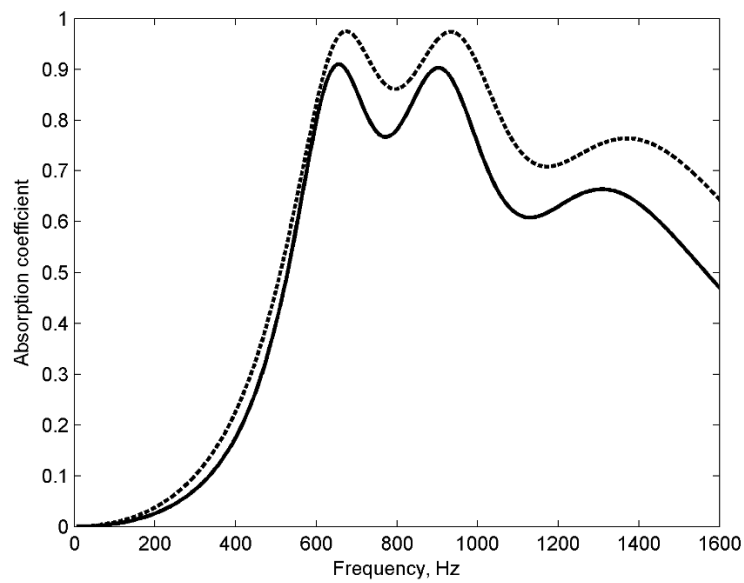


Figure 2.8 Effect of orifice diameter on the normal incidence absorption coefficients of MPP absorber array at the nonlinear regime, $SPL_{\text{incident}} = 110$ dB. (—)MPP B with $d = 1$ mm; (---) MPP D with $d = 0.6$ mm.

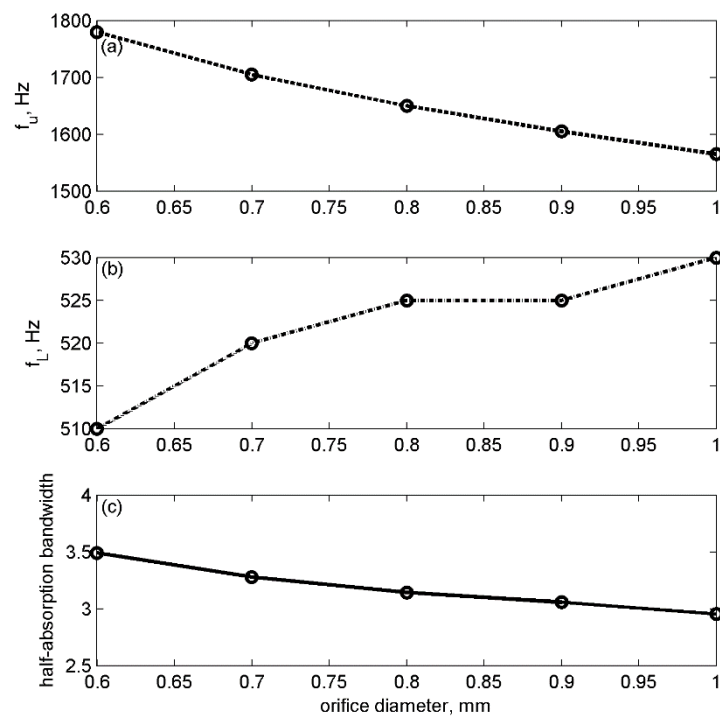


Figure 2.9 Frequency range for half-absorption. (a) Upper frequency limits; (b) Lower frequency limits; (c) Half-absorption bandwidth.

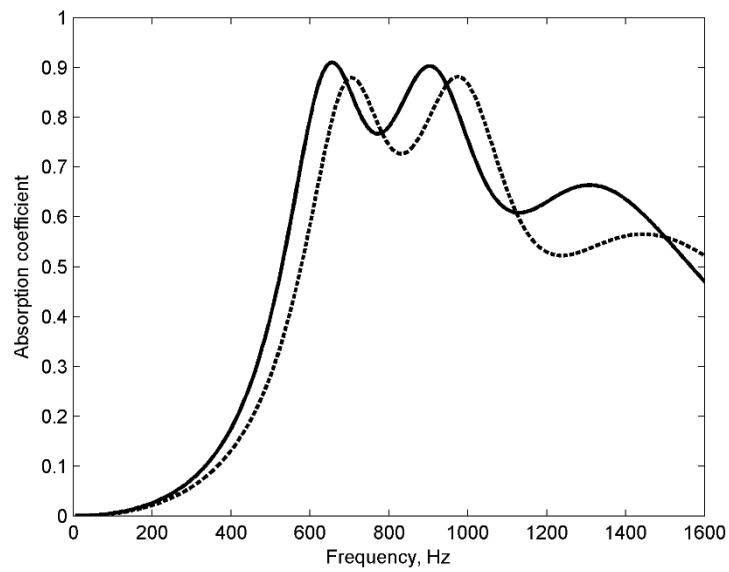


Figure 2.10 Effect of panel thickness on the normal incidence absorption coefficients of MPP absorber array at the nonlinear regime, $SPL_{\text{incident}} = 110$ dB.
 (—)MPP B with $t_{mpp} = 1$ mm; (---) MPP E with $t_{mpp} = 0.5$ mm.

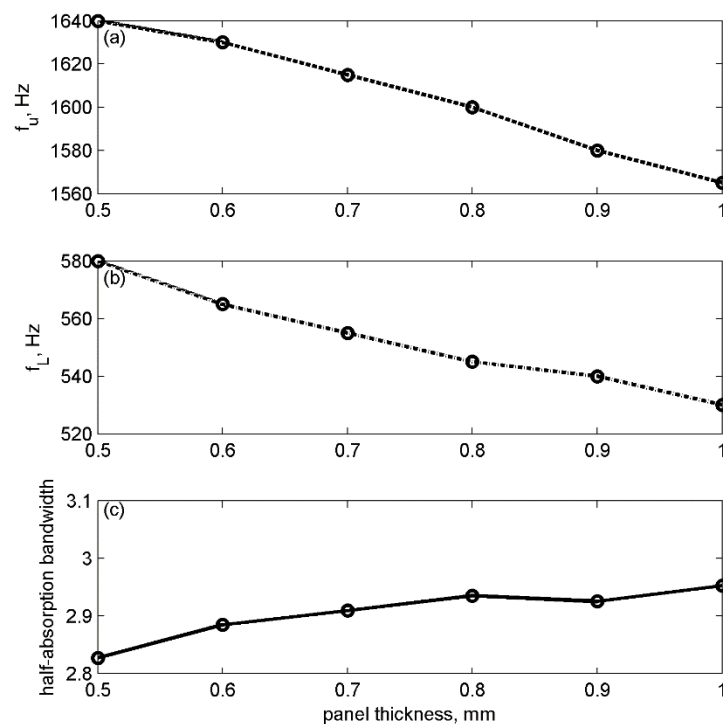


Figure 2.11 Frequency range for half-absorption. (a) Upper frequency limits; (b) Lower frequency limits; (c) Half-absorption bandwidth.

2.4.2. Effects of Incidence Pressure Amplitude

The comparison of the normal incidence absorption coefficient of the MPP absorbers for MPP F between the linear and nonlinear regimes is illustrated in Figure 2.12. The numerical result for the linear case is plotted in solid line. The predicted absorption coefficients of the MPP absorber array at high sound excitation $SPL_{\text{incident}} = 100$ dB, 110 dB and 120 dB are represented by the dashed, dotted, dash-dot lines respectively. Figure 2.12(a) demonstrates the effect of the incidence pressure amplitude on the acoustic absorption of the single MPP absorber. It is found that the absorption coefficient and the half-absorption bandwidth increase with the incidence sound pressure level. The peak absorption coefficient can reach to 0.87 for MPP F at $SPL_{\text{incident}} = 120$ dB, which is 2.35 times higher than that of the linear case. The similar observation can be obtained for the triple MPP absorber array as shown in Figure 2.12(b). In the linear regime, based on the parallel absorption mechanism, three spectral peaks are found at $f_{1,2,3}^* = 555$ Hz, 760 Hz and 1090 Hz which are associated with the local resonances of the three sub-cavities $D_2 = 100$ mm, $D_1 = 50$ mm and $D_3 = 25$ mm respectively. The corresponding normal absorption coefficients at three peaks are $\alpha_{1,2,3} = 0.87, 0.87$ and 0.75 respectively. When the MPP absorber array having the same parameters is subject to moderate acoustic intensity, the whole absorption curve is improved to a higher level and also a broader half-absorption bandwidth is achieved when compared with the linear result. The corresponding absorption coefficients at $f_{1,2,3}^*$ are improved to $\alpha_{1,2,3} = 0.99, 0.99$ and 0.92 in the nonlinear regime at 110 dB. When the incidence pressure level further increases to $SPL_{\text{incident}} = 120$ dB, the first spectral peak at 580 Hz is reduced to $\alpha_1 = 0.95$. The smoothed absorption performance of the MPP absorber array at moderate intensity

sound is induced by the added-mass effect from the neighboring sub-cavity. The explanation would be described in detail with Figures 2.14 and 2.15.

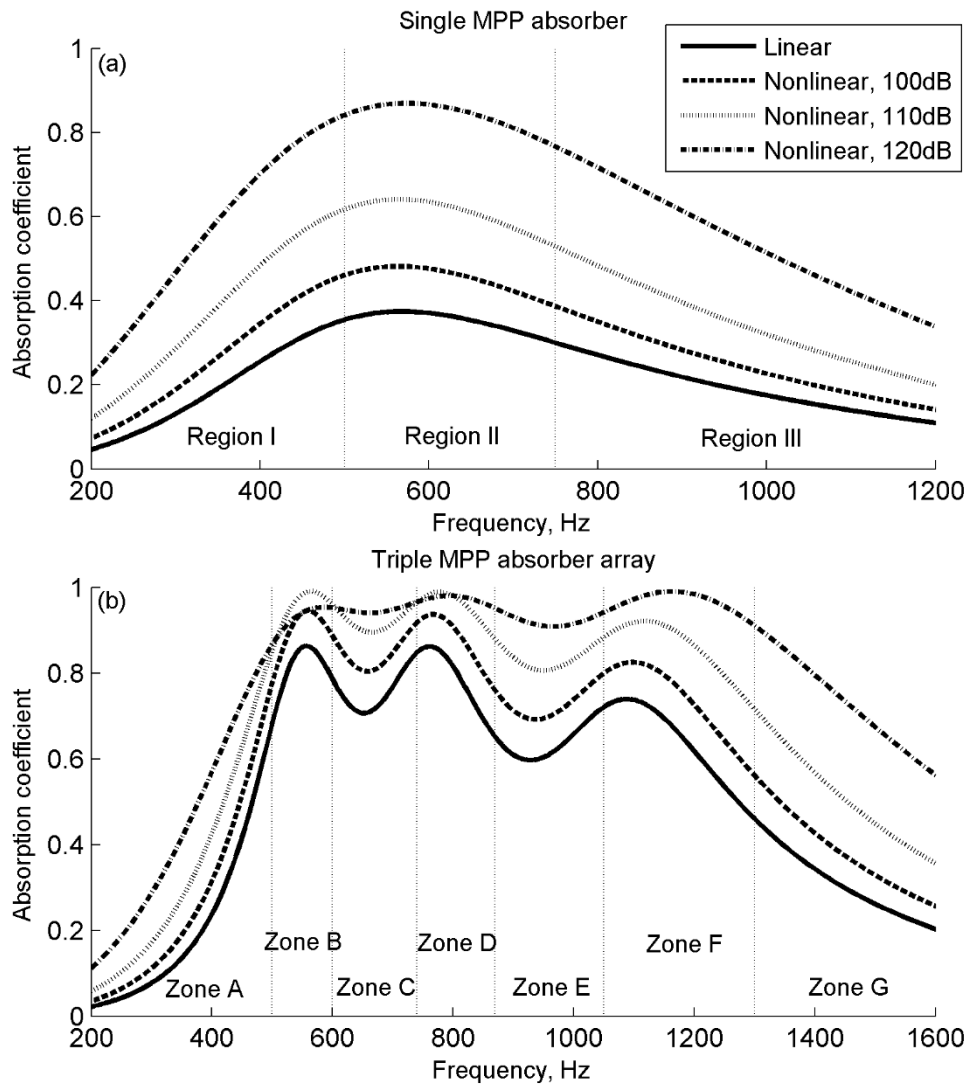


Figure 2.12 Comparison of the normal incidence absorption coefficients of MPP F between the linear and nonlinear regimes. (a) Single MPP absorber; (b) Triple MPP absorber array.

The absorption mechanism for the simple configuration with single backing cavity can be explained by dividing the acoustic response into three regions: *region I* is at low frequency range with stiffness effect; *region II* is the resonating part; *region III* is

at high frequency range with mass effect. In *region I*, it is the zone of acoustic reactance mismatch since the stiffness effect of the backing cavity is dominant as shown in Figure 2.13(b) and hence the resultant reactance of the MPP absorber is negative. For both linear and nonlinear cases, the absorption coefficient is unable to reach a high value due to the reactance mismatch. However, comparing the results between the linear regime and that at $SPL_{\text{incident}} = 120$ dB, the absorption performance of the single MPP absorber is comparatively better at high sound pressure level. In the nonlinear regime, the vortex ring formed at the exit of the perforations, which induces a higher acoustic resistance on the MPP as shown in Figure 2.13(a), and hence improve the absorption performance of the MPP absorber. For *region II*, the stiffness effect of the backing cavity is balanced by the virtual mass effect of the MPP. In this frequency range, the MPP absorber performs the best when compared with the absorption performance in *region I* and *region III* since the MPP absorber is resonating and hence more acoustic energy can be dissipated in this frequency range. The absorption performance of MPP absorber is also better under moderate acoustic excitation since the acoustic resistance of the MPP at $SPL_{\text{incident}} = 120$ dB is 0.415, which is 6.48 times higher than that in the linear regime at 570 Hz with maximum absorption coefficient. At higher frequency, it is regarded as *region III* where the virtual mass effect of the MPP is dominant. The relatively higher absorption coefficient is also achieved for the nonlinear case due to the acoustic resistance being higher which brings benefit to sound dissipation. Therefore, the absorption performance of the single MPP absorber is improved at moderate intensity sound due to the larger acoustic resistance for both regions.

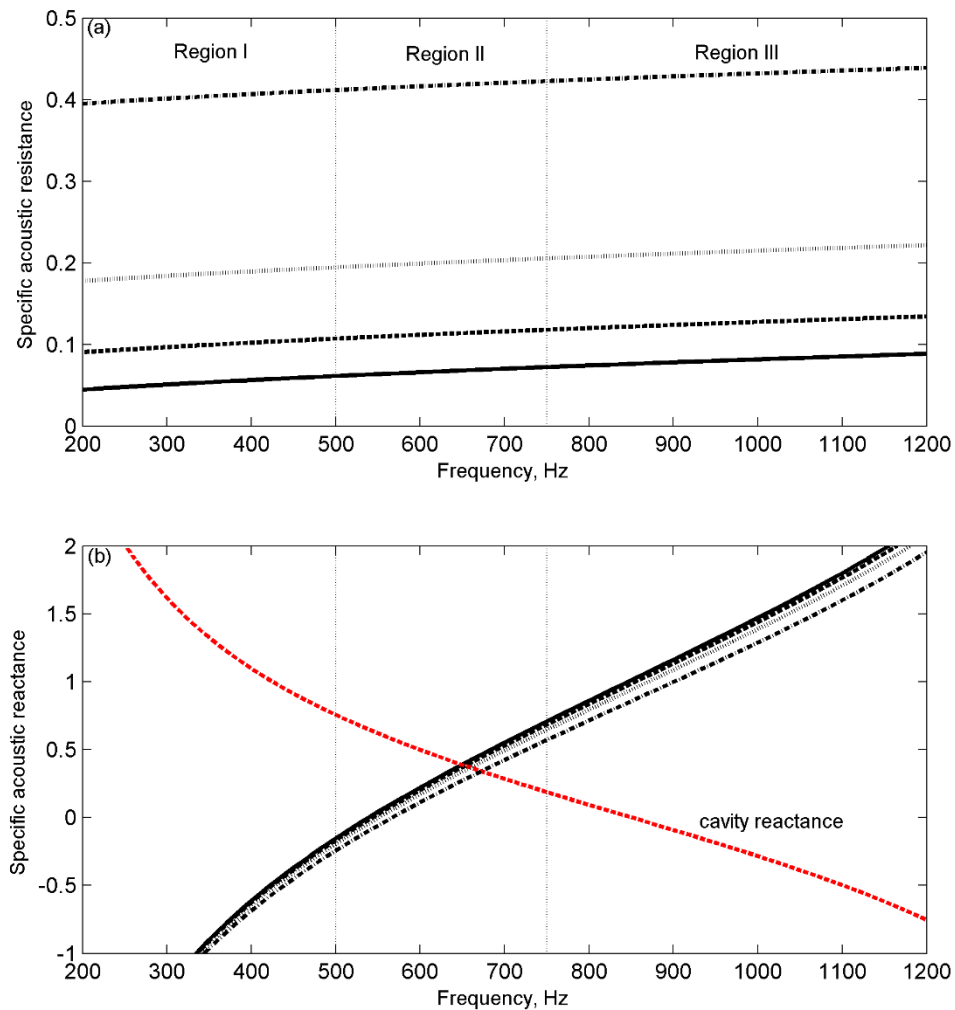


Figure 2.13 Acoustic impedance of the single MPP absorber for MPP F. (a) Specific acoustic resistance; (b) Specific acoustic reactance. (—) Linear; (---) $SPL_{\text{incident}} = 100$ dB; (···) $SPL_{\text{incident}} = 110$ dB; (-·-) $SPL_{\text{incident}} = 120$ dB.

The absorption mechanism of the parallel-arranged MPP absorber array is more complicated than that of the single MPP absorber. The acoustic behavior of the triple MPP absorber array can be divided into seven zones: *zone A* is at low frequency range with stiffness effect; *zones B, D* and *F* are the first, second and third resonating frequency ranges; *zones C* and *E* are the transition stages; *zone G* is at high frequency

range with mass effect. As shown in Figure 2.12(b), firstly, it is observed that the absorption performance of the MPP absorber array is better than that in the linear regime. Secondly, the insufficient sound absorption at the trough point at $f^* = 650$ Hz and 930 Hz for the linear case is improved with the increase of acoustic excitation. The first observation can be explained by the idea stated for the single MPP absorber since the acoustic responses of the MPP absorber array in *zone A* and *G* are the same as that of *region I* and *III* of the single MPP absorber respectively. Three spectral peaks are found at $f_{1,2,3}^* = 555$ Hz, 760 Hz and 1090 Hz due to the local resonance occurring in *zones B, D* and *F* respectively. For the second observation, the improvement of the absorption coefficient at troughs with the incidence pressure level can be explained by the total acoustic impedance of the MPP absorber array obtained by the theoretical model established in Sec. 2.2 in the transition stages, i.e., *zones C* and *E*. At frequency around 630 Hz, the acoustic reactance of the MPP absorber array in the linear regime is high due to the virtual mass effect of the MPP absorber component with $D_2 = 100$ mm. The ability of the MPP absorber array to dissipate sound energy is degraded due to the reactance mismatch as shown in Figure 2.14(b). However, at moderate acoustic excitation, a negative mass effect is induced since part of the attached mass in the orifice is blown away by the jet. Therefore, the acoustic reactance of the MPP is reduced, which allows sound wave to penetrate for sound absorption. On the other hand, at frequency around 700 Hz, an increasing acoustic reactance can be found with the increase of incidence pressure. *Zone C* is the transition stage that the resonating component is changed from $D_2 = 100$ mm to $D_1 = 50$ mm. The acoustic energy would be dissipated in both cavity 1 and 2. With the increase of sound pressure level, the situation of reactance mismatch of MPP absorber component

with $D_2 = 100$ mm is improved and thus more acoustic energy would propagate to cavity 2 when compared with the linear case. The contribution of the neighboring cavity provides an added mass effect to the overall reactance of the MPP absorber array in the nonlinear regime. As a result, the absorption performance at the trough is improved at high sound intensity since the effect of the reactance mismatch is reduced due to the added-mass effect given by the neighboring sub-cavity. The similar observation around 1000 Hz can be obtained for the second trough at *zone E*.

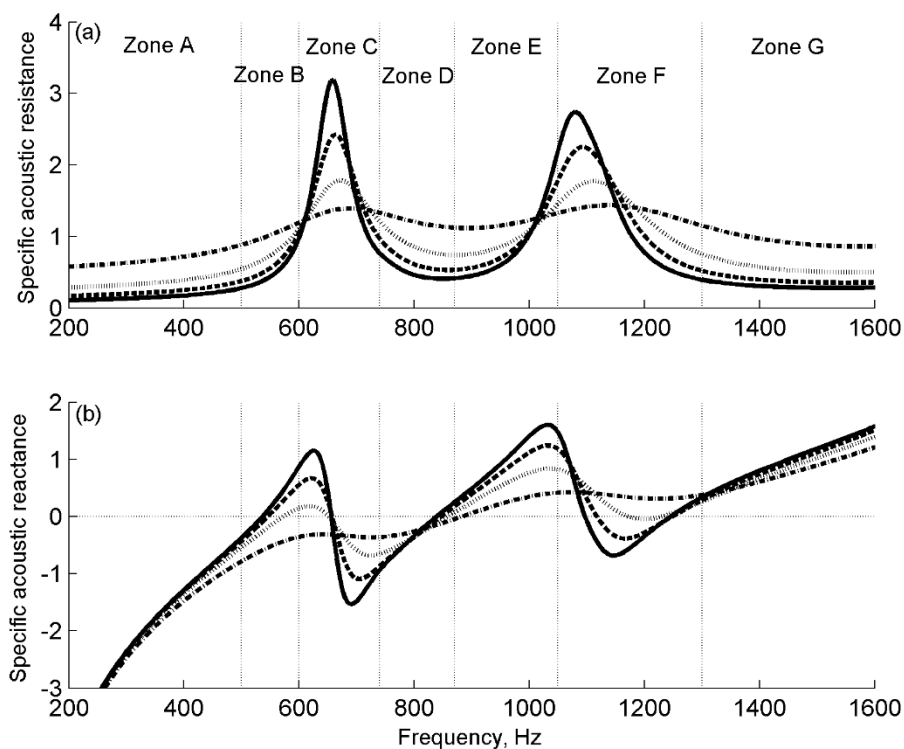


Figure 2.14 Acoustic impedance of the parallel-arranged MPP absorber array for MPP F. (a) Specific acoustic resistance; (b) Specific acoustic reactance. (—) Linear; (---) $SPL_{\text{incident}} = 100$ dB; (-·-) $SPL_{\text{incident}} = 110$ dB; (-·-) $SPL_{\text{incident}} = 120$ dB.

The troughs appear on the absorption curve for the MPP absorber array can be eliminated at its critical incidence sound pressure level as illustrated in Figure 2.15(a).

The numerical result is predicted for MPP G in the linear (solid line) and nonlinear (dashed line) regimes. At $SPL_{incident} = 120$ dB, the absorption curve is smoothed out without significant trough, and the absorption performance of the MPP absorber array is maintained at $\alpha > 0.8$ from $f^* = 415$ Hz to 1090 Hz. The pattern of the acoustic resistance and reactance of the MPP absorber array is similar to that of the single MPP absorber as shown in Figures 2.15(b) and 2.15(c) respectively. The negative mass effect induced by the jet formation at the orifice of the neighboring sub-cavity reduces the drawback brought by the effect of reactance mismatch. It allows more acoustic energy to propagate towards the neighboring sub-cavity. The contribution of the neighboring sub-cavity provides an added-mass effect to the MPP absorber array at two transition stages in *zone C* and *E*, and hence a smoother effective acoustic reactance can be achieved. Therefore, the performance of the MPP absorber array at the critical incidence sound pressure level behaves like the single MPP absorber but with a higher acoustic resistance and flat acoustic reactance because of the increased contribution from the neighboring sub-cavity.

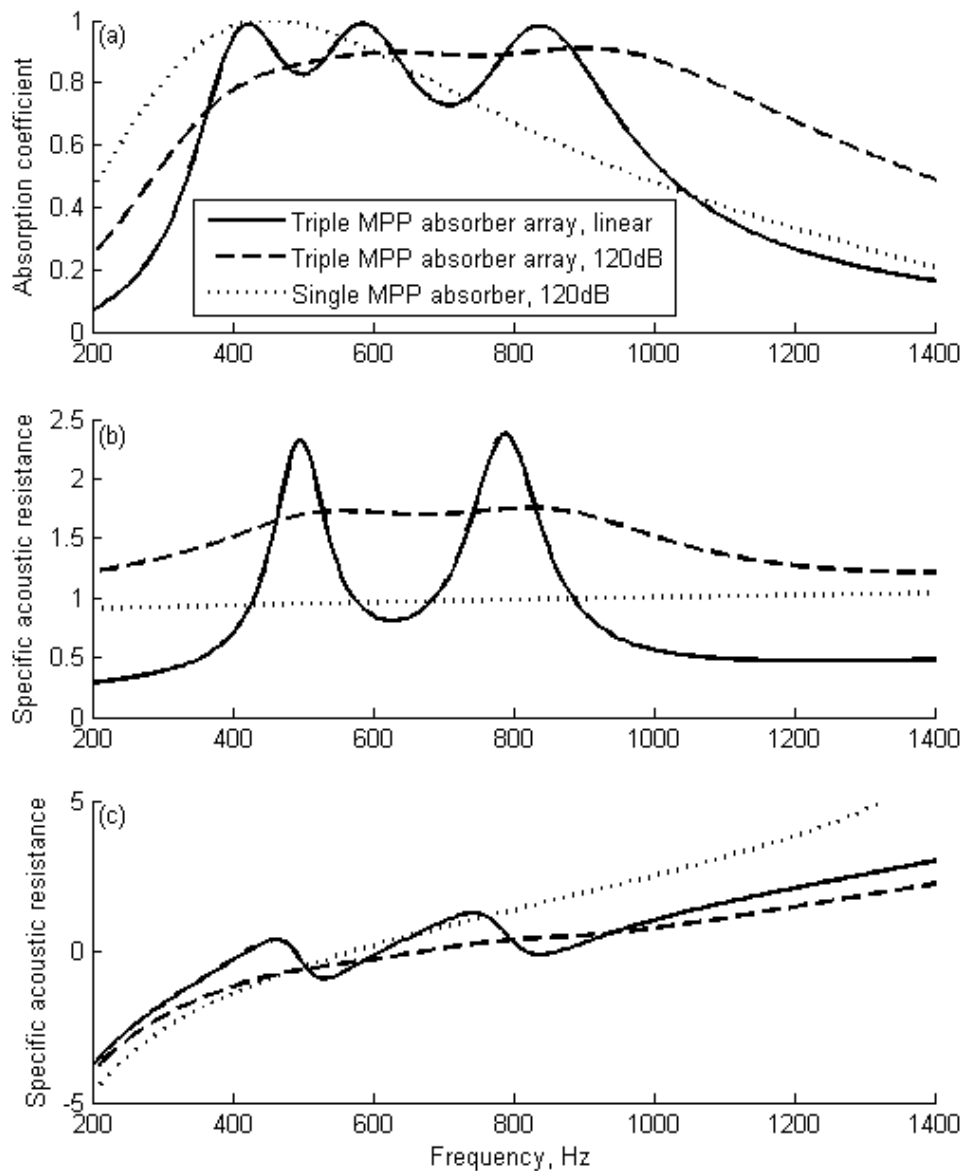


Figure 2.15 Acoustic properties of the MPP absorber array for MPP G. (a) Absorption coefficient; (b) Specific acoustic resistance; (c) Specific acoustic reactance. (—) Triple MPP absorber array in linear; (---) Triple MPP absorber array at $SPL_{incident} = 120$ dB; (· · ·) Single MPP absorber at $SPL_{incident} = 120$ dB.

2.4.3. Effects of Panel Vibration

The microperforated panel can be made of light materials. When the light MPP is adopted in an environment with moderate or high intensity sound, the effect of

structural vibration on the absorption performance of MPP would be considerable. Figure 2.16 shows the comparison of the absorption coefficients between the rigid MPP (dashed line) and flexible MPP with vibration (solid line). The numerical results are predicted for MPP F with dimensionless surface density $Ms = 6$ and bending stiffness $B = 0.003$. The normalizations of the surface density and the bending stiffness are $Ms = Ms^*/\rho_0^* h^*$ and $B = B^*/\rho_0^* (c_0^*)^2 (h^*)^3$ respectively, where ρ_0^* is the dimensional air density, c_0^* is the dimensional sound speed and h^* is the dimensional total height of the MPP absorber. The boundary conditions of the MPP are treated as clamped support at $y = 0$ and h , and simply supported by two partitions. The absorption coefficient of the MPP absorber array remains at high level ($\alpha > 0.8$) for the low frequency range until $f^* = 1000$ Hz. However, the absorption performance drops dramatically at around the third peak due to the effect of structural vibration. The trough observed at $f^* = 1234$ Hz leads to the half-absorption bandwidth reduction, which decreases from 4.38 to 3.19. The magnitude of the panel velocity in x -direction at $f^* = 980$ Hz and 1234 Hz is presented in Figures 2.16(b) and 2.16(c). At $f^* = 980$ Hz, the perforated panel is excited into vibration with small velocity, i.e., $u_p < 0.06$ m/s. However, at $f^* = 1234$ Hz, which is the local resonance frequency of cavity 3 roughly, the MPP vibrates vigorously especially for the middle region of the MPP due to the structural resonance. The maximum velocity of the panel vibration is $u_p = 0.238$ m/s, which is four times larger than that at $f^* = 980$ Hz, as shown in Figure 2.16(c). As indicated by the acoustic intensity vector inside the duct as in Figure 2.16(e), the strong structural vibration in the middle region of the MPP would cause the sound reflection. As a result, the acoustic performance of the MPP absorber array is degraded since the middle component MPP absorber fails to absorb sound energy.

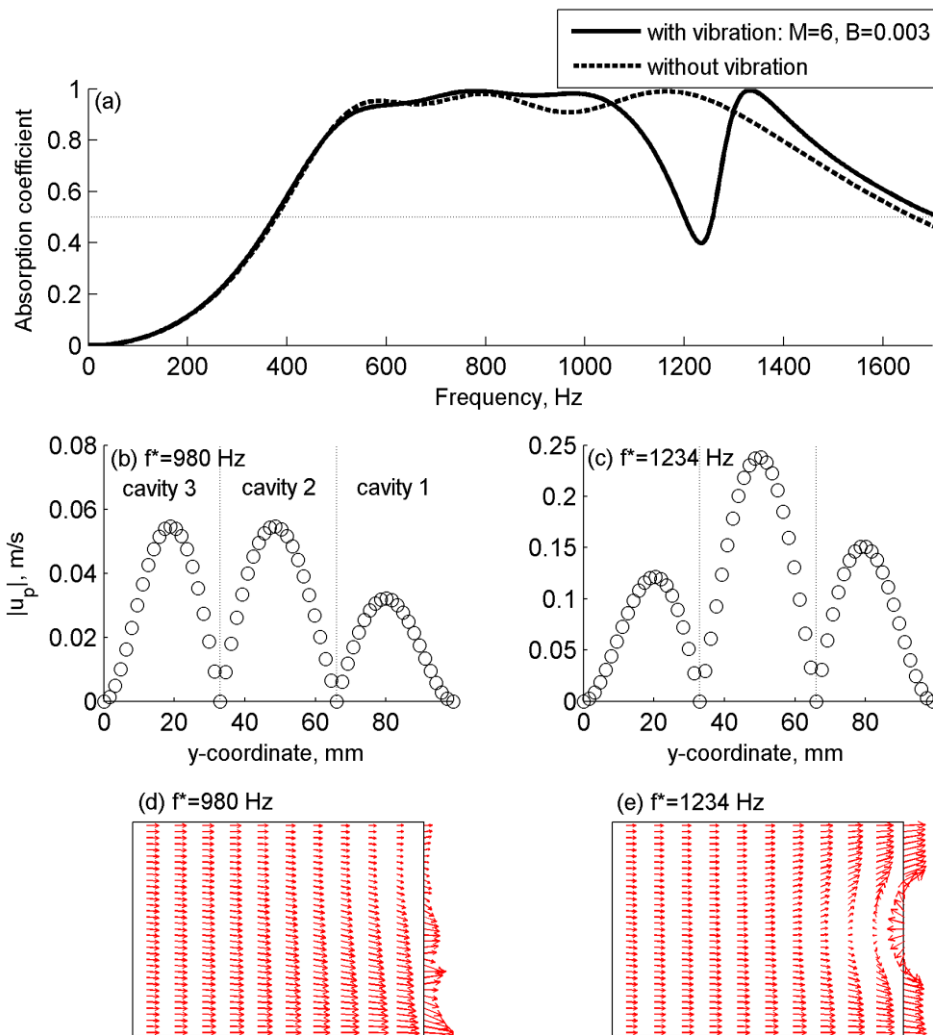


Figure 2.16 Comparison of the acoustic responses of the MPP absorber array between flexible and rigid MPP in the nonlinear regime. The results are obtained from MPP F. (a) Normal incidence absorption coefficients; (b) and (c) Amplitude of the panel vibrating velocities; (d) and (e) The acoustic intensity vector in the duct.

2.4.4. Optimization of Structural Parameters of MPP

As shown in Figure 2.16, the absorption performance of the MPP absorber array would be greatly affected by the structural vibration of the perforated panel. The material properties of the MPP should be selected appropriately in order to obtain the

optimal absorption performance with desirable bandwidth when it is subjected to high sound pressure. Figure 2.17(a) shows the optimal results of the single MPP absorber of $D_s = 100\text{mm}$ (dashed line) and triple MPP absorber array (dash-dot line) for MPP F with vibration at 120dB incident pressure level. Figures 2.17(b) and 2.17(c) display the half-absorption bandwidth contour as a function of surface density M_s and bending stiffness B for the single MPP absorber and triple MPP absorber array respectively. The solid lines on the contour show the peak value of the absorption coefficient achieved by MPP absorbers for the corresponding M_s and B . For the flexible single MPP absorber with optimal parameters $M_s = 26$ and $B = 0.008$, an absorption peak is induced by the structural resonance at a higher frequency $f^* = 1108$ Hz. As shown by Lee *et al.* (2005), such high absorption is caused by the high relative velocities between the panel and air particles. However, by comparing the result of rigid MPP represented by the solid line in Figure 2.17(a), the low frequency absorption performance of the optimal panel is degraded due to the effect of the structural vibration found at $f^* = 212$ Hz such that the half-absorption bandwidth is reduced from 3.21 to 2.99. For the triple MPP absorber array with $M_s = 20$ and $B = 0.002$, the absorption pattern is different between the cases with and without the panel vibration effect, which are represented by the dotted and dash-dot line respectively. However, it shows that the negative effect caused by the structural vibration of the panel on the half-absorption bandwidth of the MPP absorber array is significantly less than that of the single MPP absorber. Moreover, compared to the single MPP absorber, the contours show that the requirement of the bending stiffness of the optimal triple MPP absorber array can drop from 0.008 to 0.002 by 75% in order to achieve a wide half-absorption bandwidth. The corresponding optimized bandwidth of the MPP absorber

array can reach to 4.47 which significantly increases by about 49% when comparing with the single MPP absorber.

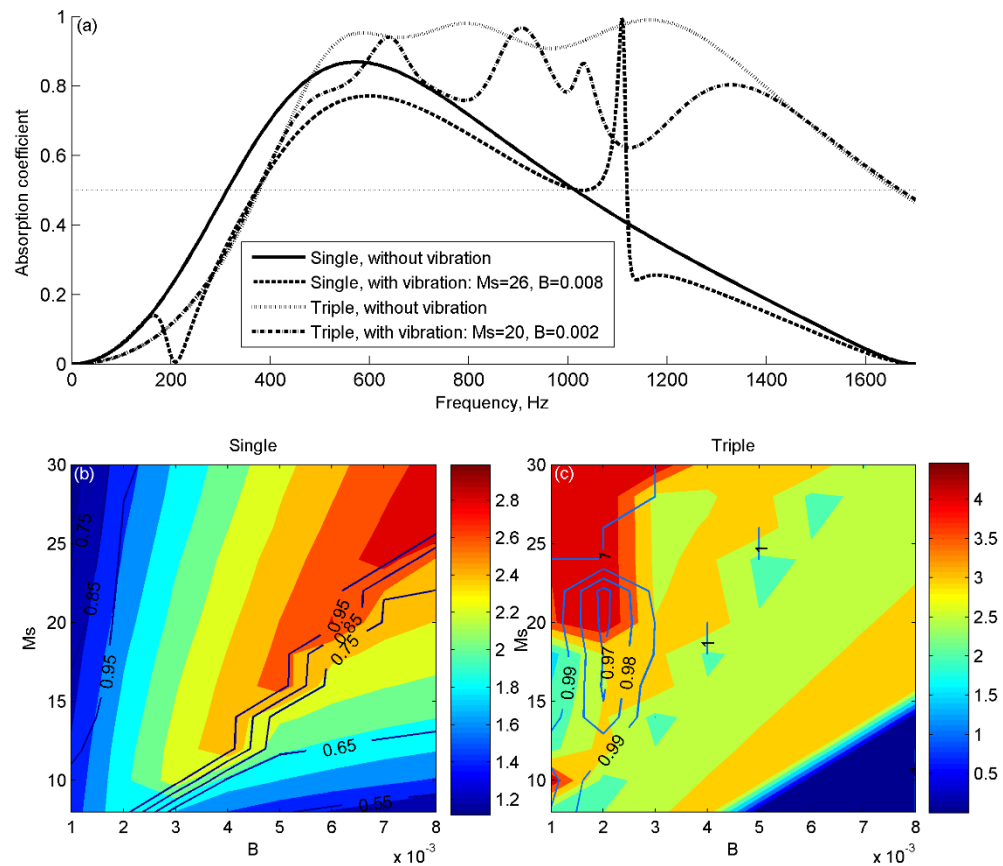


Figure 2.17 Optimal spectrum for the single MPP absorber and MPP absorber array in the nonlinear regime. (a) The normal absorption coefficients at optimal surface density and bending stiffness. The subfigures below show the optimal half-absorption bandwidth contour as a function of surface density M_s and bending stiffness B . (b) Single MPP absorber; (c) Triple MPP absorber array.

2.5. Experimental Measurement and Validation

The experimental study is conducted in both linear and nonlinear regimes to verify the finite element models established. The normal absorption coefficients of the MPP

absorber are measured experimentally by using the two-microphone transfer-function method. Figure 2.18 shows the experimental setup. A digital-to-analogue conversion card (PCI-M10-16E-1 from National Instruments) is used to generate the signal which is amplified by a B&K's amplifier (Lab Gruppen 300). The incident sound is generated by a loudspeaker. The acoustic pressure in the duct is measured by a pair of 1/2 in. microphones (B&K type 4947) were used and supported by a B&K's Nexus conditioning amplifier type 2693. The signals from the microphones are digitized by the National Instruments card PCI-4452. The A/D and D/A processes are both controlled by National Instruments' Labview program.

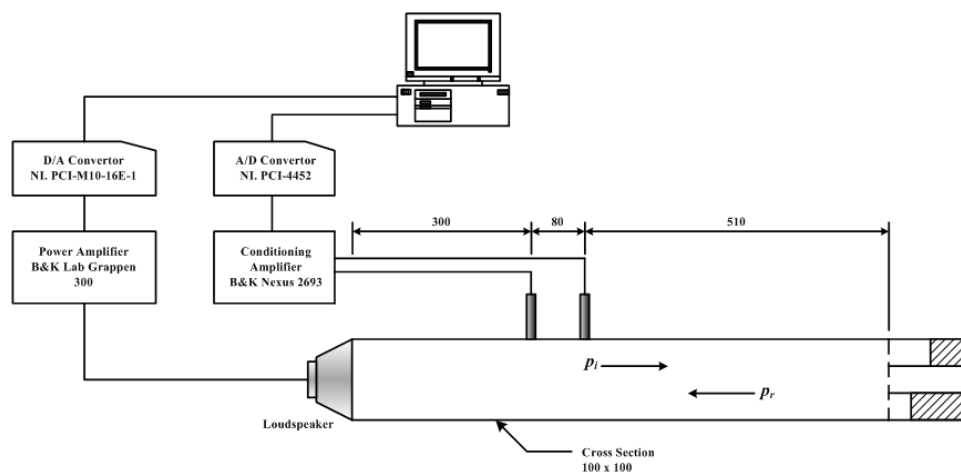


Figure 2.18 Experimental setup for measuring the normal incidence absorption coefficient by using the two-microphone method.

The microperforated panel is made of stainless steel. The parameters of the MPP are $t_{mpp} = 0.4$ mm, $d = 0.65$ mm and $\sigma = 1.76\%$. The backing cavity is partitioned into three sub-cavities by two aluminum plates with thickness 1 mm. The depths of sub-cavities are $D_1 = 50$ mm, $D_2 = 99$ mm and $D_3 = 25$ mm. The duct walls and cavity walls are made of acrylic of thickness 15mm. The cross-section area of the rectangular duct is 100 mm \times 100 mm. The first cut-on frequency is around 1700Hz. The

incidence pressure for the nonlinear case is 110dB. The Comparisons of normal absorption coefficients between the numerical predictions (solid line) and the experimentally measurements (open circle) for the prototype MPP absorber array were made in the linear and nonlinear regimes as shown in Figures 2.19(a) and 2.19(b) respectively. Three spectral peaks matched with the predictions can be observed in both cases. There is a good agreement between the numerical and measured results for the resonance frequencies and the sound absorption levels. The absorption improvement with broader half-absorption bandwidth at high sound pressure, as mentioned in Sec. III A, is successfully achieved by the experiments. Compared with the result in the linear regime, the half-absorption bandwidth of the MPP absorber array under moderate acoustic excitation increases from 3.42 to 4.18.

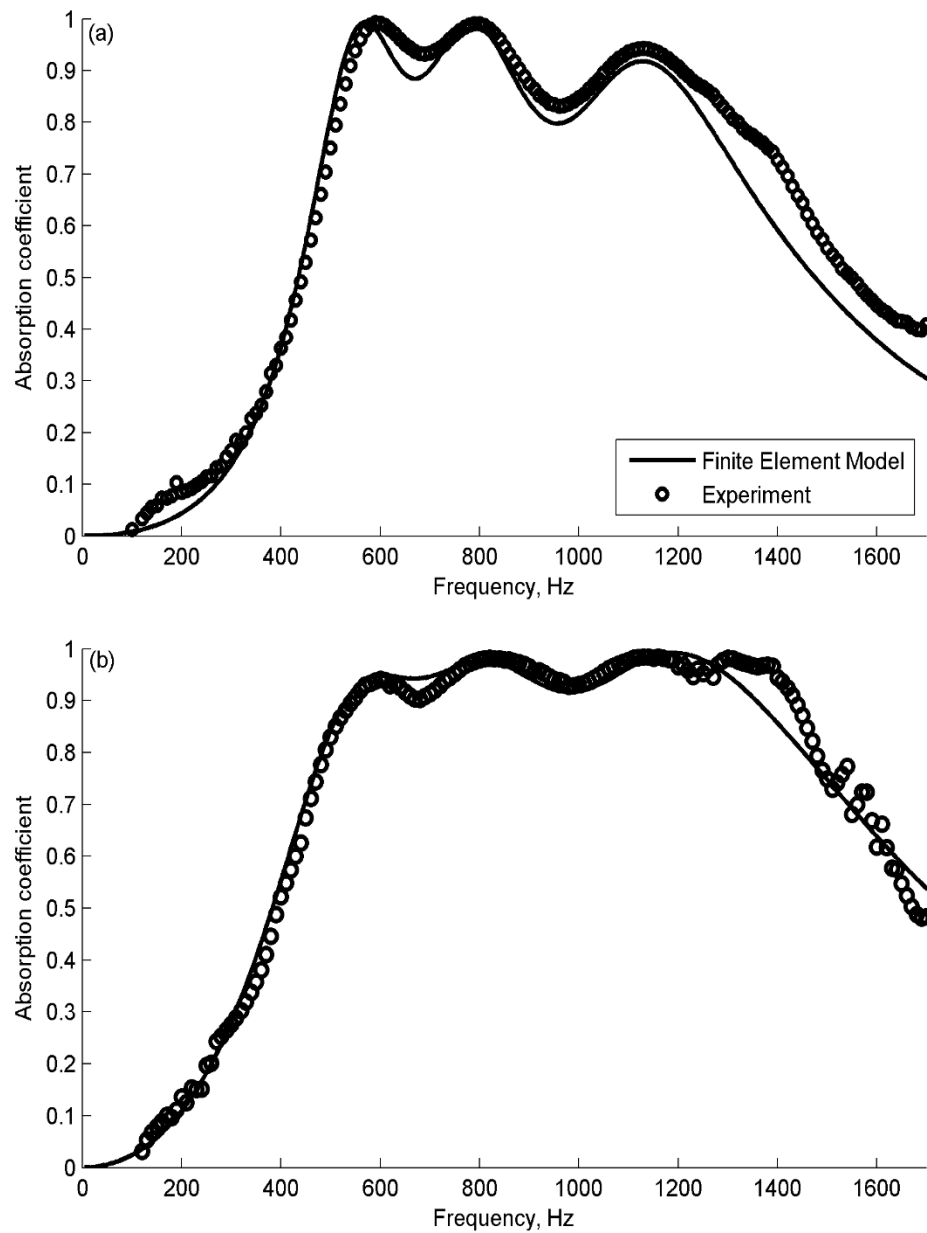


Figure 2.19 Comparison between the numerical predictions obtained from the finite element model and the experimental results of the MPP absorber array. (a) Linear; (b) Nonlinear at SPL=110dB. The MPP is made of stainless steel with parameters $t_{mpp} = 0.4\text{mm}$, $d = 0.65\text{mm}$ and $\sigma = 1.76\%$. The depths of three sub-cavities are $D_1 = 50\text{ mm}$, $D_2 = 99\text{ mm}$ and $D_3 = 25\text{ mm}$.

Besides, the numerical result of the MPP absorber array of inhomogeneous MPP is also verified by experiment as shown in Figure 2.20 at 105 dB. The inhomogeneous MPP of $d = 1.08$ mm, and perforation $\sigma_{1,2,3} = 0.85\%$, 1.15% and 0.85% is examined. The predicted absorption of the MPP absorber array in the linear and nonlinear regimes are represented by the solid and dashed line respectively. The experimental results for the linear case and nonlinear case are marked by red square and blue circle respectively. Compared with the result in the linear regime, the half-absorption bandwidth of the MPP absorber array under moderate acoustic excitation increases from 2.74 to 3.91.

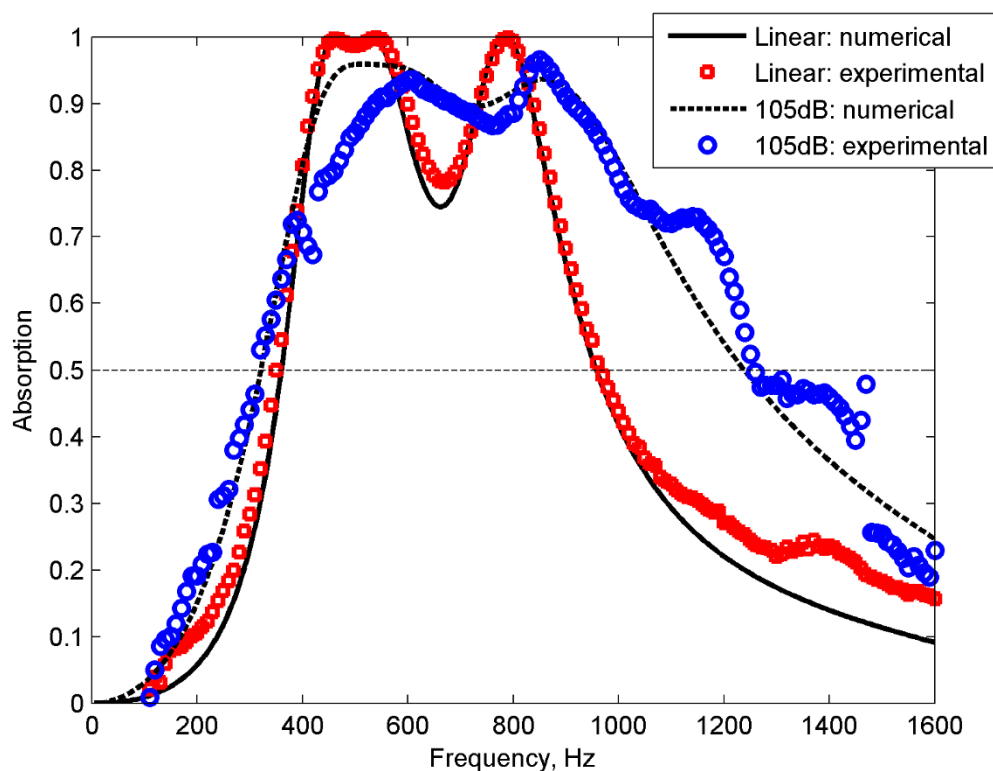


Figure 2.20 Comparison between the numerical predictions obtained from the finite element model and the experimental results of the MPP absorber array. The MPP is made of stainless steel with parameters $t_{mpp} = 0.4$ mm, $d = 1.08$ mm, $\sigma_{1,2,3} = 0.85\%$, 1.15% and 0.85% . The depths of three sub-cavities are $D_1 = 50$ mm, $D_2 = 99$ mm and $D_3 = 25$ mm.

2.6. Conclusions

In this chapter, the effect of the acoustic nonlinearity of orifice on the acoustic behavior of the microperforated panel absorber array is studied. The two-dimensional theoretical and finite element models of the MPP absorber array under normal incidence in the nonlinear regime are established. The following conclusions are made:

- 1) The parameters of the MPP including the panel thickness, orifice diameter and the perforation ratio would affect the absorption performance of the MPP absorber array. It is observed that the frequency range for half-absorption would shift to lower frequency for the thicker MPP absorber with smaller perforation ratio and orifice diameter. The parametric study provides basic information for the MPP absorber design.
- 2) The absorption performance of the MPP absorber array highly depends on the acoustic excitation. In general, a better absorption performance of the MPP absorbers can be achieved in the nonlinear regime due to the increase of acoustic resistance. If the incidence sound pressure further increases to a critical level, the contribution of the neighboring sub-cavity gives a significant added-mass effect to the MPP absorber array, and thus, the performance of the MPP absorber array behaves like the single MPP absorber but with a wider half-absorption bandwidth.
- 3) The absorption pattern of the MPP absorber array would be affected by the panel vibration. The absorption performance of the flexible MPP absorber array can be maintained by choosing the optimal surface density and bending stiffness of the panel. Otherwise, the dramatic drops on the absorption curve would be found due to the sound reflection induced by the structural resonance.

- 4) The finite element model of the MPP absorber array at high sound pressure is validated by experiment. The measured absorption coefficients of the MPP absorber array match well with the predicted results. The half-absorption bandwidth of the MPP absorber array with $t_{mpp} = 0.4\text{mm}$, $d = 0.65\text{mm}$ and $\sigma = 1.76\%$ can reach to 4.18 at $\text{SPL} = 110\text{dB}$.

Chapter Three

Performance of Micro-perforated Panel Silencer subject to Orifice Nonlinearity under Grazing Plane Wave Incidence

Numerous researchers proposed different silencers to control the duct noise, like the expansion chamber and Helmholtz resonator. Instead of the classic silencing device, Huang (2006) proposed the plate silencer which can successfully reduce the incident sound wave in a duct due to sound reflection. However, the strength to surface density of the plate is comparatively high in order to achieve a good silencing performance, which raises difficulty during implementation. Later, Wang *et al.* (2012) suggested a MPP silencer which replaced the panel of the plate silencer by the micro-perforated panel. The demand on the strength of panel is reduced with the use of MPP due to its promising absorption properties.

From the previous chapter, the influences of the orifice nonlinear features on the absorption properties of the MPP absorber are shown and discussed. The results suggest that the absorption performance of the MPP absorber is highly subjected to the acoustic excitation for normal incidence case. When the micro-perforated panel is used as a silencer to control the noise in a fan-ducted system with grazing incidence sound wave at high amplitude, the performance of MPP silencer would be affected by the nonlinear characteristic of the orifice. Therefore, the present study is conducted to

investigate the effect of the nonlinear properties of perforations on the noise attenuation mechanism of the MPP silencer subject to grazing plane wave incidence.

In this chapter, the finite element model of the MPP silencer is established in order to study the nonlinearity effect of perforations on the silencing performance of the MPP silencer with grazing incidence pressure at low Mach number. With the finite element model, the numerical results are obtained. The relationship between the incidence acoustic excitation and the acoustic response of the MPP silencer is discussed.

3.1. Finite Element Modeling of MPP Silencer

A two-dimensional finite element of the MPP silencer is established in both linear and nonlinear regime in order to investigate the nonlinearity effect of orifice on the acoustic response of the MPP silencer. The micro-perforated panels are flush mounted on duct of height a with the side branch backing cavities of depth h_c without partition. The MPP is of finite length L . The surface density and the bending stiffness of the MPP is represented by M_s and B respectively. In the current study, the incidence sound pressure level that is considered to induce the orifice nonlinearity is smaller than 120 dB. Hence the acoustic Mach number is low, and the acoustic field can be treated as linear. The schematic diagram of the MPP silencer subject to grazing incident sound wave p_i is shown in Figure 3.1.

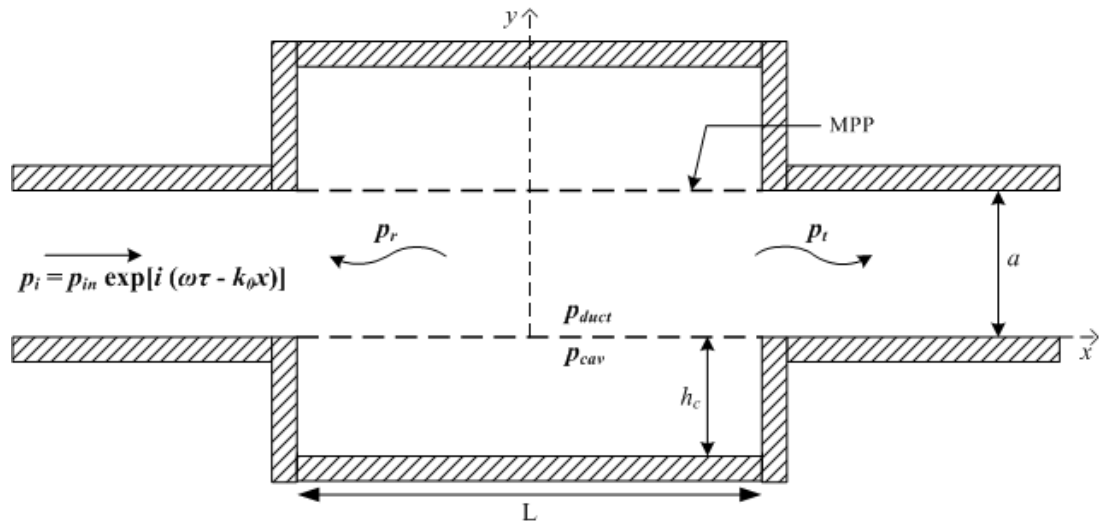


Figure 3.1 Two-dimensional configuration of the MPP silence.

The acoustic fields inside the duct and side branch backing cavities are governed by the Helmholtz equation as expressed by Eq. (2.8) in the previous chapter. The expression of the sound pressure and particle velocity in term of velocity potential and particle velocity is the same as Eq. (2.9).

The inlet and outlet boundaries of the duct at frequencies below the cut-on frequency are governed by the simple traveling wave relationships

$$\phi_{\pm} = B_{\pm} \exp[i(\omega\tau \mp k_0 x)] , \quad p_{\pm} = \pm \rho_0 c_0 u_{\pm} , \quad (3.1)$$

where the subscripts ‘+’ and ‘-’ indicate the downstream and upstream traveling waves respectively. At the exit boundary, it is assumed as an anechoic termination as

$$\frac{\partial \phi}{\partial x} + ik_0 \phi = 0 . \quad (3.2)$$

The plane sound wave is incident from the left hand side of the duct. The incident wave and the particle velocity are formulated as

$$p_i = p_{in} \exp[i(\omega\tau - k_0x)] , u_+ = \frac{p_i}{\rho_0 c_0} \quad (3.3)$$

The reflection wave p_r in the duct satisfies the upstream traveling wave relationship as shown in Eq. (3.1). Hence the total acoustic wave satisfies

$$p + \rho_0 c_0 u = p_+ + \rho_0 c_0 u_+ = 2\rho_0 c_0 u_+ . \quad (3.4)$$

The relationship of Eq. (3.4) can be expressed as

$$\frac{\partial \phi}{\partial \mathbf{n}} + ik_0 \phi = -2u_+ = -\frac{2p_i}{\rho_0 c_0} , \quad (3.5)$$

where \mathbf{n} is the normal direction of the boundary. For the acoustically rigid duct and cavity walls, the particle velocity vanishes in the normal direction \mathbf{n} , and hence the boundary condition can be expressed as

$$\mathbf{n} \cdot \nabla \phi = 0 . \quad (3.6)$$

The MPP silencer is a strongly vibro-acoustic coupled system. The noise attenuation is achieved as a combination of sound reflection excited by panel vibration and sound absorption provided by the perforations. The governing equation of the MPP motion and the boundary conditions of the ends of MPP are

$$\begin{aligned} B\nabla^4 w(x, \tau) - \omega^2 M_s w(x, \tau) &= p_{duct} - p_{cav}, & -L/2 < x < L/2 \\ w = 0, \quad \frac{\partial w}{\partial x} &= 0, & \text{fixed ending} \end{aligned} \quad (3.7)$$

where w is the displacement of the panel. The averaged velocity field at the interface of MPP is written as

$$\frac{\partial \phi}{\partial x} = \left(1 - \frac{\sigma \times \text{Im}(Z)}{Z}\right) \times u_p' + \frac{P_{cav} - P_{duct}}{\rho_0 c_0 Z}, \quad (3.8)$$

where the acoustic impedance of the MPP Z in the linear regime is the same as Eq. (2.1). With the increase of incidence acoustic excitation, the effect of orifice nonlinearity on the acoustic impedance of MPP is considered. According to Maa (1996), the nonlinear acoustic impedance of MPP used in this chapter is formulated as

$$\begin{aligned} Z &= Z_{resist,NL} + Z_{react,NL} \\ Z_{resist,NL} &= \frac{32\omega t_{mpp}}{\sigma \rho_0 c_0 d^2} \left[\left(1 + \frac{K^2}{32}\right)^{1/2} + \frac{\sqrt{2}}{8} K \frac{d}{t_{mpp}} \right] + \frac{v_0}{\sigma c_0}, \\ Z_{react,NL} &= \frac{i\omega t_{mpp}}{\sigma c_0} \left[1 + \left(9 + \frac{K^2}{2}\right)^{-1/2} + 0.85 \frac{d}{t_{mpp}} \left(1 + \frac{v_0}{\sigma c_0}\right)^{-1} \right] \end{aligned} \quad (3.9)$$

Where v_0 is the peak velocity in the orifice.

Eqs. (3.1) – (3.9) with the equations (2.1), (2.8) and (2.9) shown in chapter two are solved by using COMSOL Multiphysics. The transmission loss (TL) achieved by the MPP silencer is expressed as

$$\text{TL} = 10 \log_{10} \left(\frac{\int_{\text{outlet}} |\phi|^2 ds}{\int_{\text{inlet}} |\phi_i|^2 ds} \right), \quad (3.10)$$

where ϕ_i denotes the velocity potential of the incident sound wave. The sound wave reflection coefficient β and absorption coefficient α are

$$\beta = \frac{\int_{\text{inlet}} |\phi - \phi_i|^2 ds}{\int_{\text{inlet}} |\phi_i|^2 ds} \quad \text{and} \quad \alpha = 1 - \frac{\int_{\text{outlet}} |\phi|^2 ds + \int_{\text{inlet}} |\phi - \phi_i|^2 ds}{\int_{\text{inlet}} |\phi_i|^2 ds}. \quad (3.11)$$

3.2. Numerical Results and Discussion

Based on the finite element model established in Sec. 3.1, the performance of the MPP silencer, which is represented by TL, is predicted. In this section, the numerical model is discretized as the triangular quadratic-Lagrange elements. The maximum element size is 0.03m and the mesh consists of 28155 elements totally. The noise suppression mechanism of the silencer is investigated with the three different MPPs. The parameters of the MPPs are listed as Table 3.1. The depth of backing cavity is $h_c^* = 100$ mm.

	Thickness (t_{mpp})	Orifice diameter (d)	Perforation ratio (σ)
MPP 1	0.5 mm	0.5 mm	1%
MPP 2	0.4 mm	1 mm	1.94%
MPP 3	0.5 mm	0.7 mm	0.7%

Table 3.1 Parameters of MPPs used in MPP silencer.

3.2.1. Noise Attenuation Mechanism subject to Orifice Nonlinearity

Figure 3.2 shows the comparison of transmission loss achieved by the MPP silencer between linear (solid line) and nonlinear cases at incidence sound pressure level 100 dB (dashed line) and 110 dB (dotted line). The numerical results of MPP 1 with $L = 2$ and $B = 0.008$, but of different surface density $Ms = 2$ are illustrated in Figure 3.2. In the linear regime, two sharp peaks are observed at around $f^* = 475$ Hz and 965 Hz with $TL = 17.26$ dB and 19.29 dB respectively. However, the TL drops down immediately after reaching those two peaks. In between the sharp peaks, at the middle frequency range starting from $f^* = 515$ Hz, there is a good noise reduction performance with $TL > 10$ dB from 515 Hz to 760 Hz. The maximum TL in this middle frequency

range is 13.65 dB at $f^* = 635$ Hz. When the incidence sound pressure increases to higher levels, the curves of TL are different from that of the linear case. The frequency of the first sharp peak is shifted to a lower frequency with the increase of incidence acoustic excitation, which is found at $f^* = 455$ Hz at 110 dB. On the other hand, the second peak is found at a higher frequency $f^* = 980$ Hz for the nonlinear case with 110 dB when comparing with the linear one. In the middle frequency range, the maximum TL is reduced to 12.58 dB and 11.24 dB for $\text{SPL}_{\text{incident}} = 100$ dB and 110 dB respectively.

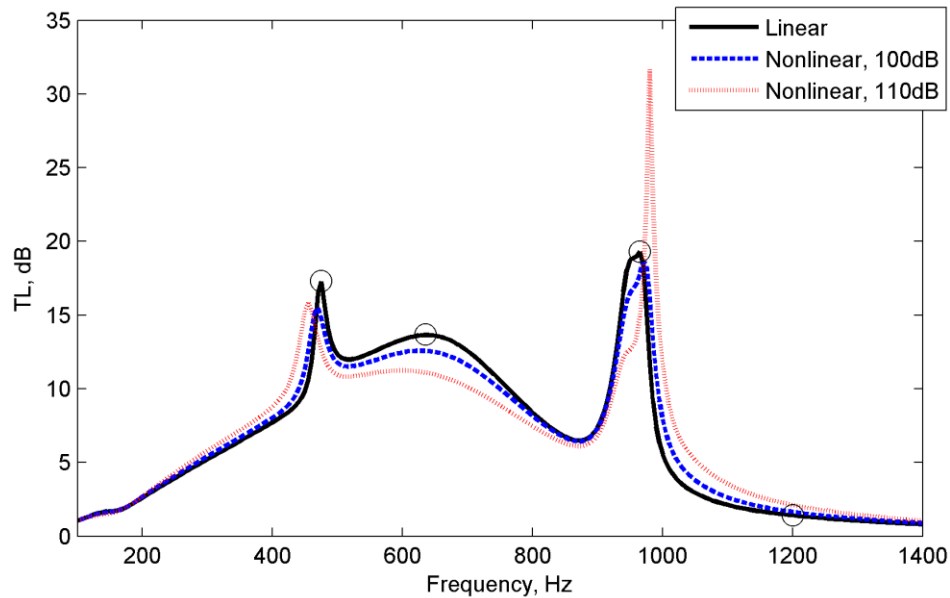


Figure 3.2 Comparison of TL of the MPP silencer at different incidence sound pressure level for MPP 1 of $M_s = 2$ and $B = 0.008$.

The acoustic response of the silencing device performs differently at different frequencies, since the noise suppression mechanism of the MPP silencer is a combination of sound reflection and acoustic absorption. The time-averaged sound intensity, i.e., $I_x = 0.5 \times \text{Re}[p(y) \times \bar{u}(y)]$ (Russell *et al.*, 2013) inside the duct and cavity

for the linear case at $f^* = 475$ Hz, 635 Hz, 965 Hz and 1200 Hz are shown as Figures 3.3, 3.4, 3.5 and 3.6 respectively. At $f^* = 475$ Hz in which the first sharp TL peak is observed, it is found that the acoustic energy is reflected back to the upstream which is induced due to the panel vibration. For the cases at $f^* = 635$ Hz and 965 Hz, the noise is controlled by both reflection and absorption. At $f^* = 635$ Hz, part of the acoustic energy is attracted to the cavity for sound absorption in the front part of MPP, and part of the sound energy is reflected. The sound reflection and absorption behaviors given by the MPP silencer are more significant at $f^* = 965$ Hz, in which the second sharp TL peak appears, as shown in Figure 3.5. The silencing performance of the MPP silencer is relatively insignificant at $f^* = 1200$ Hz since only a very small part of acoustic energy is dissipated, most of the acoustic energy can continuously propagate to the downstream of duct.

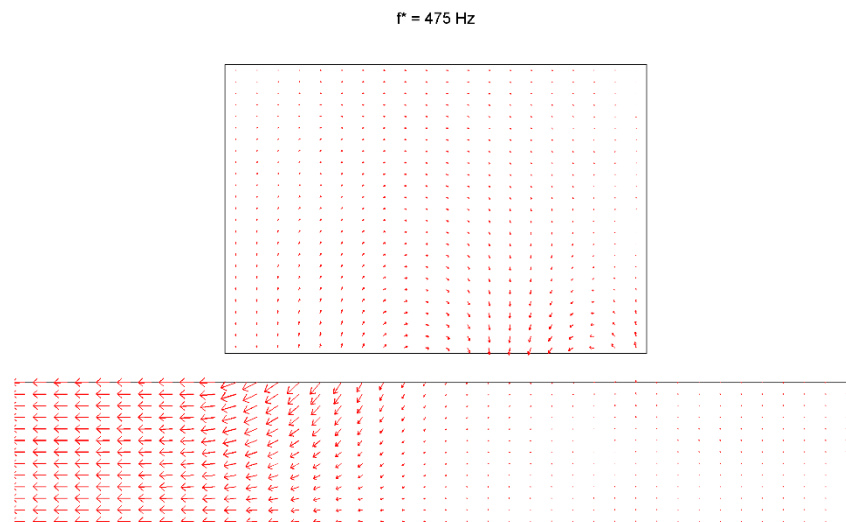


Figure 3.3 Time-averaged acoustic intensity at $f^* = 475$ Hz.

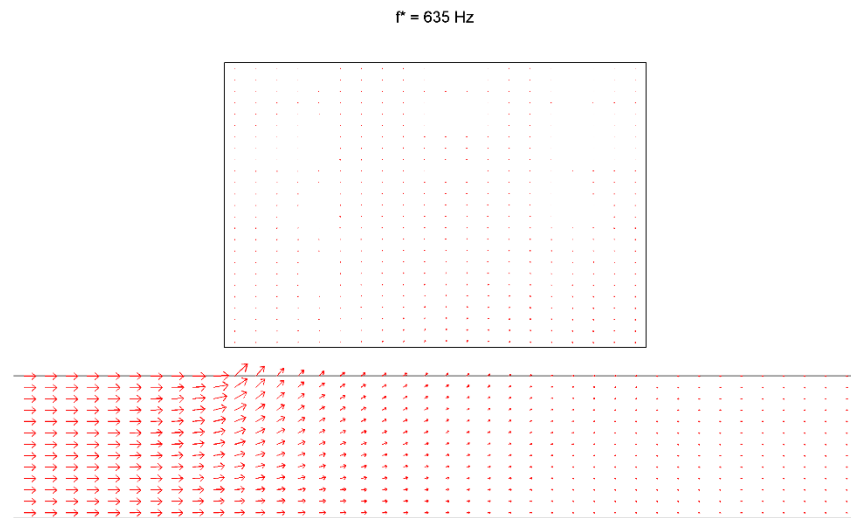


Figure 3.4 Time-averaged acoustic intensity at $f^* = 635 \text{ Hz}$.

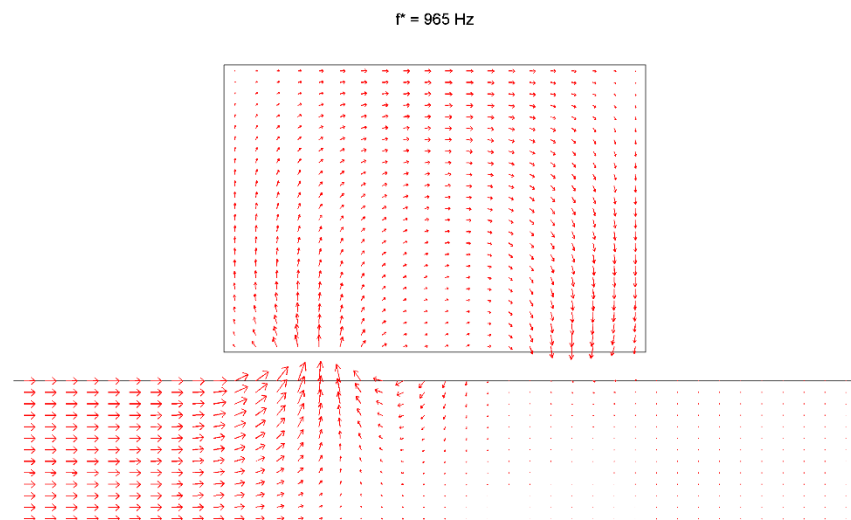


Figure 3.5 Time-averaged acoustic intensity at $f^* = 965 \text{ Hz}$.

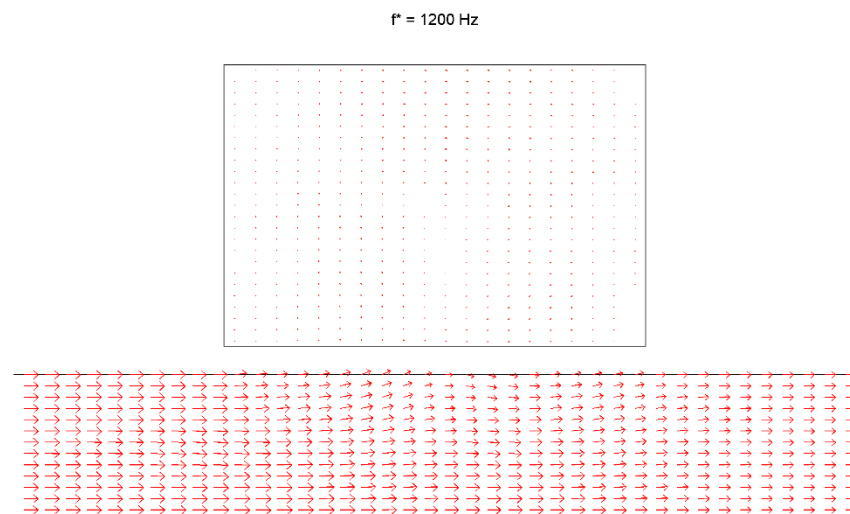


Figure 3.6 Time-averaged acoustic intensity at $f^* = 1200 \text{ Hz}$.

The reflection coefficient and the absorption coefficient of the MPP 1 with $M_s = 2$ are indicated in Figures 3.7(a) and 3.7(b) respectively. For the first TL peak at frequency around 460 Hz, Figure 3.7 illustrates that the absorption coefficient of the MPP silencer increases with the incidence sound pressure, which agrees with the observation as described in chapter two, but the reflection coefficient is reducing. Although the absorption coefficient of the MPP silencer is higher at high sound intensity due to the nonlinearity effect of orifice, the performance of the MPP silencer is better in the linear regime since the sound reflection is dominant at this frequency. In the middle frequency range from 470 Hz to 970 Hz, the performance is degraded due to the reduction of sound reflection as shown in Figure 3.3. The noise reduction attributed to sound reflection is still relatively more effective than the acoustic absorption, and hence the silencing performance of the MPP silencer in the linear regime is better due to a better sound reflection performance. At $f^* = 965 \text{ Hz}$, it is found that most of the acoustic energy is attracted to the MPP silencer for sound

absorption as shown in Figure 3.5. The absorption coefficient α increases from 0.68 and 0.97 respectively by comparing the solid and dotted lines in Figure 3.7(b). As a result, the peak with $TL = 31$ dB can be reached for $SPL_{incident} = 110$ dB.

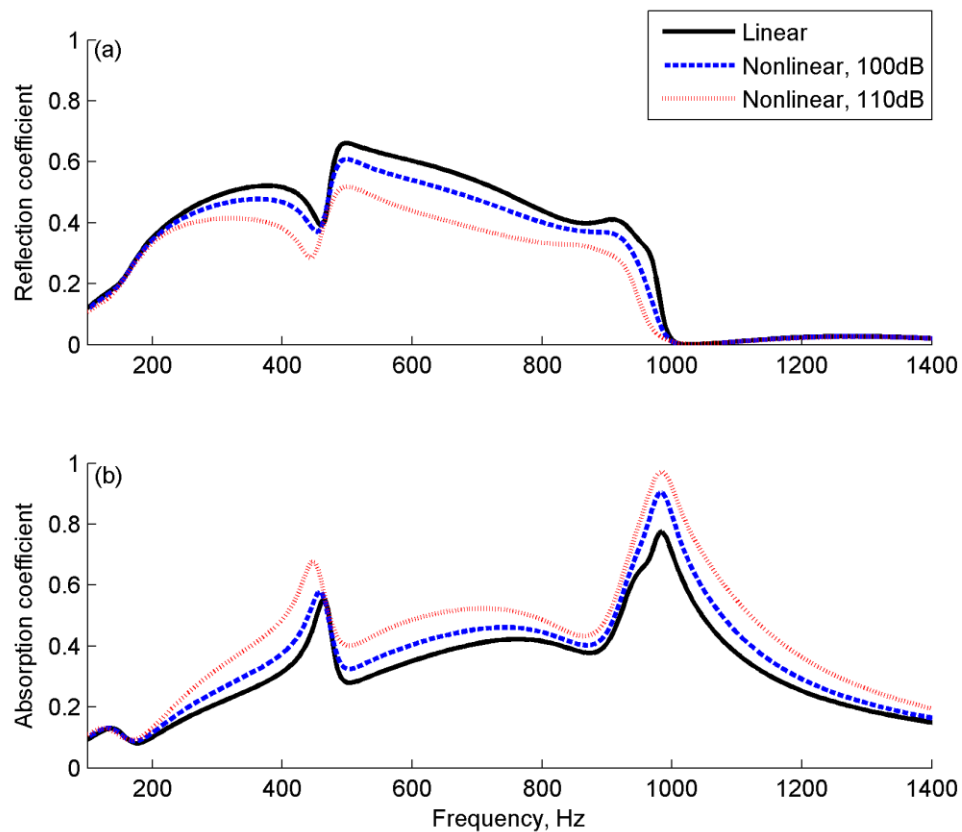


Figure 3.7 Acoustic response of the MPP silencer for MPP 1 of $M_s = 2$. (a) Reflection coefficient; (b) Absorption coefficient.

3.2.2. Parametric Studies of MPP silencer

The performance of the MPP silencer is examined with different structural properties of the panel, i.e. surface density M_s and bending stiffness B , and also with different parameters of the MPP, including the length of panel L and the panel thickness t_{mpp} . The incidence sound pressure level is taken as 110 dB for the nonlinear case. The change of the acoustic response of the MPP silencer with different structural

properties of panel is analyzed in Sec. 3.2.2.1 for MPP 2 of $L = 3$. The noise reduction performance of the MPP silencer with different parameters of MPP is studied in Sec. 3.2.2.2 for MPP 3 of $L = 5$. The performance of the MPP silencer is described by the value of TL and the bandwidth (or stopband) which is defined as the ratio of the upper frequency limit to the lower frequency limit for $TL \geq 5$ dB.

3.2.2.1. Structural Properties of Panel

The silencing performance of the MPP silencer for MPP 2 with surface density of the panel $M_s = 3, 5$ and 7 between the linear case (solid line) and nonlinear case (dashed line) is compared in Figures 3.8(a), 3.8(b) and 3.8(c) respectively. The bending stiffness of MPP 2 is $B = 0.05$. From Figure 3.8(a), in the linear regime, a stopband with the bandwidth 1.92 is observed at low frequency from $f^* = 255$ Hz to 490 Hz, i.e. bandwidth = $f_{UI}/f_{LI} = 490$ Hz / 255 Hz. Such low frequency stopband can also be achieved for the MPP silencer at high sound intensity, but with a smaller bandwidth 1.84. Although the low frequency bandwidth is slightly reduced, the nonlinearity effect of perforations leads to the second stopband from $f^* = 720$ Hz to 1280 Hz. The second bandwidth at high sound pressure is 1.78. The wider bandwidth instead of two narrow TL peaks are obtained at 110 dB due to the improved sound reflection from $f^* = 720$ Hz to 850 Hz and acoustic absorption from $f^* = 800$ Hz as shown in Figures 3.9(1a) and 3.9(1b) respectively. The wider second stopband is always observed even for the heavier MPPs which is illustrated in Figures 3.8(b) and 3.8(c), in which the second bandwidths are improved 21% and 51% for $M_s = 5$ and 7 respectively. The significant enhancements of TL found in the second stopband are mainly attributed to

the improvement of sound absorption which is induced by the nonlinearity features of orifices as shown in Figure 3.9.

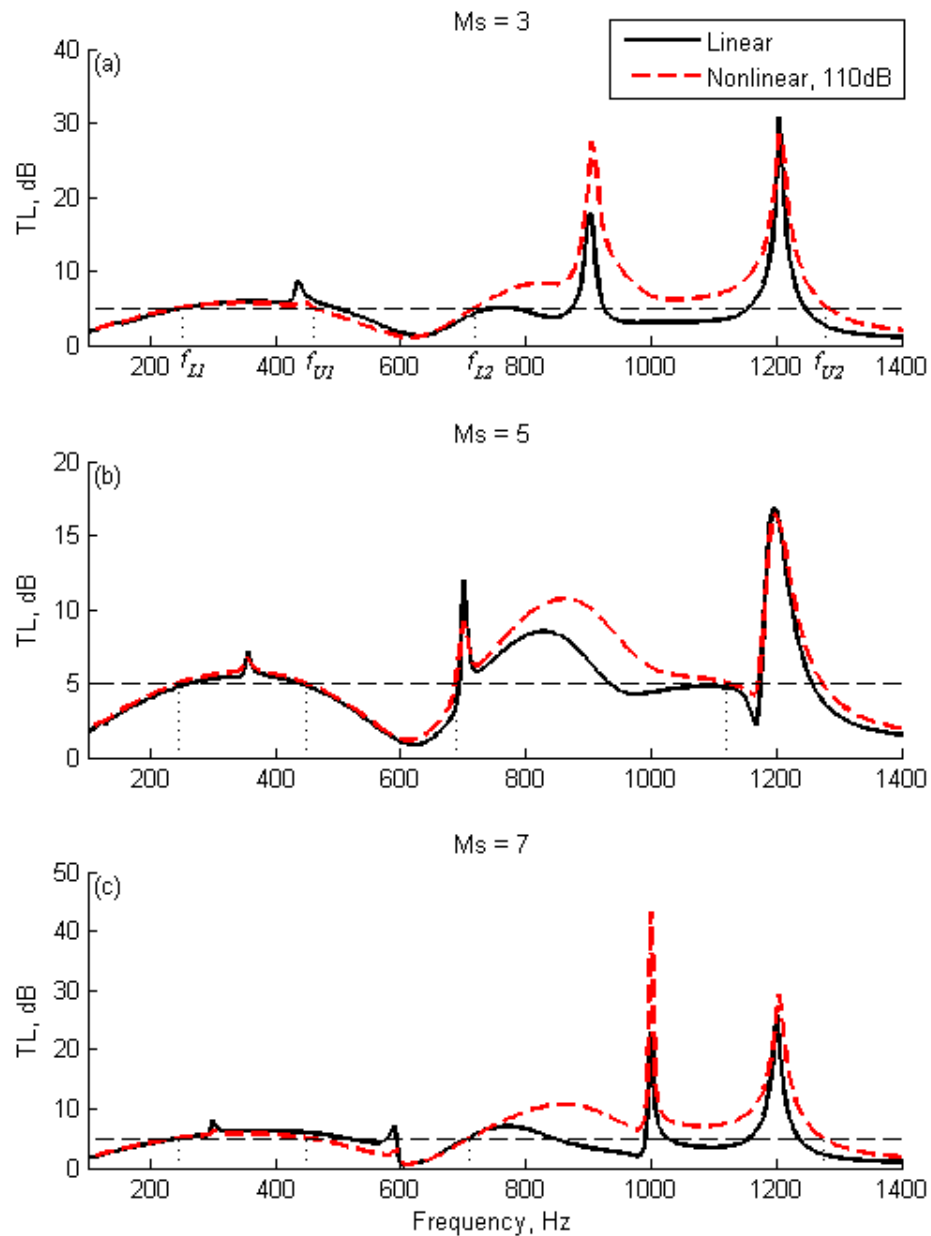


Figure 3.8 TL achieved by MPP silencer with different surface density for MPP 2.
(a) $M_s = 3$; (b) $M_s = 5$; (c) $M_s = 7$.

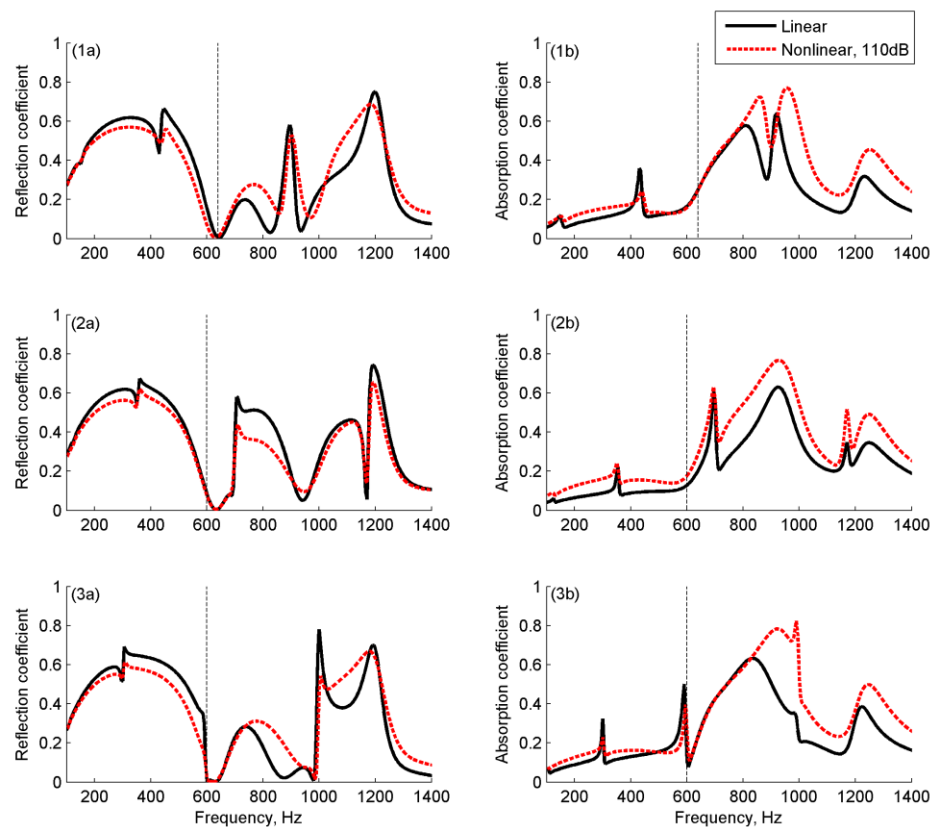


Figure 3.9 Acoustic response of MPP silencer with different surface density for MPP 2. Left column represents the reflection coefficient and the right one denotes the absorption coefficient. (1) $M_s = 3$; (2) $M_s = 5$; (3) $M_s = 7$.

Apart from the surface density, the effect of the orifice nonlinearity on the silencing performance of the MPP silencer with different bending stiffness of the panel is examined as shown in Figure. 3.10. For the first stopband in the low frequency range from 100 Hz to 600 Hz, the performance of the MPP silencer can be maintained with less than 10% reduction in the nonlinear regime at 110 dB for the three cases of $B = 0.05, 0.15$ and 0.25 . Although the upper frequency limit of the first stopband is shifted to lower frequency, the lower frequency limit moves to lower frequency as well. As shown in Figure 3.10(b) with $B = 0.15$, the first stopband for the linear case (solid line) is found from $f^* = 260$ Hz to 485 Hz, and that of the nonlinear case (dashed line) is

shifted to $f^* = 250$ Hz to 445 Hz, in which only 5% reduction of bandwidth is induced. In the linear regime, second and third stopbands with narrow band are observed in Figure 3.10(b). With the increase of acoustic excitation, a wider second bandwidth can be obtained, which increases from 1.07 to 1.77, since the TL in between the second and third stopbands is improved due to enhancement of sound reflection and absorption in the nonlinear regime as indicated in Figures 3.11(2a) and 3.11(2b). The similar results could be obtained for the MPP with $B = 0.05$ and 0.25.

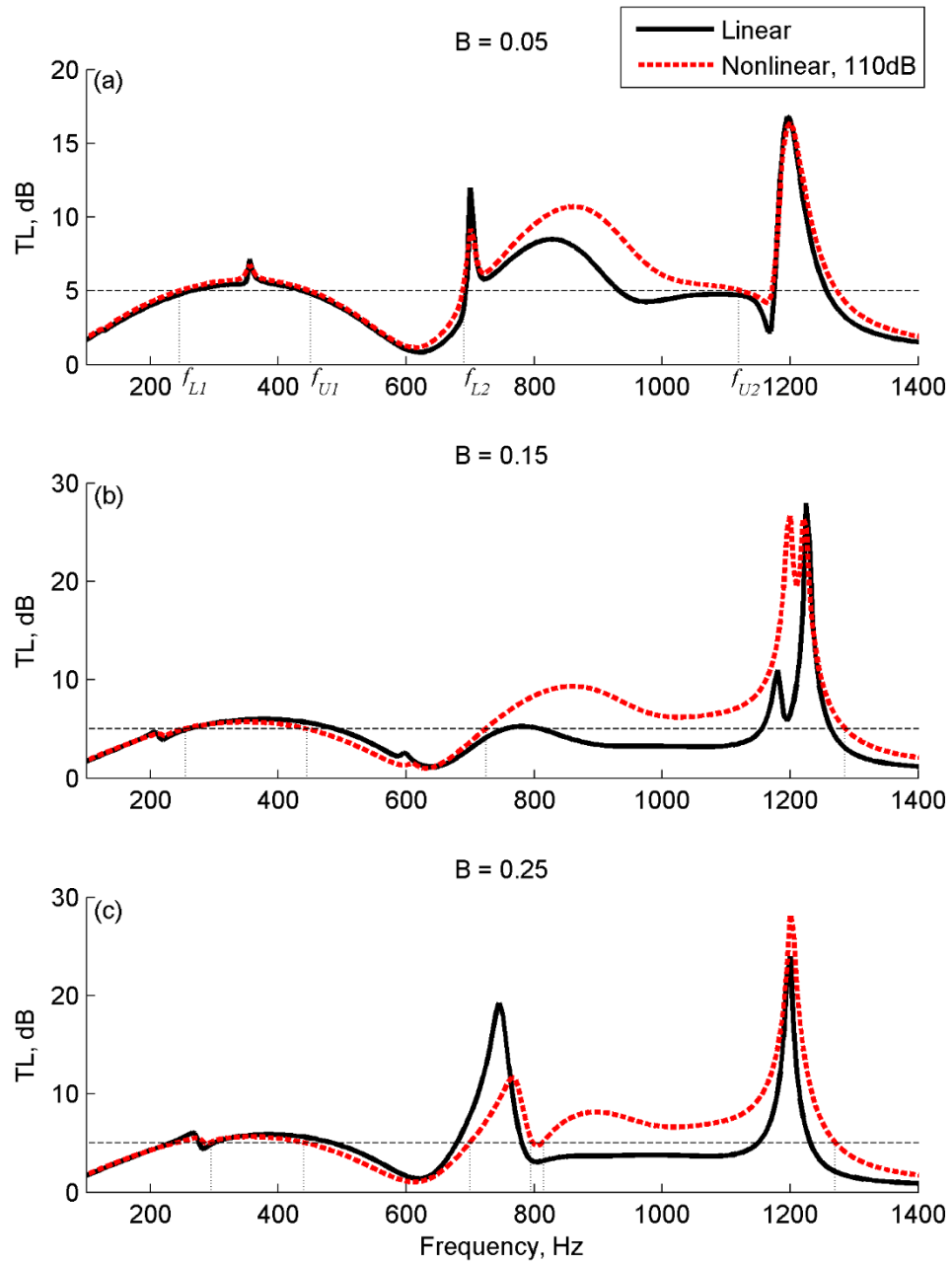


Figure 3.10 TL achieved by MPP silencer with different bending stiffness for MPP 2 of $M_s = 5$. (a) $B = 0.05$; (b) $B = 0.15$; (c) $B = 0.25$.

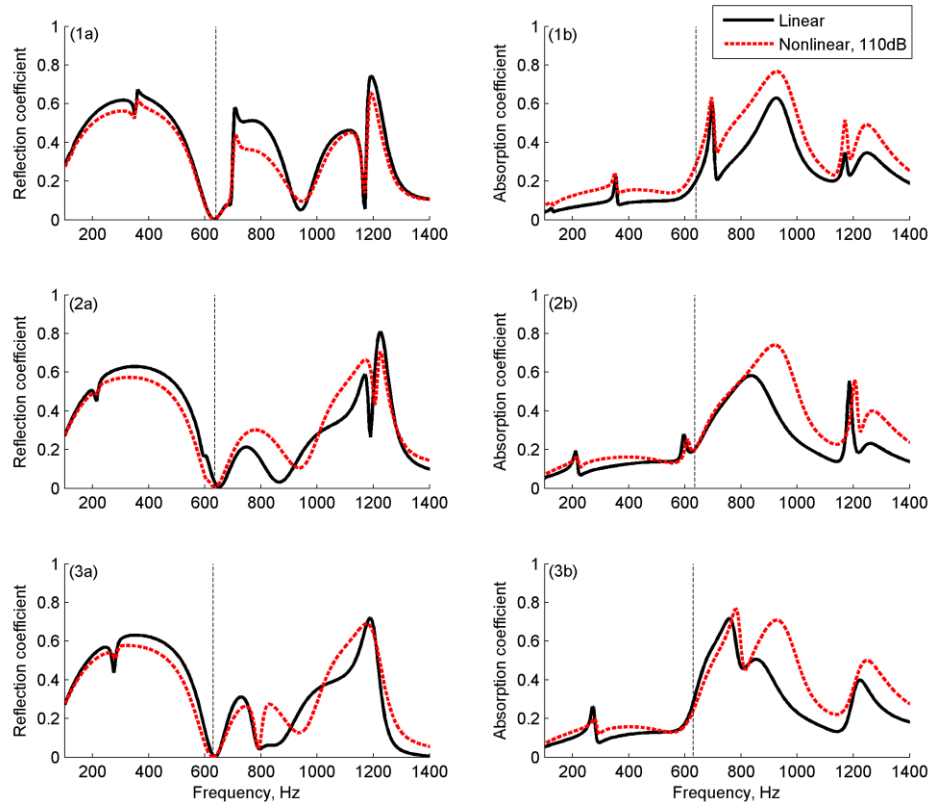


Figure 3.11 Acoustic response of MPP silencer with different bending stiffness for MPP 2 of $M_s = 5$. Left column represents the reflection coefficient and the right one denotes the absorption coefficient. (1) $B = 0.05$; (2) $B = 0.15$; (3) $B = 0.25$.

3.2.2.2. Parameters of MPP

The comparison of transmission loss of the MPP silencer for MPP 3 of $L = 5$ between the linear (solid line) and nonlinear cases (dashed line) is shown in Figure 3.12(1b). Following the same finding observed in Sec. 3.2.2.1, the trough with $TL = 2.8$ dB at $f^* = 900$ Hz in between the second and third stopbands presented in the linear regime is improved to 6.9 dB in the nonlinear regime at $SPL_{\text{incident}} = 110$ dB. At $f^* = 900$ Hz, the sound reflection is insignificant as shown in Figure 3.12(2b) for the linear and nonlinear regimes. The silencing performance of the MPP silencer greatly depends on the absorption performance of the MPP. From Figure 3.12(3b), a better acoustic

absorption is obtained due to the nonlinearity effect of MPP, and hence a wider stopband is achieved at high sound intensity. When a shorter panel of $L = 2.5$ is used for the MPP silencer, the trough at around $f^* = 700$ Hz is improved and the bandwidth of the MPP silencer can reach to 3.36 in the nonlinear regime. However, the effect of the sound absorption enhancement on the overall TL is insignificant since the sound reflection is dominant.

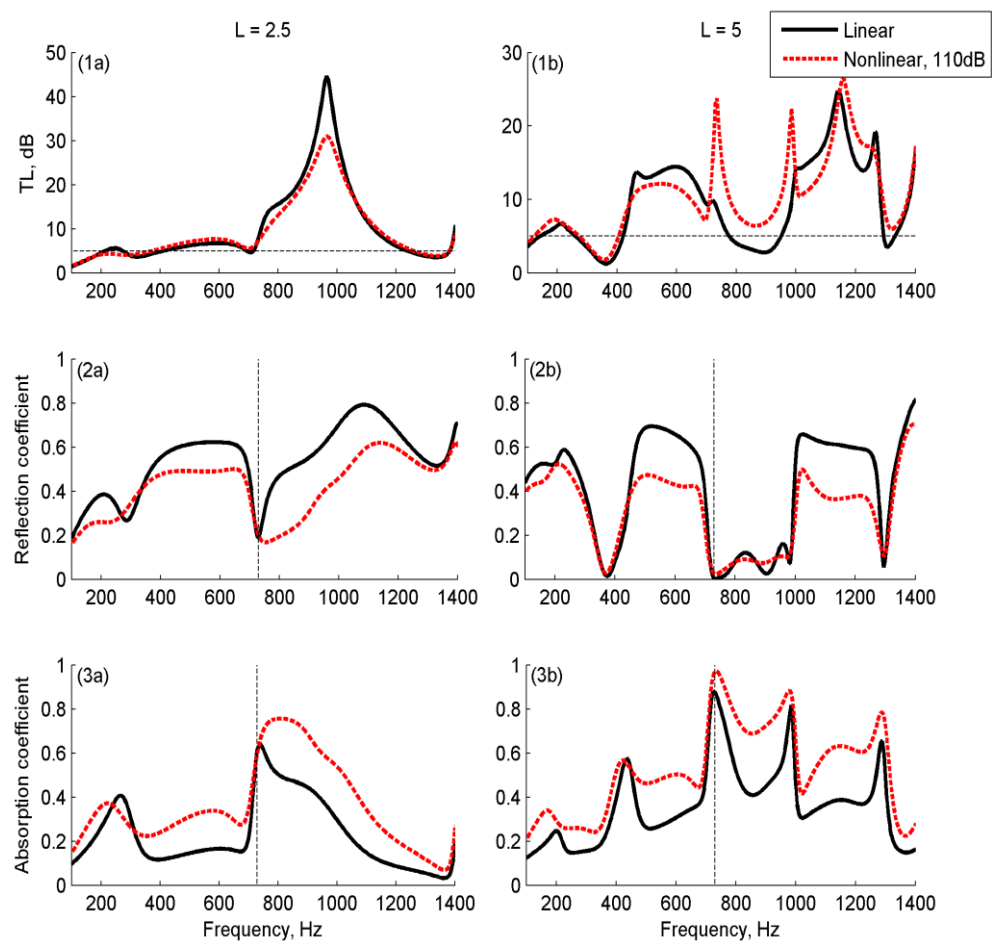


Figure 3.12 Acoustic response of MPP silencer with different length of panel for MPP 3. Left column represents the results of $L = 2.5$ and the right one denotes the results of $L = 5$. (1) TL; (2) Reflection coefficient; (3) Absorption coefficient.

The effect of the additional sound absorption provided by the nonlinearity effect of the orifice on the TL of the MPP silencer is also investigated with different the panel thickness t_{mpp} , which is shown in Figure 3.13. The change of the overall TL for the thicker MPP is insignificant in the nonlinear regime since the reflection coefficient is relatively higher than the absorption coefficient, which means that sound reflection induced by panel vibration is dominant. The effect of the additional sound absorption provided by the nonlinearity effect of the orifice on the TL is insignificant if sound reflection is dominant, hence only slightly increase of TL from $f^* = 700$ Hz to 970 Hz can be observed.

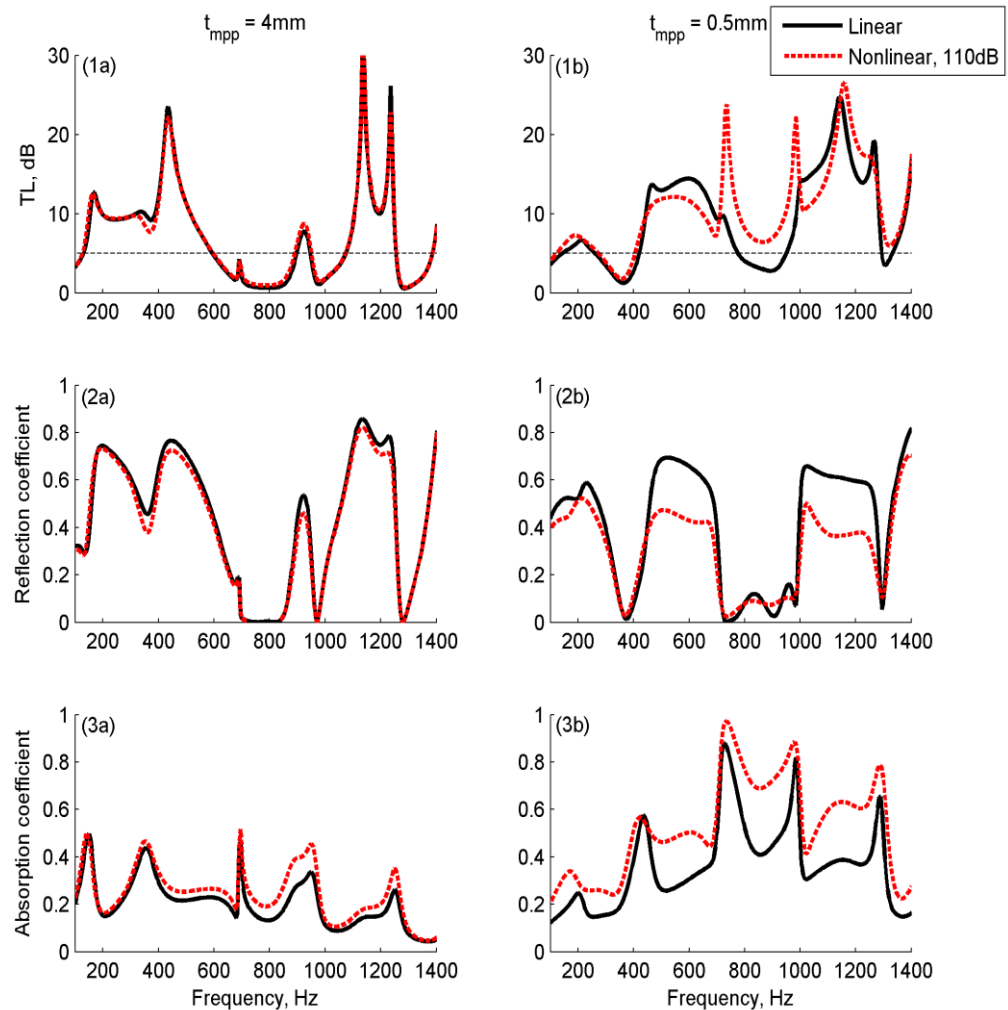


Figure 3.13 Acoustic response of MPP silencer with different panel thickness for MPP 3. Left column represents the results of $t_{mpp} = 4\text{mm}$ and the right one denotes the results of $t_{mpp} = 0.5\text{mm}$. (1) TL; (2) Reflection coefficient; (3) Absorption coefficient.

3.3. Conclusions

In this chapter, the silencing performance of the microperforated panel silencer subject to the effect of the acoustic nonlinearity of orifice is investigated. The two-dimensional finite element model of the MPP silencer under grazing plane wave incidence in the nonlinear regime is established. The following conclusions are made:

- 1) The silencing performance of the MPP silencer is achieved as a combination of sound reflection induced by panel oscillation and acoustic absorption given by the perforations. The contributions of these two noise suppression mechanisms vary at different frequencies. The performance of the silencer is improved by the effect of orifice nonlinearity when sound absorption mechanism is dominant.

- 2) The parametric study of the MPP silencer is conducted with different structural properties of the panel, i.e. surface density M_s and bending stiffness B , and also with different parameters of the MPP, including the length of panel L and the panel thickness t_{mpp} . It is observed that the second and third stopbands with narrow bandwidth obtained in the linear regime can be widened with the increase of incidence sound pressure level. The broader stopband is achieved in the nonlinear regime due to the additional absorption given by the nonlinear effect of perforations in between the second and third stopbands.

Chapter Four

Theoretical Studies on the Sound Attenuation Mechanism of a Tensioned Membrane Housing Device in Flow Duct

Apart from the micro-perforated panel silencer, the membrane house device is another fibreless passive approach that is used to control the duct noise. Huang (1999) firstly introduced the noise reduction mechanism of the drum-like silence which composed of two tensioned membranes in light weight with two backing cavities in order to control the incidence plane wave in duct. Choy and Huang (2005) showed that a good performance can also be achieved by such a reactive device in the duct with mean flow based on the sound reflection mechanism. Apart from the uniform mean flow, the time-dependent turbulent flow is another flow condition that could be found in the fan-ducted system. Tang (2011) used a point vortex with grazing flow to represent the turbulent flow in order to investigate the aero-acoustic-structural interaction of the drum-like silencer in the duct with unsteady flow. Later, Liu *et al.* (2012) adopted the concept of the drum-like silencer to attenuate the fan noise directly at its source position. The performance of such device in the fan-ducted system was studied analytically with a steady mean flow. The fan noise radiation is simplified as a dipole source. However, in the practical fan-ducted system, the flow condition is no long a steady mean flow. The time-varying turbulent flow should be taken into account, and hence the vibro-acoustic coupling mechanism would be more complicated.

This chapter examines the fluid-acoustic-structural interactions and the aeroacoustic generation mechanism of the flush-mounted flexible membrane backed by a cavity at the source position, which is called as a membrane housing device, in a fan-ducted system. The theoretical model is described in Sec. 4.1. The numerical results about the time-varying fluid-structural interactions and the sound generation mechanism are shown in Sec. 4.2. Sec. 4.3 outlines the short conclusions of this chapter.

4.1. Theoretical Modeling of Membrane Housing Device

The membrane housing device consists of two tensioned membranes of light mass m with finite length L and two side-branch cavities of depth h_c . The tension T is applied along the axial direction. A two-dimensional schematic diagram of the membrane housing device is shown in Figure 4.1. The membrane housing device is flush-mounted on a duct of height a . The membranes are supported at edges $x = -L/2$ and $x = L/2$. In the present study, the effect of viscosity is not considered for the flow condition of high Reynolds number and low Mach number. An initial position of the inviscid vortex is (x_e, y_e) , where the y -coordinate depends on the length of blades as it is practically shed at the trailing edge. The strength of vortex is represented by the circulation Γ . A fan noise which is of dipole nature is modeled as a doublet which is located at the centre of the silencer. The doublet is a combination of a source and sink with same amplitude of strength μ_0 , which are separated with a small distance 2ε . The vortex motion is time-dependent which is associated with the effects of the mean flow U , membranes oscillation and doublet radiation. In the foregoing section, the instantaneous position of vortex is expressed as (x_v, y_v) .

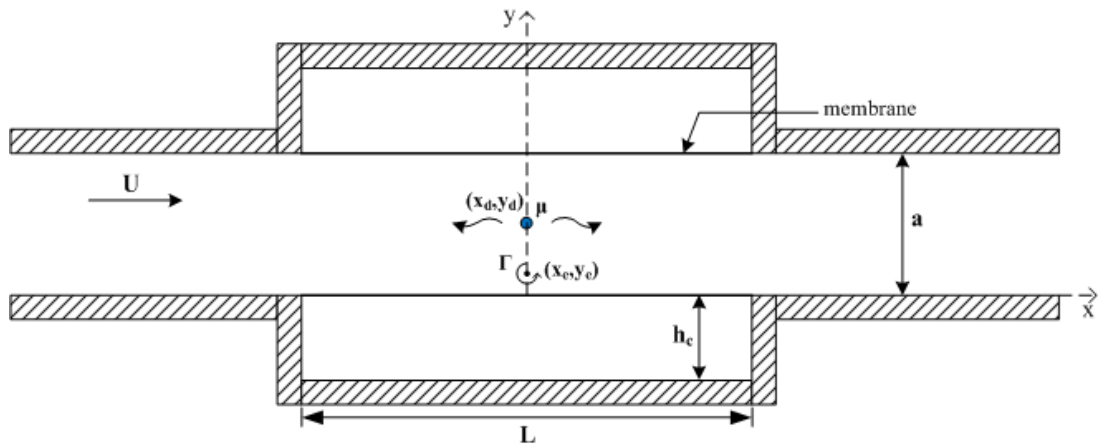


Figure 4.1 Two-dimensional schematic diagram of the membrane housing device in flow duct.

4.1.1. Vortex Dynamics and Membrane Vibrations

The sound radiation of the fan in dipole nature is modeled as a doublet inside a channel.

The complex potential of doublet, W_{dou} , at any position (x, y) by utilizing the potential theory (Currie, 2013), is expressed as

$$\begin{aligned}
 W_{dou}(x, y) = & (\mu / \pi) \log[(e^{\pi x/a} \cos(\pi y / a) - e^{\pi(x_d - \varepsilon)/a} \cos(\pi y_d / a)) \\
 & + i(e^{\pi x/a} \sin(\pi y / a) - e^{\pi(x_d - \varepsilon)/a} \sin(\pi y_d / a))] \\
 & / [(e^{\pi x/a} \cos(\pi y / a) - e^{\pi(x_d + \varepsilon)/a} \cos(\pi y_d / a)) \\
 & + i(e^{\pi x/a} \sin(\pi y / a) - e^{\pi(x_d + \varepsilon)/a} \sin(\pi y_d / a))]
 \end{aligned} \quad , \quad (4.1)$$

where μ is the rate of volume flow issuing outward (inward) from the source (sink) (Vallentine, 1959). It is expressed as a harmonic form, i.e. $\mu(\tau) = \mu_0 \cos(2\pi f\tau)$, (x_d, y_d) denotes the location of the doublet, τ is time and a is the height of duct. Note that the position of doublet is taken as the middle point between the source and the sink. The fluid velocity v_{dou} along the duct due to the influence of the doublet and its image is formulated as

$$\begin{aligned}
 v_{dou}(x, y) = \hat{x} \frac{\mu}{2a} & \left\{ e^{\pi(x_d - \varepsilon - x)/a} \left[\frac{\cos(\pi(y - y_d)/a) - e^{\pi(x_d - \varepsilon - x)/a}}{e^{2\pi(x_d - \varepsilon - x)/a} - 2e^{\pi(x_d - \varepsilon - x)/a} \cos(\pi(y - y_d)/a) + 1} \right. \right. \\
 & \left. \left. + \frac{\cos(\pi(y + y_d)/a) - e^{\pi(x_d - \varepsilon - x)/a}}{e^{2\pi(x_d - \varepsilon - x)/a} - 2e^{\pi(x_d - \varepsilon - x)/a} \cos(\pi(y + y_d)/a) + 1} \right] \right. \\
 & \left. - e^{\pi(x_d + \varepsilon - x)/a} \left[\frac{\cos(\pi(y - y_d)/a) - e^{\pi(x_d + \varepsilon - x)/a}}{e^{2\pi(x_d + \varepsilon - x)/a} - 2e^{\pi(x_d + \varepsilon - x)/a} \cos(\pi(y - y_d)/a) + 1} \right. \right. \\
 & \left. \left. + \frac{\cos(\pi(y + y_d)/a) - e^{\pi(x_d + \varepsilon - x)/a}}{e^{2\pi(x_d + \varepsilon - x)/a} - 2e^{\pi(x_d + \varepsilon - x)/a} \cos(\pi(y + y_d)/a) + 1} \right] \right\} \\
 & + \hat{y} \frac{\mu}{2a} \left\{ e^{\pi(x_d - \varepsilon - x)/a} \left[\frac{\sin(\pi(y - y_d)/a)}{e^{2\pi(x_d - \varepsilon - x)/a} - 2e^{\pi(x_d - \varepsilon - x)/a} \cos(\pi(y - y_d)/a) + 1} \right. \right. \\
 & \left. \left. + \frac{\sin(\pi(y + y_d)/a)}{e^{2\pi(x_d - \varepsilon - x)/a} - 2e^{\pi(x_d - \varepsilon - x)/a} \cos(\pi(y + y_d)/a) + 1} \right] \right. \\
 & \left. - e^{\pi(x_d + \varepsilon - x)/a} \left[\frac{\sin(\pi(y - y_d)/a)}{e^{2\pi(x_d + \varepsilon - x)/a} - 2e^{\pi(x_d + \varepsilon - x)/a} \cos(\pi(y - y_d)/a) + 1} \right. \right. \\
 & \left. \left. + \frac{\sin(\pi(y + y_d)/a)}{e^{2\pi(x_d + \varepsilon - x)/a} - 2e^{\pi(x_d + \varepsilon - x)/a} \cos(\pi(y + y_d)/a) + 1} \right] \right\} \quad , \quad (4.2)
 \end{aligned}$$

where \hat{x} and \hat{y} are the unit vector.

The membranes are initially at rest, it is then driven into motion due to the excitation by grazing mean flow, vortex acceleration and also the doublet radiation. For small membrane vibration magnitudes, the vibrating membranes are modeled as rigid boundaries with distributed fluctuating normal velocities (Tang, 2011). The complex potential, W_{mem} , at any position (x, y) inside a duct due to the flow induced by membranes vibration is

$$\begin{aligned}
 W_{mem}(x, y) = \frac{1}{\pi} & \left[\int_{-L/2}^{L/2} v_l(x') \log \left[\sinh \frac{\pi((x - x') + i(y - \eta_l))}{2a} \right] dx' \right. \\
 & \left. + \int_{-L/2}^{L/2} v_u(x') \log \left[\cosh \frac{\pi((x - x') + i(y - \eta_u))}{2a} \right] dx' \right] \quad , \quad (4.3)
 \end{aligned}$$

where x' represents the quantity along the membrane and η_u and η_l are the displacement of the upper and lower membranes respectively. The fluid velocity at any point (x, y) along the duct induced by the membrane vibrations can be estimated by the integration along the membranes,

$$v_{mem}(x, y) = \frac{\hat{x}}{2a} \left[\int_{-L/2}^{L/2} \frac{v_l(x') \sinh(\pi(x-x')/a)}{\cosh(\pi(x-x')/a) - \cos(\pi(y-\eta_l)/a)} dx' - \int_{-L/2}^{L/2} \frac{v_u(x') \sinh(\pi(x-x')/a)}{\cosh(\pi(x-x')/a) + \cos(\pi(y-\eta_u)/a)} dx' \right] + \frac{\hat{y}}{2a} \left[\int_{-L/2}^{L/2} \frac{v_l(x') \sin(\pi(y-\eta_l)/a)}{\cosh(\pi(x-x')/a) - \cos(\pi(y-\eta_l)/a)} dx' + \int_{-L/2}^{L/2} \frac{v_u(x') \sin(\pi(y-\eta_u)/a)}{\cosh(\pi(x-x')/a) + \cos(\pi(y-\eta_u)/a)} dx' \right], \quad (4.4)$$

The duct-side velocity on the upper and lower membranes are formulated as

$$v_u = \frac{\partial \eta_u}{\partial \tau} + U \frac{\partial \eta_u}{\partial x'} \quad \text{and} \quad v_l = \frac{\partial \eta_l}{\partial \tau} + U \frac{\partial \eta_l}{\partial x'}, \quad (4.5)$$

respectively, where U denotes the uniform flow speed.

When the blade starts its motion impulsively from $\tau=0$, there is a starting vortex with circulation $\Gamma(\tau)$ evolved at the sharp trailing edge of the blade. The growth of the vortex strength is determined by the Kutta condition. It is related to the chord-line of blade c , the angle of attack α , and also the uniform speed in the far-field U_∞ . The general expression of the circulation is $\Gamma(\tau)=2U\alpha(cU\tau)^{0.5}$. When $\tau \rightarrow \infty$, the limiting circulation would be $\Gamma_\infty=\pi c\alpha U_\infty$ stated by Saffman (1992). According to Brown and Michael (1954), the vortex velocity including its self-induced velocity is written as

$$v_{vortex} = \hat{x} \left[-\frac{x_v - x_e}{\Gamma} \frac{d\Gamma}{d\tau} + U + \frac{\Gamma}{4a} \cot \frac{\pi y_v}{a} \right] + \hat{y} \left[-\frac{y_v - y_e}{\Gamma} \frac{d\Gamma}{d\tau} \right] + v_{mem}(x_v, y_v) + v_{dou}(x_v, y_v). \quad (4.6)$$

The instantaneous vortex motion, harmonic radiation of doublet and mean flow give rise to fluctuating pressure loading on the two membranes. The response of membranes are governed by

$$\begin{aligned} m \frac{\partial^2 \eta_l}{\partial \tau^2} - T \frac{\partial^2 \eta_l}{\partial x^2} + D \frac{\partial \eta_l}{\partial \tau} + (p_{l,duct} - p_{l,cavity}) &= 0 \quad \text{and} \\ m \frac{\partial^2 \eta_u}{\partial \tau^2} - T \frac{\partial^2 \eta_u}{\partial x^2} + D \frac{\partial \eta_u}{\partial \tau} + (p_{u,cavity} - p_{u,duct}) &= 0 \end{aligned}, \quad (4.7)$$

where p is the fluid pressure and the subscript “duct” and “cavity” represent the meaning of the duct section and cavity section respectively. m is the mass density of the membrane, T is the tension applied on the membrane per unit length, D represents the damping coefficient.

The duct-side pressure loading which exists on the surface of membranes can be obtained by the linearized Bernoulli equations (Peake, 2004)

$$p_{l,duct} = -\rho_0 \left(\frac{\partial \phi}{\partial \tau} + U \frac{\partial \phi}{\partial x} \right) \Big|_{y=\eta_l} \quad \text{and} \quad p_{u,duct} = -\rho_0 \left(\frac{\partial \phi}{\partial \tau} + U \frac{\partial \phi}{\partial x} \right) \Big|_{y=\eta_u}, \quad (4.8)$$

where ρ_0 is the fluid density and ϕ is the velocity potential in the duct. The total incompressible velocity potential in near-field at any position (x, y) in the channel is generally written as

$$\begin{aligned}
 \phi(x, y, \tau) = & -\frac{\Gamma}{2\pi} \tan^{-1} \left[\frac{2 \sin(\pi y_v / a) (e^{\pi(x-x_v)/a} \cos(\pi y / a) - \cos(\pi y_v / a))}{(e^{\pi(x-x_v)/a} \cos(\pi y / a) - \cos(\pi y_v / a))^2 + (e^{\pi(x-x_v)/a} \sin(\pi y / a))^2 - (\sin(\pi y_v / a))^2} \right] \\
 & + \frac{1}{2\pi} \int_{-L/2}^{L/2} \left(\frac{\partial \eta_l}{\partial \tau} + U \frac{\partial \eta_l}{\partial x'} \right) \log \left[\cosh(\pi(x-x') / a) - \cos(\pi(y-\eta_l) / a) \right] dx' \\
 & - \frac{1}{2\pi} \int_{-L/2}^{L/2} \left(\frac{\partial \eta_u}{\partial \tau} + U \frac{\partial \eta_u}{\partial x'} \right) \log \left[\cosh(\pi(x-x') / a) + \cos(\pi(y-\eta_u) / a) \right] dx' \\
 & + \frac{\mu(\tau)}{4\pi} \log \left[\frac{e^{2\pi(x_d-\varepsilon-x)/a} - 2e^{\pi(x_d-\varepsilon-x)/a} \cos(\pi(y_d-y) / a) + 1}{e^{2\pi(x_d+\varepsilon-x)/a} - 2e^{\pi(x_d+\varepsilon-x)/a} \cos(\pi(y_d-y) / a) + 1} \right] \\
 & + \frac{\mu(\tau)}{4\pi} \log \left[\frac{e^{2\pi(x_d-\varepsilon-x)/a} - 2e^{\pi(x_d-\varepsilon-x)/a} \cos(\pi(y_d+y) / a) + 1}{e^{2\pi(x_d+\varepsilon-x)/a} - 2e^{\pi(x_d+\varepsilon-x)/a} \cos(\pi(y_d+y) / a) + 1} \right] + Ux + \gamma(\tau)
 \end{aligned} \tag{4.9}$$

where γ is a time function. The expression can be deduced by using the matched asymptotic expansion described in Sec. 4.1.2. On the right-hand-side of Eq. (4.9), the first term is the flow potentials induced by vortex and its images with the use of method of infinite images. The second and third terms describe the potentials corresponding to the membranes oscillations respectively. The contribution of radiations of doublet and its images is expressed as the fourth and fifth terms respectively.

The flexible membranes are backed by the cavity with the same length of the membrane as illustrated in Figure 4.1. It is a fully coupled membrane-cavity system. The vibration of flexible membrane induces acoustic pressure fluctuation inside the cavity. The pressure loading induced inside the cavity acts on the membrane and hence affects the membrane vibration. The pressure distribution in the cavity can be estimated by Finite Difference Time Domain (FDTD) method with the conservation of momentum and the continuity equation. The longitudinal and transverse particle velocities, denoted as v_x and v_y , are obtained by discretizing the governing equations. The two-dimensional basic formulations of FDTD are

$$v_x^{n+0.5}(i + \frac{1}{2}, j) = v_x^{n-0.5}(i + \frac{1}{2}, j) - \frac{\Delta\tau}{\rho_0\Delta x} [p_{cavity}^n(i+1, j) - p_{cavity}^n(i, j)] \quad \text{and} \quad (4.10)$$

$$v_y^{n+0.5}(i, j + \frac{1}{2}) = v_y^{n-0.5}(i, j + \frac{1}{2}) - \frac{\Delta\tau}{\rho_0\Delta y} [p_{cavity}^n(i, j+1) - p_{cavity}^n(i, j)], \quad (4.11)$$

where $\Delta\tau$ is the temporal step size, Δx and Δy are the spatial size for x - and y -direction respectively. The step sizes $\Delta\tau$, Δx and Δy must be chosen to satisfy the Courant stability criterion: $c_0\Delta\tau \leq (1/\Delta x + 1/\Delta y)^{-1/2}$ for two-dimensional case (Taflove and Brodwin, 1975). Integers n indicate the time instant, i and j denote the spatial points along x - and y -axis respectively. The approximations of acoustic pressure at any point inside the cavity p_{cavity} , are obtained by the discretized continuity equation which is expressed as

$$p_{cavity}^{n+1}(i, j) = p_{cavity}^n(i, j) - \frac{\rho_0 c_0^2 \Delta\tau}{\Delta x} [v_x^{n+0.5}(i + \frac{1}{2}, j) - v_x^{n+0.5}(i - \frac{1}{2}, j)] - \frac{\rho_0 c_0^2 \Delta\tau}{\Delta y} [v_y^{n+0.5}(i, j + \frac{1}{2}) - v_y^{n+0.5}(i, j - \frac{1}{2})], \quad (4.12)$$

where c_0 is the speed of sound. Apart from the oscillating flexible membrane, other three boundaries are rigid walls, which are treated as locally reacting surface, with frequency independent boundary conditions

$$\frac{\partial p_{cavity}}{\partial \tau} = -c_0 \xi_x \frac{\partial p_{cavity}}{\partial x}, \quad \text{for } x = -L/2 \text{ and } x = L/2$$

$$\frac{\partial p_{cavity}}{\partial \tau} = -c_0 \xi_y \frac{\partial p_{cavity}}{\partial y}, \quad \text{for } y = -h_c \text{ and } y = a + h_c \quad (4.13)$$

where ξ_x and ξ_y are the normalized impedance in x - and y -direction respectively. The pressure distribution inside the backed-cavity with different wall impedance can also be solved by modifying ξ_x and ξ_y (Kowalczyk and Van Walstijn, 2008). The

membranes are initially regarded as stationary. The vortex accelerates, circulation grows and membrane vibration starts with $\tau=0$. The movement of vortex and the motion of membrane vibration can be predicted by time integration of Eqs. (4.1) – (4.13) with the use of fourth order Runge-Kutta procedure. The motion of the vortex solved by the Runge-Kutta scheme can be written as

$$\begin{aligned} K_1 &= v_{vortex}(Z_\tau, \tau), & K_2 &= v_{vortex}(Z_\tau + K_1 \times \Delta\tau / 2, \tau + \Delta\tau / 2), \\ K_3 &= v_{vortex}(Z_\tau + K_2 \times \Delta\tau / 2, \tau + \Delta\tau / 2), & K_4 &= v_{vortex}(Z_\tau + K_3 \times \Delta\tau, \tau + \Delta\tau), \\ Z_{\tau+\Delta\tau} &= Z_\tau + \frac{\Delta\tau}{6}(K_1 + 2K_2 + 2K_3 + K_4) \end{aligned} \quad (4.14)$$

where $Z=(x_v, y_v)$.

4.1.2. Far-field Sound Radiation

The solution of far-field acoustic pressure radiation in duct can be found through the matched asymptotic expansion which matches the inner region incompressible near-field solution to the outer region of the plane wave solution. The far-field plane wave equation with steady mean flow of low Mach number is (Howe, 1998)

$$(1-M^2) \frac{\partial^2 \phi}{\partial x^2} - \frac{2M}{c_0} \frac{\partial^2 \phi}{\partial x \partial t} - \frac{1}{c_0^2} \frac{\partial^2 \phi}{\partial t^2} = 0, \quad (4.15)$$

where t is time in far-field and M is the Mach number, i.e. $M=U/c_0$. The general solution, Φ , after the time-Fourier transformation is

$$\Phi = A_- \exp[i\omega x / (c_0(1-M))] + A_+ \exp[-i\omega x / (c_0(1+M))], \quad (4.16)$$

where A_- and A_+ are the complex magnitude of upstream going wave and downstream going wave respectively and ω is the angular frequency. The downstream approximated velocity potential far from the device, i.e. $x \rightarrow +\infty$, from Eq. (4.9) is

$$\phi_{+\infty} \approx -\frac{\Gamma}{\pi} \left(\frac{\pi y_v}{a} \right) e^{-\pi x/a} + \frac{x}{2a} \int_{-L/2}^{L/2} \left(\frac{\partial \eta_l}{\partial \tau} - \frac{\partial \eta_u}{\partial \tau} \right) dx' + \frac{2\varepsilon\mu}{a} + Ux + \gamma . \quad (4.17)$$

Since all of the wave propagates towards the downstream without moving reversely back to the near-field, the magnitude of upstream going wave in Eq. (4.16) is zero, i.e. $A_-=0$. By the method of match asymptotic expansion, the asymptotic solution can be found for very low frequency, i.e. $\omega x/c_0 \rightarrow 0$, and very low Mach number, where $M \rightarrow 0$ (Sabina and Willis, 1975; Sabina and Babich, 2001). The leading order of the far-field solution suggests the sole function to be

$$\gamma(\tau) = \frac{c}{2a} \int_{-L/2}^{L/2} (\eta_u - \eta_l) dx' . \quad (4.18)$$

Thus, the complex magnitude A_+ can be obtained by applying Fourier transformation to the solution of fluid potential in far-field which is shown as

$$\phi_{far,+\infty} \approx -\frac{\Gamma y_v}{a} + \frac{2\varepsilon\mu}{a} + \frac{c}{2a} \int_{-L/2}^{L/2} (\eta_u - \eta_l) dx' . \quad (4.19)$$

The resultant acoustic pressure radiation far in downstream is

$$\begin{aligned} p_{+\infty} &= -\rho_0 \left(\frac{\partial \phi_{far,+\infty}}{\partial t} + U \frac{\partial \phi_{far,+\infty}}{\partial x} \right) \\ &= -\frac{\rho_0}{1+M} \left[-\frac{\partial}{\partial \tau} \left(\frac{\Gamma y_v}{a} \right) + \frac{2\varepsilon}{a} \frac{\partial \mu}{\partial \tau} + \frac{c_0}{2a} \int_{-L/2}^{L/2} \frac{\partial}{\partial \tau} (\eta_u - \eta_l) dx' \right] , \end{aligned} \quad (4.20)$$

which is evaluated at the retarded time $t-x/[c(1+M)]$. The first term in the bracket is the sound radiation induced by the evolution of vortex circulation and the vortex velocity. The second term is the acoustic pressure radiated by the doublet induced force acting on fluid. The sound wave generated by the volumetric flow excited by membranes vibration is expressed as the last term. Following similar procedures, as

there is no wave moving back toward the near field from upstream, i.e. $A_+ = 0$, the low frequency acoustic wave radiation in upstream is given as

$$\begin{aligned}
 p_{-\infty} &= -\rho_0 \left(\frac{\partial \phi_{far,-\infty}}{\partial t} + U \frac{\partial \phi_{far,-\infty}}{\partial x} \right) \\
 &= -\frac{\rho_0}{1-M} \left[\frac{\partial}{\partial \tau} \left(\frac{\Gamma y_v}{a} \right) - \frac{2\varepsilon}{a} \frac{\partial \mu}{\partial \tau} + \frac{c_0}{2a} \int_{-L/2}^{L/2} \frac{\partial}{\partial \tau} (\eta_u - \eta_l) dx' \right], \quad (4.21)
 \end{aligned}$$

with retarded time $t+x/[c(1-M)]$.

In the current study, the silencing performance of the membrane housing device is indicated by an insertion loss (IL) which is shown as

$$\text{IL} = 10 \log_{10} \frac{W_{original}}{W_{silenced}}, \quad (4.22)$$

where ‘‘original’’ refers to the unsilenced system and ‘‘silenced’’ refers to the silenced system with the membrane housing device. The acoustic power radiated, W , is obtained by integrating $p_{rms}^2/\rho_0 c_0$ over the cross section area of duct.

4.2. Numerical Results and Discussion

The fluid-structural interactions between the point vortex, membrane housing device and doublet, and the sound radiation mechanism are discussed in this section. All parameters are normalized by three basic quantities, i.e., duct height a^* , fluid density ρ_0^* and the maximum mean flow speed U_{max}^* chosen in the present study, for the numerical calculation. The uniform flow speed is restricted from zero to 50 m/s for the subsonic regime. The normalized total length of the membrane is $L = 2$. The dimensional mass density of the membrane m^* , the applied tension on the membrane per unit length T^* and the damping coefficient D^* are normalized by $a^* \rho_0^*$,

$a^*(U_{max}^*)^2\rho_0^*$ and $a^*U_{max}^*\rho_0^*$ respectively. A weak damping condition is adopted in the current study by setting $D^* = (\rho_0^*c_0^*a^*)$ since the effect of the damping coefficient is not considered (Frendi et al., 1994). The point vortex with circulation $\Gamma_\infty = 2.74 \times 10^{-3}$ which has been normalized by $a^*U_{max}^*$ is initially located at $x_e = 0$ and $y_e = 0.1$. For the doublet radiating with frequency f and strength $\mu = \mu_0 \cos(2\pi f\tau)$, it is fixed at (0, 0.5). The amplitude of the volume flow rate per unit length μ_0 has been normalized by $a^*U_{max}^*$. In order to satisfy the Courant stability condition, the time step $\Delta\tau$ is chosen as 0.001 and the spatial sizes of the cavity are $\Delta x = \Delta y = 0.02$ for the FDTD.

4.2.1. Fluid-structural Interactions

Figure 4.2 illustrates the effect of cavity depth of the membrane housing device h_c with the membrane of different mass density m on the vortex path in the duct at uniform flow speed $U = 0.2$. The doublet has the strength $\mu_0 = 6$ and frequency $f = 0.68$. The vortex initially started its motion at $x_v = 0$, $y_v = 0.1$. For the membrane of $m = 50$ and $T = 20$ as shown in Figure 4.2(a), the vortex path eventually bends upward with the increase of cavity height. When comparing with the cases of having deeper backing cavity, the upward motion of the vortex is less significant for the relatively shallow cavity $h_c = 0.5$ (solid lines). Moreover, after the upward bending motion, the vortex resumes close to its original height, i.e., $y_v = 0.1$, shortly for a shallower cavity such as $h_c = 0.5$. According to the findings shown by Tang (2011), the effect of membrane vibration on the vortex dynamics is significant since this system is a strongly vibro-acoustic coupled system. The compressibility of trapped air inside the cavity would change with the cavity depth, and hence, causes different membrane

motion (Dowell and Voss, 1963). The corresponding vibration of membrane will be discussed later with Figure 4.3.

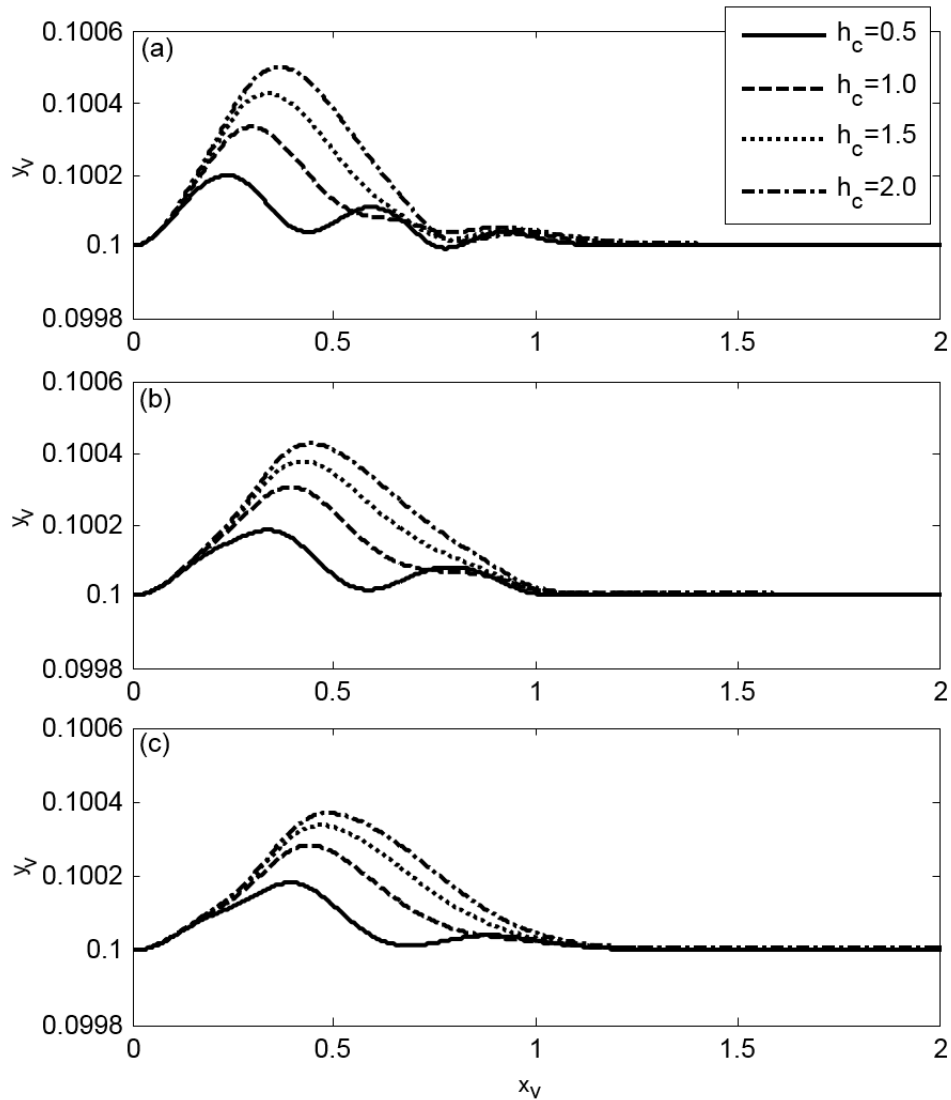


Figure 4.2 Effects of cavity height and mass density on the vortex trajectories. (a) $m = 50$; (b) $m = 100$; (c) $m = 150$.

Figures 4.2(b) and 4.2(c) illustrate that the similar trend of vortex trajectory can also be obtained with the increase of mass ratio of the membrane. However, it is observed that, for the membrane with heavier mass, the magnitude of maximum variation of the

vortex height slightly decreases. When comparing the results obtained for cavity depth $h_c = 2$ and mass density $m = 50$, the maximum deviation of vortex height is slightly reduced from 0.5% to 0.42% and 0.37% for $m = 100$ and $m = 150$ respectively. In addition, the whole vortex trajectory is shifted axially to the trailing edge of the membrane section with the increase of membrane mass density.

The vortex dynamics shown in Figure 4.2 is strongly influenced by the membrane oscillations. The corresponding displacement and transverse velocity along the lower membrane for the membrane housing device with $h_c = 0.5$ (solid line) and $h_c = 1.0$ (dashed line) at three different time instants are described in Figure 4.3 in order to explain the vortex movement illustrated in Figure 4.2(a). The longitudinal position of the vortex at the corresponding time is marked by circle and cross for the results of $h_c = 0.5$ and $h_c = 1.0$ respectively. Figures 4.3(1a) and 4.3(2a) show the displacement and the transverse velocity along the lower membrane respectively at the beginning $\tau=0.498$. It illustrates that the membrane vibration is of the same phase along the membrane for different cavity heights. The vibrating velocity of the membrane is slightly higher for the cavity with larger cavity depth. At $\tau=1.239$, the vortex reaches the peak position for the case with $h_c = 1.0$ which is consistent with the membrane motion as shown in Figures 4.3(1b) and 4.3(2b). For the shallower cavity $h_c=0.5$, the vortex height and the transverse velocity of the vortex is lower due to the weak response of the membrane covered by the shallow cavity. However, the vortex height for a deeper cavity is not always higher than that of the shallow cavity. At $\tau = 2.971$, the corresponding vortex height at the longitudinal position $x = 0.6$ is relatively higher for $h_c = 0.5$ when comparing with that obtained at $h_c = 1.0$. As shown in Figure 4.3(1c), when the vortex flies over the membrane at $x=0.6$, the upward displacement of the

membrane is larger for $h_c=0.5$. As a result, a higher vortex height is achieved. The results indicate that the vortex motion greatly depends on the phases of the membrane vibration at the corresponding time instant that the vortex flies over the membrane.

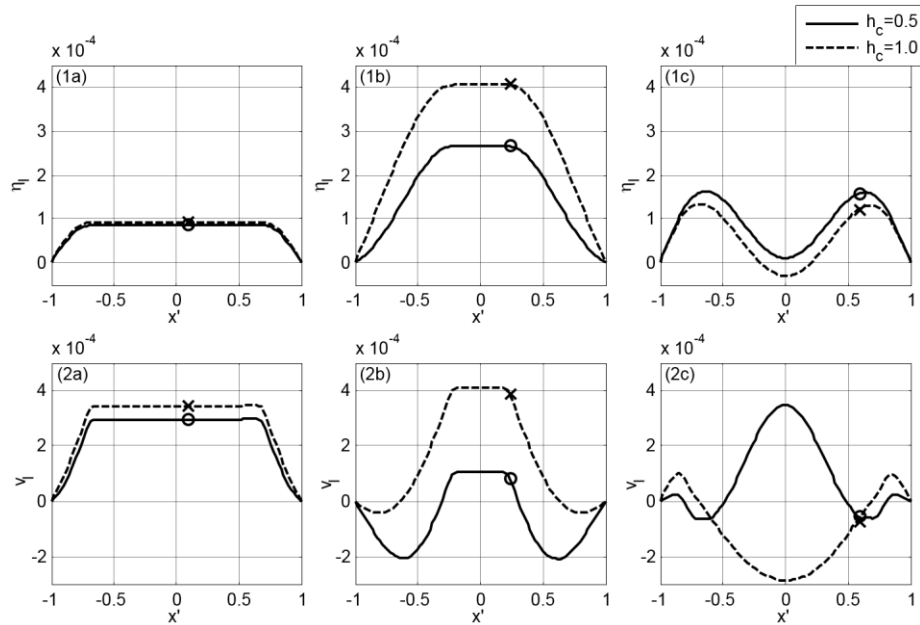


Figure 4.3 Vibration of lower membrane. The first row represents the variation of displacement while the second row represents the velocity at (a) $\tau=0.498$; (b) $\tau=1.239$; (c) $\tau=2.971$.

Figures 4.4(1a) to 4.4(1c) show the first (solid line), second (dotted line) and third (dashed line) modal response of the lower membrane which is obtained by solving the motion equation shown in Eq. (4.7) with mass density $m=50$, $m=100$ and $m=150$ against time respectively. The result indicates that the membrane vibration is dominant at odd modes while the response of second mode is insignificant. Similar observations can be obtained for the membranes with different mass densities. Figures 4.4(2a) to 4.4(2c) show the time history of the vibration displacement of lower membrane for $m=50$, $m=100$ and $m=150$ respectively. It is found that the maximum amplitude of the membrane displacement for different mass density is nearly the same.

However, the oscillating frequency of the membrane is reduced with the increase of membrane mass since the *in-vacuo* wave speed of the membrane, $c_T=(T/m)^{0.5}$, is lower for a heavier membrane. The dashed lines shown on the contour in Figures 4.4(2a) to 4.4(2c) denote the longitudinal position of the vortex x_e at the corresponding time. The maximum amplitude of displacement is always achieved at the center of the membrane $x' = 0$ since the odd vibration modes are dominant. Since the point vortex is initially located at $x_e = 0$ which is the centre of the membrane, it has a higher chance to gain a larger transverse velocity caused by membrane vibration if the membrane could reach its vibration amplitude within a shorter time before the vortex is swept to the downstream of the silencer due to the mean flow.

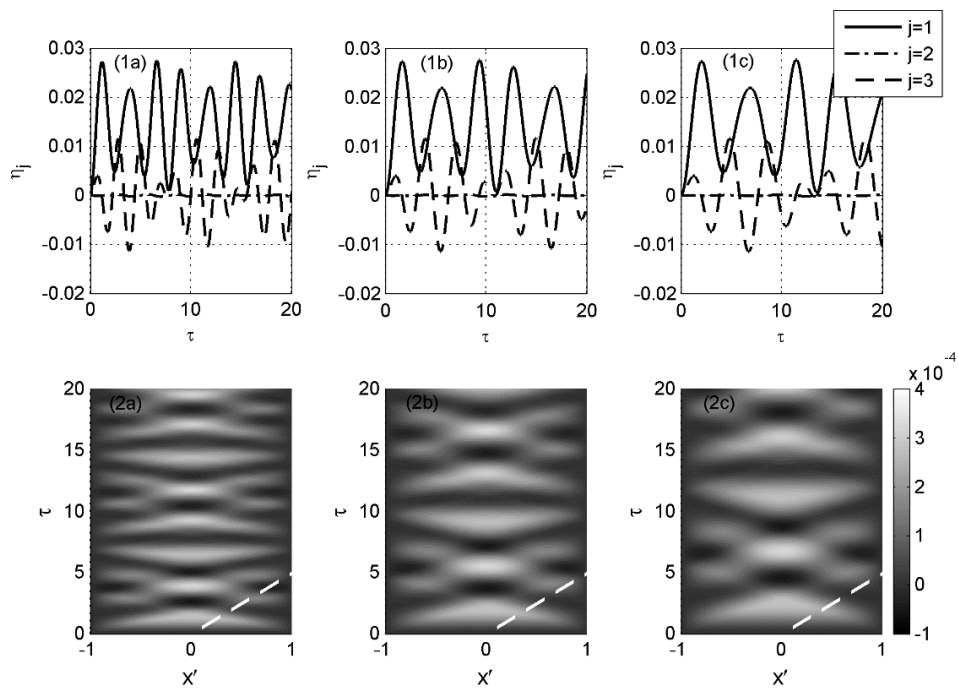


Figure 4.4 Vibration displacement of lower membrane for $h_c=0.5$. The first row represents the modal magnitude while the second row represents the time variation of vibration displacement of lower membrane of (a) $m=50$; (b) $m=100$; (c) $m=150$.

For the fan blade with a shorter chord length, the vortex shed at a higher initial height. The relationship between the relative transverse position of the vortex and the initial position of the vortex is shown in Figure 4.5. The membrane housing device of $m = 100$, $T = 20$ and $h_c = 0.8$ at uniform flow speed $U = 0.1$ is considered. For the flow duct system without doublet, the vortex transverse velocity is weakened with an increase of the initial height of the vortex due to the pressure-releasing effect of upper membrane oscillation. For the fan-ducted system with doublet, the vortex movement is not only affected by the membrane vibration, but also influenced by the doublet. The variation of the vortex height increases with the strength of the doublet as shown in Figure 4.5. The numerical results for doublet strength $\mu_0 = 3$, $\mu_0 = 6$ and $\mu_0 = 9$ with frequency $f = 0.68$ are shown as Figures 4.5(a), 4.5(b) and 4.5(c) respectively. Moreover, a significant periodic fluctuation of the variation of vortex height can be seen with the increase of vortex initial height. It suggests that the effect of the doublet radiation on the vortex motion becomes more significant when initial vortex height is higher. When the vortex continuously propagates towards the trailing edge of the membrane, the interaction between the doublet and vortex vanishes.

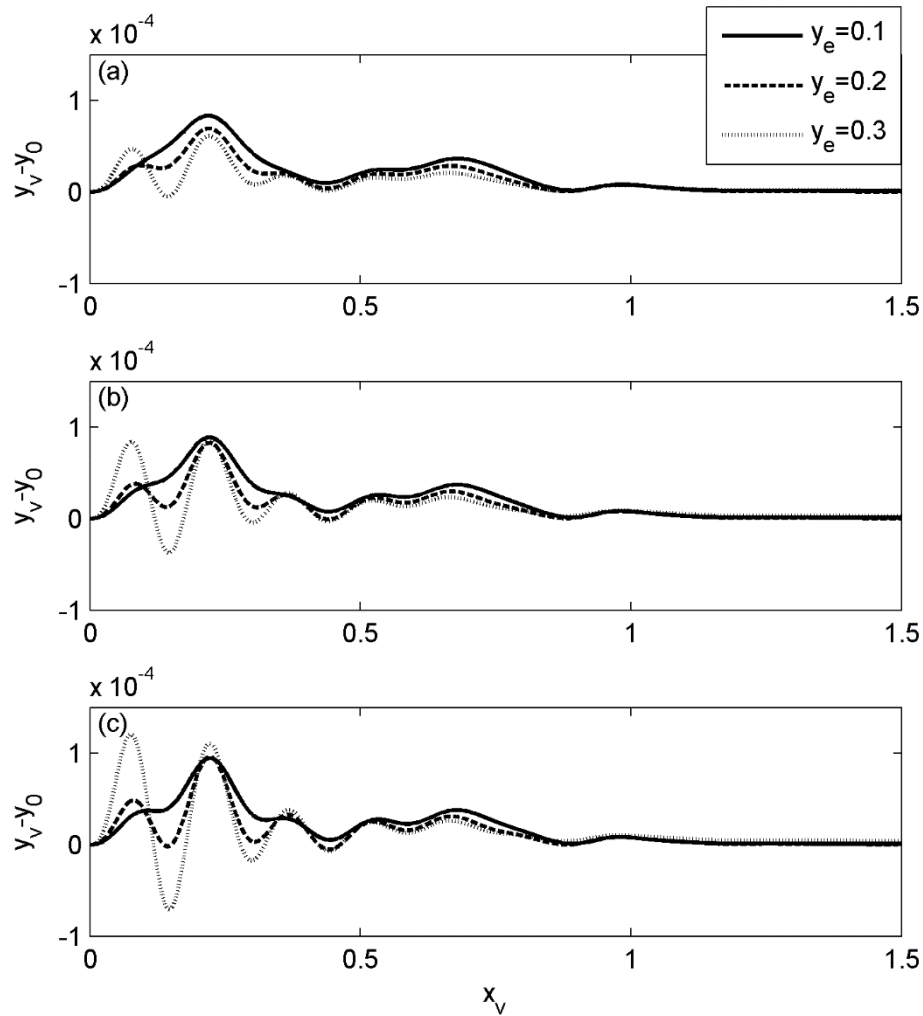


Figure 4.5 Effect of doublet strength and initial vortex height on the vortex dynamics for $h_c = 0.8$. (a) $\mu_0 = 3$; (b) $\mu_0 = 6$; (c) $\mu_0 = 9$.

4.2.2. Far-field Acoustic Pressure Radiation

In this section, the acoustic pressure radiated from each noise source in this system is studied. For the point vortex with $\Gamma_\infty = 0.00274$, the noise induced by the vortex movement is only about one tenth of the total sound pressure radiation, which is much smaller than that radiated by the doublet and the membrane. Thus, the corresponding acoustic contribution from the inviscid vortex is not considered here. The far-field acoustic pressure generated by the membrane vibration and doublet radiation is

examined with different mean flow speed as shown in Figure 4.6. The far-field sound pressure radiations of the doublet and membrane formulated as the last two terms of Eq. (4.20) are expressed as root mean square value. The numerical results are predicted with four different cavity depths $h_c = 0.5$ (\circ), 0.6 (\times), 0.7 (\square) and 0.8 ($+$) for the case of $m=100$, $T=20$, $f=0.68$ and $\mu_0=6$. Figure 4.6 indicates that a stronger sound radiation can be obtained with the increase of mean flow speed. According to Eq. (4.20), the source strength of the acoustic radiation changes with the flow speeds by the term $U\partial\phi_{far,+\infty}/\partial x$. Also, the acoustic-structural coupling is more significant at higher flow speed as illustrated by Sucheendran *et al.* (2013). Therefore, the acoustic response of the membrane vibration increases with Mach number.

The effect of the cavity depth on the sound radiation induced by the membrane vibration can be classified into three regions with respect to the Mach number: region I is the zone with very small Mach number with $0.006 < M < 0.013$; region II is the intermediate zone for $0.013 \leq M \leq 0.018$; region III is the zone with $M > 0.018$. In region I with small Mach number, the root mean square value of the sound pressure induced by the membrane, $p_{rms,m}$, is relatively small compared to a doublet, $p_{rms,d}$, i.e., $p_{rms,m} < p_{rms,d}$. The effect of cavity depth on the sound radiation slightly increases with the Mach number. The effect of cavity depth on the amplitude of sound pressure is not significant in region I since the excitation on the membrane induced by the mean flow is small and the induced pressure loading inside the cavity is relatively small as well. When the Mach number is increased to that of region II, the sound generated by the membrane is comparable with that generated by the fluid force from the doublet, i.e., $p_{rms,m} \approx p_{rms,d}$. In this intermediate range, the influence of cavity height on the sound pressure radiation from the membrane becomes more crucial. When the depth of

cavity increases from $h_c=0.5$ to 0.8 at $M=0.01324$, more than 41% sound radiation enhancement is found. When the Mach number is further increased reaching region III, the acoustic pressure generated due to membrane vibration would be comparatively much larger than that of doublet, i.e., $p_{rms,m} > p_{rms,d}$. In this region, sound would be amplified even for different designs of backed-cavity due to the vigorous vibration of membrane. Therefore, a better silencing performance could be achieved in region I and II at low Mach numbers. The noise attenuation mechanism with different design of the silencing device would be discussed in Sec. 4.2.3.

The relationship between the uniform flow speed U and maximum value of total sound power W_{max} radiated to the downstream of the duct is described in Figure 4.6(b). Following the findings observed in Figure 4.6(a), the acoustic power radiation is higher for the cavity with larger depth h_c at any mean flow speed. The maximum of sound power W_{max} increases with the mean flow speed U nonlinearly. The maximum sound power can be expressed as the function of the grazing flow speed by a quadratic function in a normalized form

$$W_{\max} = (834.5U^2 - 92.28U + 3.848) \times 10^{-9} , \quad (4.23)$$

for the case $m=100$, $T=20$, $f=0.68$ and $\mu_0=6$.

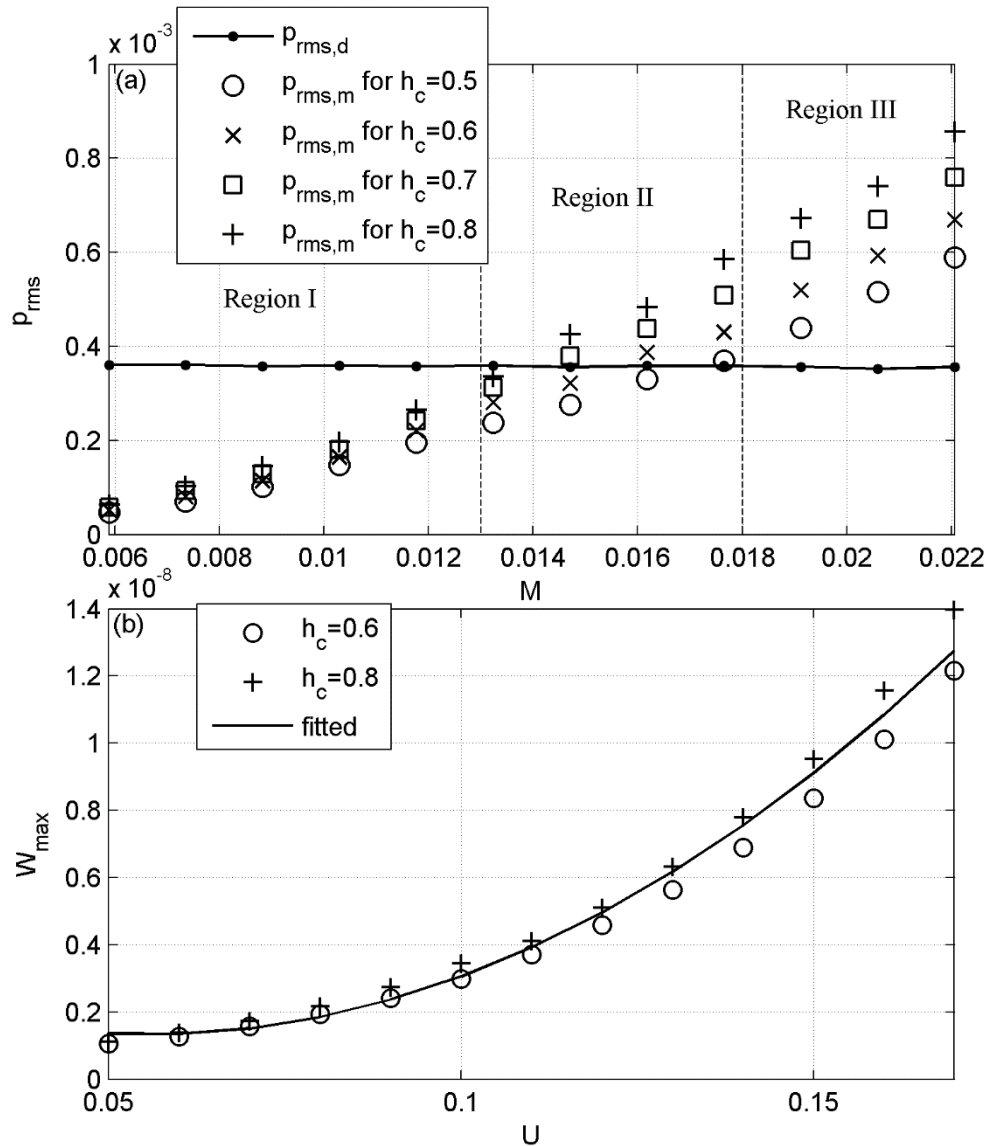


Figure 4.6 Effect of mean flow speed on the sound radiation. (a) Root mean square value of acoustic pressure radiation; (b) Maximum sound power radiation.

4.2.3. Noise Attenuation Mechanism

The dipole noise in the flow duct can be suppressed by the proposed membrane housing device based on the sound cancellation mechanism. The membranes flush-mounted on the duct would be driven into vibration due to the doublet and flow excitation to generate sound. The sound pressure radiated by the membrane is then

superimposed with the aerodynamic noise and the dipole sound. The performance of such a device depends on two aspects, which are the amplitude difference and phase difference between the sound radiation generated by membrane vibration and the dipole sound. The effects of different design parameters, including the geometric feature specified as the cavity depth h_c and also the mechanical properties of the flexible membrane noticed as the mass density m and the applied tension T , on the performance of the silencing device are investigated and discussed briefly in the following paragraphs. The numerical results are obtained with three different mean flow speed, which are $U = 0.05, 0.1$ and 0.2 respectively.

Figure 4.7 shows the time-varying far-field sound pressure radiation by the doublet p_{dou} (dotted line), and that induced by the membrane vibration p_{mem} for three different cavity heights, $h_c = 0.4$ (solid line), 0.6 (dashed line) and 0.8 (dash-dot line) respectively with $f = 0.34$, $\mu_0 = 8$, $m = 90$ and $T = 40$. For the amplitude of acoustic pressure, it is observed that amplitude of sound radiated by the membrane oscillation increases with the height of backing cavity, which has been explained in Sec. 4.2.2. For the frequency of sound pressure radiation, Figure 4.7(a) indicates that the oscillation frequency of acoustic pressure radiation from the membrane is higher for a shallower cavity since the cavity stiffness is more significant for the case with smaller cavity depth. The same observation could be found for higher mean flow speed, i.e. $U = 0.1$ and 0.2 as illustrated in Figures 4.7(b) and 4.7(c) respectively. As shown by Figures 4.7(a) and 4.7(b), at $\tau \leq 10$, the phase difference between p_{mem} and p_{dou} is small for $h_c = 0.6$. In this situation, the membrane housing device is unable to attenuate the dipole noise, but reversely enhances the sound radiation of the system due to the occurrence of constructive interference. However, if the cavity is replaced

by a shallower alternative $h_c = 0.4$, the membrane respond in a higher frequency such that ~ 180 degree phase difference between the sound radiated by membrane and doublet is achieved. As a result, a better silencing performance can be achieved and some of the noise from doublet could be cancelled due to the anti-phase sound radiation of the membrane.

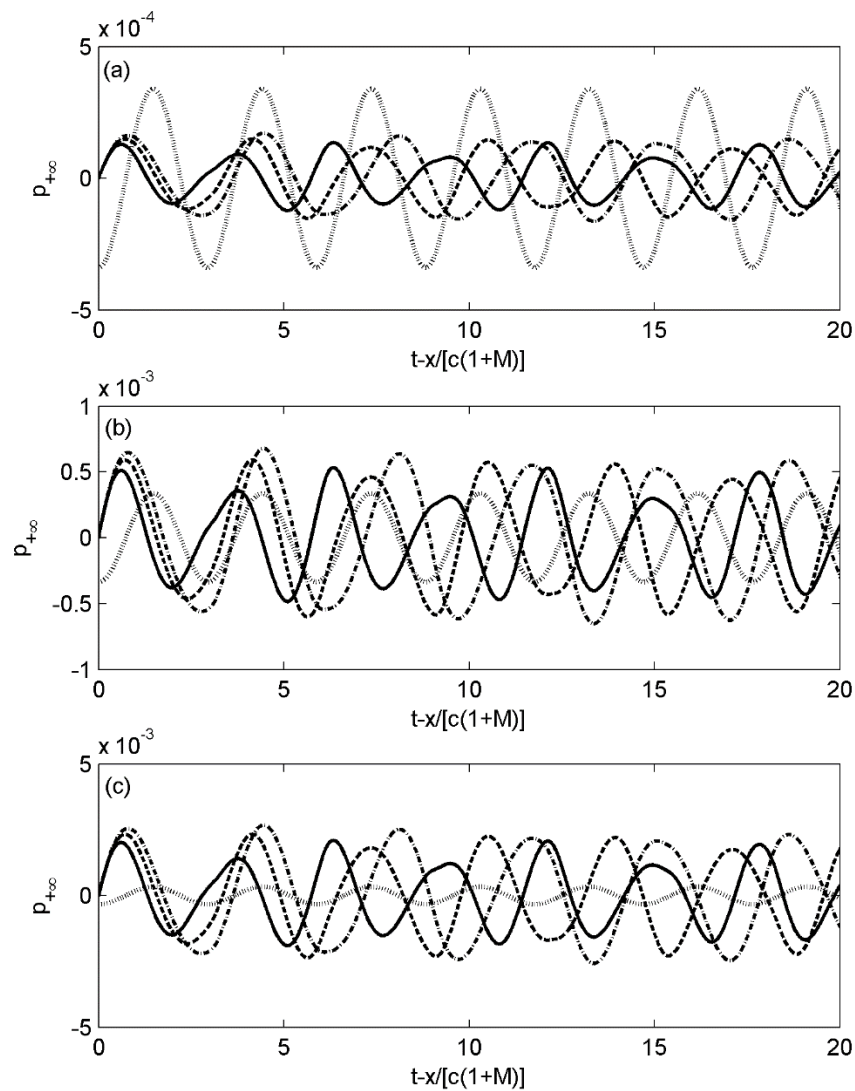


Figure 4.7 Effect of cavity height on the sound radiation of membrane. (a) $U = 0.05$; (b) $U = 0.1$; (c) $U = 0.2$. (---) p_{dou} ; (—) p_{mem} for $h_c = 0.4$; (---) p_{mem} for $h_c = 0.6$; (-·-) p_{mem} for $h_c = 0.8$.

Figure 4.8 shows the mass effect of the membrane on the sound pressure radiation for cavity height $h_c = 0.7$, $T = 40$ and three different mass ratio, i.e. $m = 80$ (solid line), 100 (dashed line) and 120 (dash-dot line). At high grazing flow speed, i.e., $U = 0.2$, the acoustic pressure generated by membrane vibration would be too high to suppress the noise from doublet. From Figure 4.8(c), the root-mean-square value of the sound pressure radiated by the doublet $p_{rms,d}$ is only 17.1% of that induced by the membrane vibration $p_{rms,m}$ when $m = 120$. Figure 4.8 suggests that the amplitude of p_{mem} , can be adjusted to a lower level by using the membrane with higher mass. The reduction in the amplitude of p_{mem} is achieved as a heavier membrane has a greater inertia and hence it requires a greater loading to drive a heavier membrane into vibration. Moreover, for the frequency of sound radiation, the frequency of p_{mem} is reduced by increasing the mass of membrane due to the reduction of wave speed c_T .

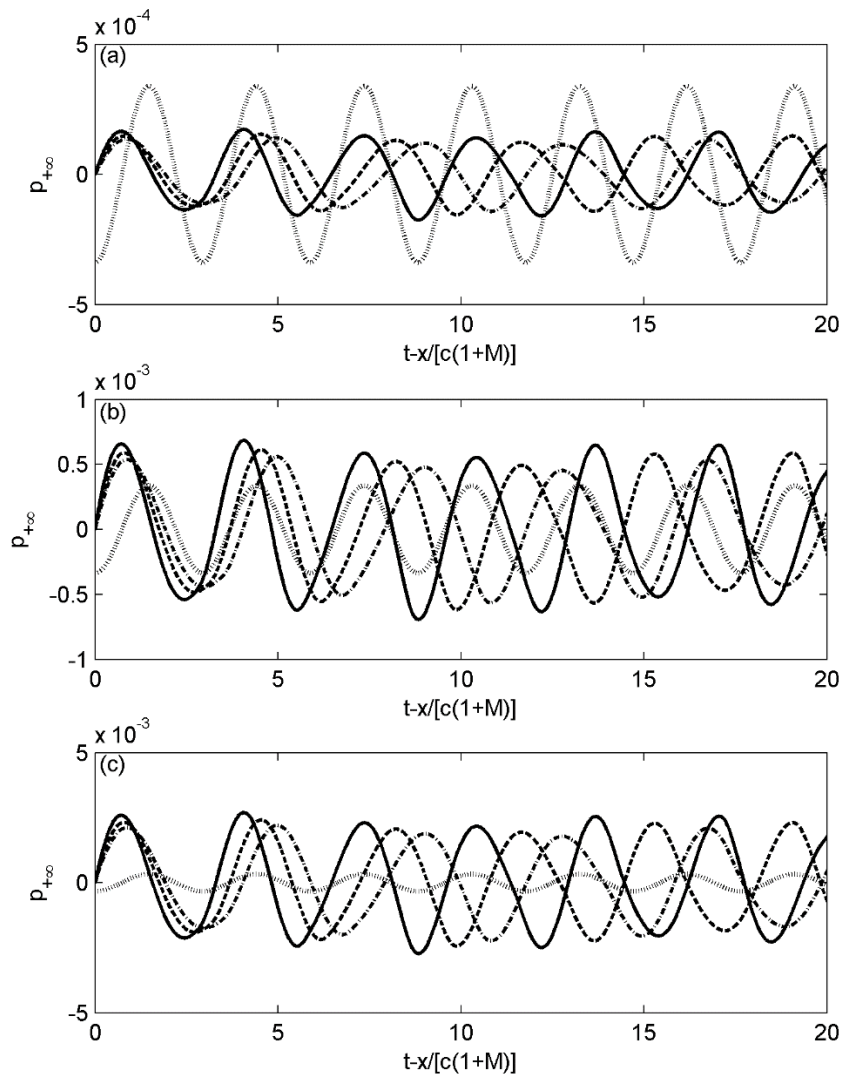


Figure 4.8 Effect of mass ratio on the sound radiation of membrane. (a) $U = 0.05$; (b) $U = 0.1$; (c) $U = 0.2$. (---) p_{dou} ; (—) p_{mem} for $m = 80$; (---) p_{mem} for $m = 100$; (-.-) p_{mem} for $m = 120$.

On the other hand, the wave speed c_T also depends on the tension applied on the membrane. A higher wave speed can be obtained for the membrane with higher tension, and thus a higher frequency of sound radiation from the membrane is achieved as shown in Figure 4.9 for $f = 0.34$ and strength $\mu_0 = 8$. Figures. 4.9 shows that sound radiated by the membrane with $T = 60$ nearly in the same phase as that of

the doublet. Thus two sound waves superimpose together and result in a larger total acoustic pressure radiation. However, if membranes with smaller tension are adopted, i.e., $T = 20$ (solid line), the frequency of sound induced by membrane vibration is lower. In this case, the phase difference between p_{mem} and p_{dou} is close to 180° . As a result, the doublet noise can be canceled by the sound radiated by the membrane.

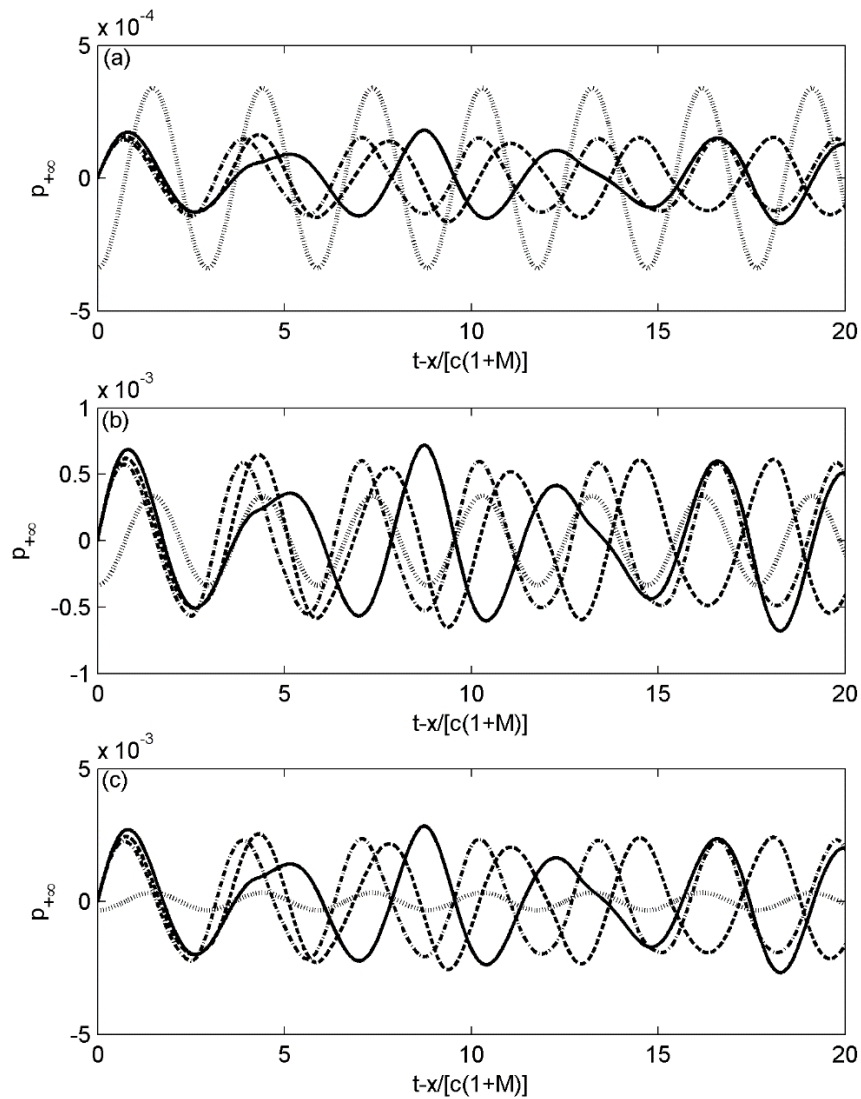


Figure 4.9 Effect of tension on the sound radiation ($\mu_0 = 8$, $f = 0.34$, $h_c = 0.7$, $m = 90$). (a) $U = 0.05$; (b) $U = 0.1$; (c) $U = 0.2$. (---) p_{dou} ; (—) p_{mem} for $T = 20$; (---) p_{mem} for $T = 40$; (-·-) p_{mem} for $T = 60$.

The performance of the silencer can be described by insertion loss (IL) which is formulated as Eq. (4.22). Figure 4.10(a) shows the insertion loss achieved by the silencer with different wave speeds c_T , which is a function of mass ratio and tension of the membrane. The depth of the backing cavity is kept as $h_c = 0.7$. The doublet noise to be controlled with $\mu_0 = 8$ is investigated with three different frequencies $f = 0.14$ (\square), 0.24 (\circ) and 0.34 (\times). The uniform flow speed in the duct is $U = 0.05$. The negative IL found in Figure 4.10(a) indicates that the silencing performance of the membrane housing device with the wave speed of membrane ranged from $c_T = 0.471$ to 0.817 is poor in order to control the doublet noise at $f = 0.14$ or 0.34 . However, at $f = 0.24$, a positive IL can be achieved by the silencer for c_T smaller than 0.633 . Figures 4.10(b) and 4.10(c) show the far-field acoustic pressure radiation attributed to the vortex motion (dotted line), doublet radiation (dashed line) and the membrane vibration (dash-dot line) for $c_T = 0.577$ and 0.471 respectively. For the membrane with $c_T = 0.471$ and $c_T = 0.577$, the IL obtained for controlling the doublet noise with $f = 0.24$ are 6.483 dB and 4.339 dB respectively. The total acoustic pressure radiation in downstream $p_{+\infty}$ by summing up all the components is indicated by the solid line. As shown in Figure 4.10(b), for $c_T = 0.577$, the amplitude of the total acoustic pressure radiation, $p_{+\infty}$ is close to that of the doublet component p_{dou} at the beginning. When time passes, sound cancellation achieved by the membrane housing device is observed. The total acoustic pressure $p_{+\infty}$ becomes smaller than p_{dou} since the membrane radiated pressure p_{mem} is anti-phase to p_{dou} such that it cancels part of the doublet noise due to the destructive interference. The same sound cancellation process can also be found in Figure 4.10(c) with different physical properties of the membrane, i.e. $c_T = 0.471$.

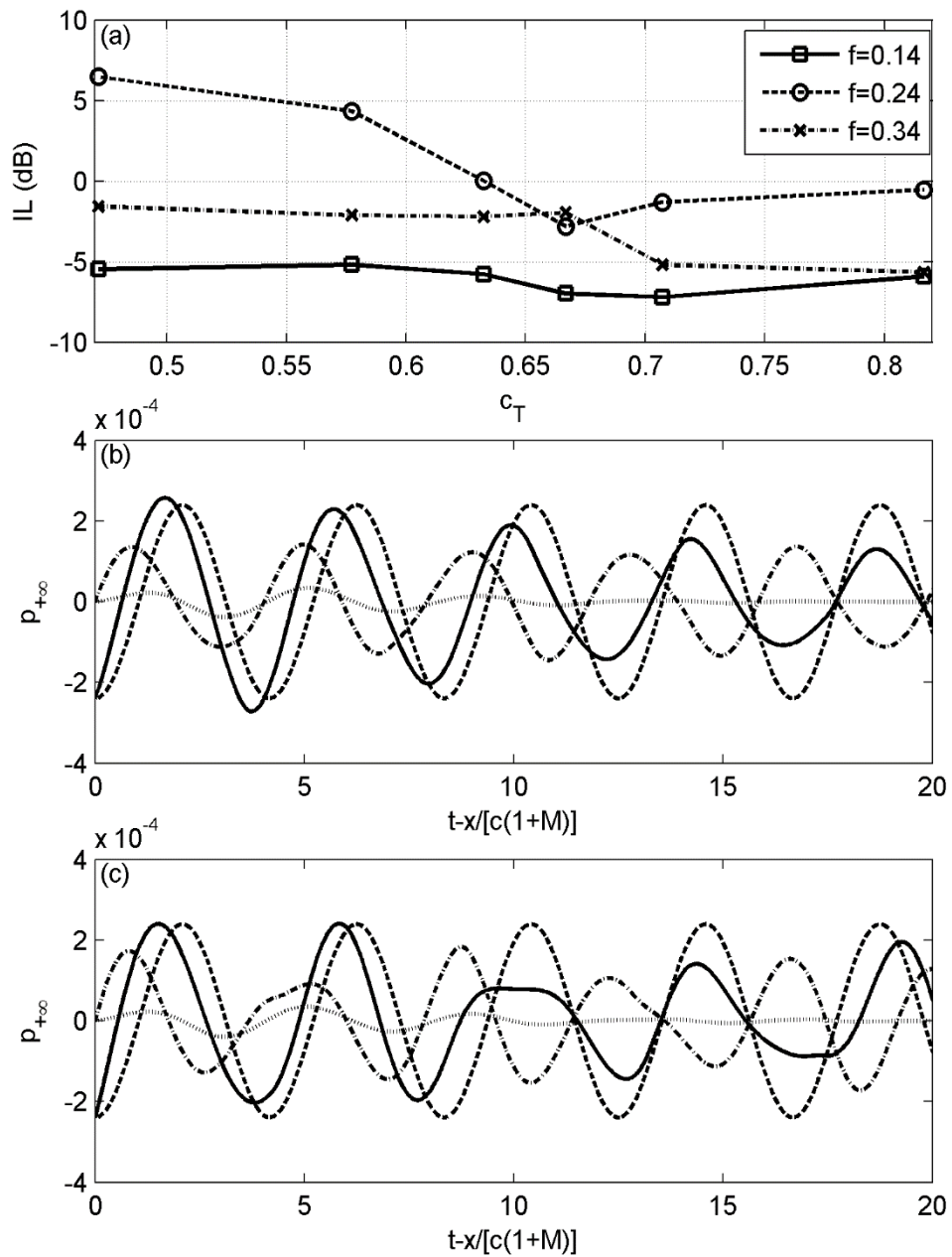


Figure 4.10 Silencing performance of proposed membrane housing device. (a) Spectrum of inserting loss (IL). (b) and (c) are the components of sound pressure radiation for $c_T = 0.577$ and $c_T = 0.471$ respectively. (—) Total sound pressure radiation; (---) Pressure radiated by vortex; (-·-) Pressure radiated by membrane oscillation; (-·-) Pressure radiated by doublet.

4.3. Conclusions

In this chapter, a two-dimensional theoretical model is developed in order to investigate the fluid-structural-acoustic interaction and the acoustic radiation mechanism of the membrane housing device in a flow duct. Based on the potential theory, the time-varying vortex motion and membrane vibration can be obtained. Also, the far-field sound radiation and the performance of the membrane housing device is predicted by adopting the matched asymptotic expansion technique. The following conclusions are made:

- 1) The vortex motion depends on the membrane vibration and the doublet radiation. The effect of the doublet fluctuation on the vortex movement becomes significant if the vortex is initially shed at a higher position, which means closer to the doublet. The cavity depth would also affect the vortex trajectory by changing the membrane vibration.
- 2) The vortex motion, membrane vibration and the doublet radiation are three major sound sources in the system. The sound power radiated due to the membrane oscillation increases with the uniform flow speed nonlinearly. A better silencing performance can be achieved at the intermediate range of flow speed ($0.013 \leq M \leq 0.018$) since the difference of the sound pressure amplitude radiated from the membrane and doublet is small.
- 3) The dipole noise in the flow duct can be attenuated by the membrane housing device based on the sound cancellation mechanism. The silencing performance of such device depends on two aspects, which are the amplitude and phase difference between the sound generated by the membrane oscillation and doublet

radiation. About 6 dB insertion loss can be achieved by the proposed membrane housing device.

Chapter Five

Conclusions and Recommendations

This research study is focused on the fluid-acoustic-structural interaction and the acoustic behaviors of the silencing device with flexible structures in the fan-ducted system in low Mach numbers. Two types of flow effects which would influence the acoustic performance of the silencing device have been investigated. . One is the effect of vortex evolution which directly changes the acoustic properties of the device. Another one is the effect of the existing vortex that changes the structural vibration of the device due to the additional loading given by the presence of vortex. The summarized conclusions for the present research and the recommendations for future work are given in this chapter.

5.1. Conclusions

The features and absorption mechanism of the micro-perforated panel absorber array subjected to the effect of orifice nonlinearity under normal incidence have been studied. When the MPP is exposed to the environment at high sound pressure, the acoustic properties of the MPP are totally different from that in the linear regime due to the jet formation at the exit of orifice. It is shown that the absorption performance and the acoustic impedance of the MPP absorber are highly dependent on the acoustic excitation level. In order to investigate the effect of the acoustic nonlinearity of orifice on the acoustic behavior of the micro-perforated panel absorber array, the two-

dimensional theoretical and finite element models have been established. By comparing the performance of the MPP absorber array between the linear and nonlinear regimes, it is found that the negative mass effect induced by the vortex formation broadens the half-absorption bandwidth of the MPP absorber array. In addition, the absorption coefficient of the MPP absorber array is improved to a higher level due to the increase of acoustic resistance. With the further increase of the incidence sound pressure level, the MPP absorber array behaves like the single MPP absorber due to the added mass effect given by the neighboring sub-cavity. With the effect of the panel vibration, the dramatic drops on the absorption curve is found due to the sound reflection induced by the structural resonance. The parametric study on the MPP absorber array with and without the effect of structural vibration has been carried out to provide basic information for the MPP absorber design. The proposed finite element model of the MPP absorber array subject to the orifice nonlinearity feature is validated by experiment. The measured absorption coefficient of the MPP absorber array matches well with the numerical result. The half-absorption bandwidth of the MPP absorber array with $t = 0.4\text{mm}$, $d = 0.65\text{mm}$ and $\sigma = 1.76\%$ can reach to 4.18 at $\text{SPL} = 110\text{dB}$.

Moreover, the influence of the orifice nonlinear feature on the silencing performance of the vibro-acoustic coupled micro-perforated panel silencer has been studied under grazing plane wave incidence. A finite element model has been developed to study the noise attenuation mechanism of the micro-perforated panel silencer at moderate intensity sound. The duct noise reduction can be achieved by the MPP silencer due to the combination of sound reflection induced by panel oscillation and acoustic absorption given by the perforations. The contributions of these two noise suppression

mechanisms vary at different frequencies. At the frequency range in which sound absorption is dominant, an improvement on the silencing performance of such silencing device is obtained in the nonlinear regime due to the additional absorption given by the effect of orifice nonlinearity. The parametric study of the MPP silencer is also conducted with different structural properties of the panel, i.e. surface density M_s and bending stiffness B , and also with different parameters of the MPP, including the length of panel L and the panel thickness t_{mpp} . With the supplementary sound absorption provided by the nonlinearity feature of the orifice, the second and third stopbands with narrow bandwidth obtained in the linear regime are widened with the increase of the incidence sound pressure level.

In addition, the mechanism of the fluid-acoustic-structural interaction of the membrane housing device in a fan-ducted system has been investigated. The membrane housing device is used to control the fan noise directly at the source position. The dominant noise generated by the fan is a dipole. Turbulence flow is induced during the fan operation. In order to investigate the complicated fluid-acoustic-structural interactions and the noise attenuation mechanism of the membrane housing device in the present of unsteady flow, a simplified theoretical aeroacoustic model of the membrane housing device has been established. The time-varying vortex motion and membrane vibration have been predicted based on the potential theory. It is found that the vortex dynamics depends on the membrane vibration and the doublet radiation. The effect of the doublet fluctuation on the vortex movement becomes significant if the vortex is initially shed at a higher position, which means closer to the doublet. The cavity depth would also affect the vortex trajectory by changing the membrane vibration. The far-field sound radiation and the performance of the

membrane housing device have been also examined by using the matched asymptotic expansion technique. The vortex motion, membrane vibration and the doublet radiation are three major sound sources in the system. It is found that the sound power radiated due to the membrane oscillation increases with the uniform flow speed nonlinearly. The dipole noise in the flow duct can be attenuated by the membrane housing device based on the sound cancellation mechanism. The silencing performance of such a device depends on two aspects, which are the amplitude and phases difference between the sound generated by the membrane oscillation and doublet radiation. About 6 dB insertion loss can be achieved by the proposed membrane housing device.

5.2. Recommendations for Future Development

The main work of this thesis is summarized in the previous section. It focuses on the fluid-acoustic-structural interaction of the silencing device with flexible boundary in fan-ducted system. Moreover, the flow effect on the noise attenuation mechanism of the devices has been investigated extensively. Based on the work of the present study, future study can be carried out to increase the understanding of the sound radiation mechanism of the system subjected to the interactions between flow and flexible structure.

- 1) The current work shows that the acoustic behavior of the MPP silencer is related to the incidence sound excitation. An improved silencing performance can be achieved by the MPP silencer due to the supplementary sound absorption provided by the nonlinear acoustic properties of the perforations. The study is only done

with the numerical model. A theoretical study is expected in order to give a deeper physical understanding of the sound attenuation mechanism of the MPP silencing subjected to the orifice nonlinearity under grazing incidence sound at high amplitude.

- 2) The analyses on the MPP silencer in this thesis are focused of the effect of orifice nonlinearity caused by moderate acoustic excitation, while the nonlinear feature is also possible to be induced by the presence of internal flow or even by a combination of the uniform flow and moderate acoustic excitation. The acoustic response of the MPP silencer and the sound field in duct would be affected by the grazing flow. Therefore, the investigation on the effect of flow induced orifice nonlinearity on the fluid-acoustic-structural interaction of the MPP silencer in the duct with uniform flow in both linear and nonlinear regimes can be conducted for future studies.
- 3) The study on the performance of MPP absorbers in chapter two has shown the promising absorption behavior with broad bandwidth by using MPP absorber array with partitioned backing cavity of different depths due to the parallel absorption mechanism. As such, it is expected that a broadband sound attenuation can be achieved by the array of MPP silencers with different cavity depths or MPP parameters in both linear and nonlinear regimes. Hence, it is necessary to establish a model in order to investigate the complicated vibro-acoustic coupled system of the array of MPP silencers with the effect of orifice nonlinearity and the noise suppression mechanism with impedance discontinuity.

- 4) Instead of controlling the fan noise in the propagating path, the fan noise in dipole nature can also be controlled by the MPP at the source position like the membrane housing device, which can be regarded as the MPP housing device. The high excitation generated by the dipole source is possible to change the acoustic response of the MPP housing device in the nonlinear regime. Meanwhile, the effect of the unsteady flow induced by the fan operation on the sound radiation mechanism of the fan-ducted system with MPP housing device is another important factor that is necessary to be considered.

- 5) The analyses on the fluid-acoustic-structural interactions of the flexible boundaries in this thesis are conducted in the fan-ducted system at low Mach number. However, in some extreme environments, the sound intensity would be very high and hence the acoustic field of the system is no longer linear. Therefore, a further study about the sound radiation mechanism and fluid-acoustic-structural interaction of fan-ducted system with flexible structures with considering the nonlinear acoustic propagation is recommended.

References

- Allard, J. I. (1993). *Propagation of Sound in Porous Media Modelling Sound Absorption Material* (Elsevier Applied Science, England).
- Beranek, L. L., and Vér, I. L. (2006). *Noise and vibration control engineering: principles and applications* (Wiley, Hoboken), pp. 279-343.
- Bielak, G., Gallman, J., Kunze, R., Murray, P., Premo, J., Kosanchick, M., Hersh, A., Celano, J., Walker, B., Yu, J., Kwan, H. W., Chiou, S., Kelly, J., Betts, J., Follet, J. and Thomas, R. (2002). "Advanced Nacelle Acoustic Lining Concepts Development," NASA/CR-2002-211672.
- Bolt, R. H. (1947). "On the design of perforated facings for acoustic materials," J. Acoust. Soc. Am. 19, 917-921.
- Bravo, T., Maury, C. and Pinhede, C. (2012). "Vibroacoustic properties of thin micro-perforated panel absorbers," J. Acoust. Soc. Am. 132, 789-798.
- Brown, C. E., and Michael, W. H. (1954). "Effect of Leading-Edge Separation on the Lift of a Delta Wing," AIAA J. 21, 690-694.
- Choy Y. S. (2012). "Low frequency noise absorption by helium-filled ductlining," J. Noise Control Eng. 60(1), 10-21.
- Choy, Y. S., and Huang, L. (2002). "Experimental studies of a drumlike silencer," J. Acoust. Soc. Am. 112, 2026-2035.
- Choy, Y. S. and Huang L. (2003). "Drum Silencer with shallow cavity filled with helium," J. Acoust. Soc. Am. 114, 1477-1485.
- Choy, Y. S., and Huang, L. (2005). "Effect of flow on the drumlike silencer," J. Acoust. Soc. Am. 118, 3077-3085.
- Choy, Y. S., Huang, L., and Wang, C. (2009). "Sound propagation in and low frequency noise absorption by helium-filled porous material," J. Acoust. Soc. Am. 126, 3008-3019.
- Crocker, M. J. (1998). *Handbook of Acoustics* (John Wiley & Sons, Inc., NY), pp. 203-210.
- Cummings, A. (1986). "Transient and multiple frequency sound transmission through perforated plates at high amplitude," J. Acoust. Soc. Am. 79, 942-951.
- Cummings, A., and Eversman, W. (1983). "High amplitude acoustic transmission through duct terminations: Theory," J. Sound Vib. 91, 503-518.

- Curle, N. (1955). "The Influence of Solid Boundaries upon Aerodynamic Sound," Proc. R. Soc. London, Ser. A 231, 505-514.
- Currie, I. G. (2013). *Fundamental mechanics of fluids* (CRC press, Boca Raton, FL), pp. 73-91.
- Dai, X., Jing, X. and Sun, X. (2012). "Discrete vortex model of a Helmholtz resonator subjected to high-intensity sound and grazing flow," J. Acoust. Soc. Am. 132, 2988-2996.
- Dowell, E. H., and Voss, H. M. (1963). "The effect of a cavity on panel vibration," AIAA J. 1, 476-477.
- Ffowcs Williams, J. E., and Hawkings, D. L. (1969). "Sound Generation by Turbulence and Surfaces in Arbitrary Motion," Philos. Trans. Roy. Soc. London Ser. A 264, 321-342.
- Frendi, A., Maestrello, L., and Bayliss, A. (1994). "Coupling Between Plate Vibration And Acoustic Radiation," J. Sound Vib. 177, 207-226.
- Fuchs, H. V. (2001a). "Alternative Fibreless Absorbers - New Tools and Materials for Noise Control and Acoustic Comfort," Acta Acust. united Ac. 87, 414-422.
- Fuchs, H. V. (2001b). "From Advanced Acoustic Research to Novel Silencing Procedures and Innovative Sound Treatments," Acta Acust. united Ac. 87, 407-413.
- Hersh, A. S., Walker, B. E., and Celano, J. W. (2003). "Helmholtz Resonator Impedance Model, Part 1: Nonlinear Behavior," AIAA J. 41, 795-808.
- Howe, M. S. (1998). *Acoustics of fluid-structure interactions* (Cambridge University Press, Cambridge; New York), pp. 27-33.
- Howe, M. S. (2003). *Theory of vortex sound* (Cambridge University Press, New York), pp. 25-40.
- Huang, L. (1999). "A theoretical study of duct noise control by flexible panels," J. Acoust. Soc. Am. 106, 1801-1809.
- Huang, L. (2002), "Model analysis of a drumlike silencer," J. Acoust. Soc. Am. 112, 2014-2025.
- Huang, L. (2006), "Broadband sound reflection by plates covering side-branch cavities in a duct," J. Acoust. Soc. Am. 119, 2628-2638.
- Huff, D. L. (2013), "NASA Glenn's Contributions to Aircraft Engine Noise Research," NASA/TP-2013-217818.

- Ingard, K. U. (1995). *Notes on sound adsorption technology* (Noise Control Foundation, Poughkeepsie, NY), Chap. 3, pp. 1-18.
- Ingard, U., and Ising, H. (1967). "Acoustic Nonlinearity of an Orifice," *J. Acoust. Soc. Am.* 42, 6-17.
- Ingard, U., and Labate, S. (1950). "Acoustic Circulation Effects and the Nonlinear Impedance of Orifices," *J. Acoust. Soc. Am.* 22, 211-218.
- Ji, Z. L. (2005). "Acoustic attenuation performance analysis of multi-chamber reactive silencers," *J. Sound Vib.* 283, 459-466.
- Jing, X. and Sun, X. (2000). "Discrete Vortex Simulation on the Acoustic Nonlinearity of an Orifice," *AIAA J.* 38, 1565-1572.
- Kowalczyk, K., and Van Walstijn, M. (2008). "Formulation of locally reacting surfaces in FDTD/K-DWM modelling of acoustic spaces," *Acta Acust. united Ac.* 94, 891-906.
- Lee, D. H., and Kwon, Y. P. (2004). "Estimation of the absorption performance of multiple layer perforated panel systems by transfer matrix method," *J. Sound Vib.* 278, 847-860.
- Lee, F.C. and Chen, W.H. (2001). "Acoustic transmission analysis of multi-layer absorbers," *J. Sound Vib.* 248(4), 621-634.
- Lee, Y. Y., Lee, E. W. M., and Ng, C. F. (2005). "Sound absorption of a finite flexible micro-perforated panel backed by an air cavity," *J. Sound Vib.* 287, 227-243.
- Li, D., Cheng, L., Yu, G.H. and Vipperman, J.S. (2007). "Noise control in enclosures: Modeling and experiments with T-shaped acoustic resonators," *J. Acoust. Soc. Am.* 122, 2615-2625.
- Lighthill, M. J. (1952). "On Sound Generated Aerodynamically. I. General Theory," *Proc. R. Soc. London, Ser. A* 211, 564-587.
- Liu, Y., Choy, Y. S., Huang, L., and Cheng, L. (2012). "Noise suppression of a dipole source by tensioned membrane with side-branch cavities," *J. Acoust. Soc. Am.* 132, 1392-1402.
- Liu, Y., Choy, Y. S., Huang, L., and Cheng, L. (2014). "Reactive control of subsonic axial fan noise in a duct," *J. Acoust. Soc. Am.* 136, 1619-1630.
- Longhouse, R. (1977). "Vortex shedding noise of low tip speed, axial flow fans," *J. Sound Vib.* 53, 25-46.

- Maa, D. Y. (1975). "Theory and design of microperforated panel sound-absorbing constructions," *Sci. Sin.* 18, 55-71.
- Maa, D.Y. (1987). "Microperforated Panel wide-band absorbers," *J. Noise Control Eng.* 29, 77-84.
- Maa, D. Y. (1996). "Microperforated panel at high sound intensity," *Acta Acust. united Ac.* 21, 10-14.
- Maa, D. Y. (1998). "Potential of microperforated panel absorber," *J. Acoust. Soc. Am.* 104, 2861-2866.
- Mu, R. L., Toyoda, M., and Takahashi, D. (2011). "Sound insulation characteristics of multi-layer structures with a microperforated panel," *Appl. Acoust.* 72, 849-855.
- Ostoich, C. M., Bodony, D. J., and Geubelle, P. H. (2013). "Interaction of a Mach 2.25 turbulent boundary layer with a fluttering panel using direct numerical simulation," *Phys. Fluids* 25, 110806.
- Park, S.-H. (2013). "A design method of micro-perforated panel absorber at high sound pressure environment in launcher fairings," *J. Sound Vib.* 332, 521-535.
- Peake, N. (2004). "On the unsteady motion of a long fluid-loaded elastic plate with mean flow," *J. Fluid Mech.* 507, 335-366.
- Russell, D. A., Junell, J., and Ludwigsen, D. O. (2013). "Vector acoustic intensity around a tuning fork," *Am. J. Phys.* 81, 99-103.
- Sabina, F. J., and Babich, V. M. (2001). "Low-frequency scattering of acoustic waves by a bounded rough surface in a half-plane," *J. Acoust. Soc. Am.* 109, 878-885.
- Sabina, F. J., and Willis, J. R. (1975). "Scattering of SH Waves by a Rough Half-Space of Arbitrary Slope," *Geophys. J. R. Astr. Soc.* 42, 685-703.
- Saffman, P. G. (1992). *Vortex dynamics* (Cambridge University Press, Cambridge; New York), pp. 95-115.
- Sakagami, K., Morimoto, M., and Koike, W. (2006). "A numerical study of double-leaf microperforated panel absorbers," *Appl. Acoust.* 67, 609-619.
- Salikuddin, M., and Ahuja, K. K. (1983). "Acoustic power dissipation on radiation through duct terminations: Experiments," *J. Sound Vib.* 91, 479-502.
- Seo, S. H. and Kim, Y. H. (2005), "Silencer design by using array resonators for low frequency band noise reduction," *J. Acoust. Soc. Am.* 118, 2332-2338.
- Sharland, I. (1964). "Sources of noise in axial flow fans," *J. Sound Vib.* 1, 302-322.

- Sivian, L. J. (1935). "Acoustic impedance of small orifices," J. Acoust. Soc. Am. 7, 94-101.
- Sucheendran, M. M., Bodony, D. J., and Geubelle, P. H. (2013). "Coupled Structural-Acoustic Response of a Duct-Mounted Elastic Plate with Grazing Flow," AIAA J. 52, 178-194.
- Taflove, A., and Brodwin, M. E. (1975). "Numerical Solution of Steady-State Electromagnetic Scattering Problems Using the Time-Dependent Maxwell's Equations," IEEE Trans. Microwave Theory Tech. 23, 623-630.
- Tang, S. K. (2011). "Vortex sound in the presence of a low Mach number flow across a drum-like silencer," J. Acoust. Soc. Am. 129, 2830-2840.
- Tang, S. K., Leung, R. C. K., So, R. M. C., and Lam, K. M. (2005). "Acoustic radiation by vortex induced flexible wall vibration," J. Acoust. Soc. Am. 118, 2182-2189.
- Tayong, R., Dupont, T., and Leclaire, P. (2010). "On the variations of acoustic absorption peak with particle velocity in micro-perforated panels at high level of excitation," J. Acoust. Soc. Am. 127, 2875-2882.
- Thurston, G. B., Jr., L. E. H., and Cook, B. D. (1957). "Nonlinear properties of circular orifices," J. Acoust. Soc. Am. 29, 992-1001.
- Toyoda, M., Mu, R. L. and Takahashi, D. (2010). "Relationship between Helmholtz-resonance absorption and panel-type absorption in finite flexible microperforated-panel absorbers," Appl. Acoust. 71, 315-320.
- Vallentine, H. R. (1959). *Applied hydrodynamics* (Butterworths Scientific Publications, London), pp. 102-135.
- Wang, C. Q., Han, J. and Huang, L. (2007), "Optimization of a clamped plate silencer," J. Acoust. Soc. Am. 121, 949-960.
- Wang, C., and Huang, L. (2011). "On the acoustic properties of parallel arrangement of multiple micro-perforated panel absorbers with different cavity depths," J. Acoust. Soc. Am. 130, 208-218.
- Wang, X. N., Choy, Y. S. and Cheng, L. (2012). "Hybrid noise control in a duct using a light micro-perforated plate," J. Acoust. Soc. Am. 132, 3778-3787.
- Yairi, M. and Sakagami, K. (2011). "Excess sound absorption at normal incidence by two microperforated panel absorbers with different impedance," Acoust. Sci. & Tech. 32, 194-200.

Yi, S. and Lee, B. H. (1986), "Three-dimensional acoustic analysis of circular expansion chambers with a side inlet and a side outlet," *J. Acoust. Soc. Am.* 79, 1299-1306.

Zha, X., Kang, J., Zhang, T., Zhou, X., and Fuchs, H. (1994). "Application approach for microperforated panel sound absorbers," *Acta Acustica* 19, 256-265.

Zhang, Q., and Bodony, D. J. (2016). "Numerical investigation of a honeycomb liner grazed by laminar and turbulent boundary layers," *J. Fluid Mech.* 792, 936-980.

Zhang, Z. M., and Gu, X. T. (1998). "The theoretical and application study on a double layer microperforated sound absorption structure," *J. Sound Vib.* 215, 399-405.